Microstructure and Carrier Transport Processes in Semiconducting Polymers

by

Ban Xuan Dong

A dissertation submitted in partial fulfillment
of the requirements for the degree of
Doctor of Philosophy
(Materials Science and Engineering)
in the University of Michigan
2017

Doctoral Committee:

Professor Peter F. Green, Chair
Professor Jinsang Kim
Associate Professor Anish Tuteja
Associate Professor Zhaohui Zhong

Ban Xuan Dong

banxdong@umich.edu

ORCID iD: 0000-0002-2873-5207

ACKNOWLEDGEMENTS

Looking back the past 5 years since I started my graduate study at the University of Michigan, I am extremely grateful for all the love and support I receive from friends, family and colleges who have made my PhD a very memorable and joyful experience.

First, I would like to thank Vietnam Education Foundation (VEF) for providing me financial support and helps to pursue my graduate study in the United States. Throughout VEF program, I had the opportunity to know and discuss with Professor Peter Green. His solid knowledge and physical intuition in the field of polymer physics had motivated me to join his group at the University of Michigan, and ever since I always knew that his lab was the right place for me. I would like to express my deepest acknowledgement to Peter for his strong support from all fronts. Not only providing me with invaluable resources and guidance to lead me through the tough times of my research, his style of mentorship has also helped me to become a very independent researcher, preparing me for the next step of my career. I am also sincerely grateful to my other committee members, Professor Jinsang Kim, Professor Anish Tuteja and Professor Zhaohui Zhong for providing insightful comments and suggestions for my research.

Research is a collaborative effort and a substantial portion of my success is rested on the shoulders of my collaborators. I would like to give a special thank you to Professor Gila Stein at the University of Tennessee for providing me so much insight into X-Ray diffraction and further improved my research. I would like to also thank Dr. Joseph Strzalka and Dr. Zhang Jiang at

Argonne National Lab, Geoffrey Purdum and Professor Lynn Loo at Princeton University, Dr. Mitchell Smith, Professor Anne McNeil, Dr. Adam Barito, Dr. Matthew Sykes, Dr. David Bilby for your collaborative works.

I would never have made it this far without the help of all my previous and current Green Group colleagues. You are not only my co-workers, my collaborators but also my dearest friends. Thank you for making every working day in Green Group a fun but also challenging experience. It has been an absolute pleasure working and hanging out with all of you, Dr. Bingyuan Huang, Dr. Anton Li, Dr. Jojo Amonoo, Dr. Emmanouil Glynos, Dr. Bradley Frieberg, Dr. Junnan Zhao, Dr. Peter Chung, Dr. Hengxi Yang, Dr. Aaron Tan, Kyle Johnson, Ravi Sharma and Jill Wenderott.

Finally, I would like to express my greatest thanks to my family and friends at Ann Arbor. I would like to thank my loving wife, my distant family for their unconditional love and support. And of course special thank you to many friends that I have made in Ann Arbor, both at and outside the University of Michigan that made my graduate life more joyful.

TABLE OF CONTENTS

LIST OF FIGURES

ABSTRACT

The molecular design and synthesis of semiconducting conjugated polymers was a major achievement in the field of chemistry, enabling the now viable organic electronics industry. Unlike their crystalline inorganic counterparts, the weak van der Waals bonding forces between conjugated polymer chains give rise to significant structural and energetic disorder. This reduces charge carrier mobility and adversely impacts device performances. Efforts to understand carrier transport in conjugated polymer systems have been challenged due to the complexity of the structure and a lack of proper understanding of the manner in which the polymer morphology affects electrical properties. This thesis focuses on developing several experimental strategies to turn polymer morphologies and studying the impact of polymer microstructure on carrier transport. The experimental approaches for morphology manipulation in this thesis include (i) fabricating film with different thickness (ii) using the environmentally benign method supercritical carbon dioxide processing and (iii) using a novel vacuum deposition technique to deposit thin polymer films.

By studying thickness dependence of morphology and carrier transport in a low bandgap polymer, we show that the out-of-plane carrier mobilities in conjugated polymer films monotonically increase with thickness in the range of 100 nm to 1 μm due to substrate-induced morphological changes as a function of film thickness. Our findings demonstrate that carrier mobility in conjugated polymers is not intrinsic properties of the materials but rather dictated by

local morphology; it could vary nearly by an order of magnitude depend on the proximity to the substrate.

For the second route, we show how the polymer structure near polymer/substrate interface in organic thin film transistor can be selectively manipulated using supercritical carbon dioxide processing. Subsequently, we observe a significant enhancement in the in-plane carrier mobility that is accompanied by rather a subtle change in polymer morphology. This demonstrates that supercritical carbondioxide processing is an effective way to control polymer structure near the buried interface.

Lastly, we introduce a novel vacuum deposition technique Matrix-Assisted Pulse Laser Evaporation (MAPLE) to fabricate conjugated polymer films. Although the structure of MAPLE-deposited samples is highly disordered, transistor devices made from MAPLE-deposited films exhibit superior in-plane transport characteristics. Motivated by this finding, we then employ an advanced X-ray characterization method called complete pole figure construction and characterize the polymer structure at different stage of deposition in order to reveal the structure of MAPLE-deposited films at the buried interface. To our surprise we discover a large population of highly-oriented crystals at the buried interface having structure strongly depending on the substrate chemistry. We also show that this polymer layer dictates transport in thin film transistor, showing the importance of characterizing the structure at the buried interface in order to evaluate transistor performance.

Chapter 1 : INTRODUCTION

1.1. BACKGROUND AND MOTIVATION

The synthesis of conjugated polymers was a major achievement of the field of chemistry; it enabled collaborations with the fields of physics and engineering to create the now viable organic electronics industry. The field is based on the use of semiconducting carbon-based polymers in the active layers of electronic devices. Organic electronics are not being developed to replace traditional electronics, but instead serve as a complement to existing technologies. A continued fascination with the engineering and scientific challenges is partly driven by the nearly limitless possibilities for tuning the optoelectronic properties of organic molecules via molecular design. Additionally, solution processing over large areas, low-cost device fabrication, and the ability to readily deposit active layers on flexible substrates, contribute to both low cost and the use for different applications, that are not possible for conventional hard semiconducting materials. With their unique capabilities, various devices based on conjugated polymers that includes xerography,[1] organic light-emitting diodes (OLEDs),[2,3] organic thin-film transistors(TFTs)[4] and organic photovoltaics (OPVs).[5,6] are beginning to come to market.

In devices made from conjugated polymers, charge carrier mobility is arguably the most important figure of merit which directly influences external quantum efficiency in OLEDs, switching speed in TFTs, short circuit current, fill factor and consequently power conversion efficiency in OPVs.[7–9] An important limitation nevertheless is that organic materials possess significant structural and energetic disorder; this is responsible for limited charge carrier

mobilities and low device performances. Efforts to improve carrier mobilities in polymers and organic materials are often hindered by the lack of a proper, or generally accepted, physical description of carrier transport in organic semiconductors. Some of these difficulties arise from the complexity of the morphology and a lack of understanding of the manner in which certain physical properties depend on the morphology. The goal of this dissertation here is to use different methodologies to alter the morphological structure of semicrystalline semiconducting polymers and study the effect of structure on charge carrier transport. Understanding the effect of processing conditions and polymer chemistry on microstructure and charge transport will help in the effort to establish rigorous design rules for new conjugated polymers with improved properties.

1.2. CHARGE TRANSPORT MECHANISMS IN CONJUGATED POLYMER

We are used to ubiquitous polymers (or plastics) being somewhat opposite to metals: they are insulator and do not conduct electricity. In fact, in many applications electric wires or other electronic parts are coated with polymers to protect them from short-circuits. In order to make polymer conductive, a key importance is the presence of alternative double bond and single bonds along the backbone of the polymer (or conjugated backbone). Conjugated polymer backbone contains localized sigma (σ) bond which forms a strong chemical bond and less strongly localized "pi" (π) bond which is weaker. The electrons in the partially empty conjugated p-orbitals are highly mobile and can move across the polymer backbone. However, conjugation alone is not enough to make the polymeric material conductive. In addition to this, charge carriers in the form of extra electrons or "holes" have to be injected into the material. The game changing moment came in 1977 when Heeger, MacDiarmid and Shirakawa discovered oxidation of polyacetylene with chlorine, bromine or iodine vapor make it 10^9 times more conductive than

they were originally. [10] The finding has opened up a new field of research where one can have a material with electrical and optical properties of traditional semiconductor/metal and in the same time having the processability of polymers. The discovery of conductivity in polymers was recognized in 2000 when Heeger, MacDiarmid and Shirakawa were awarded the Nobel Prize in Chemistry.[11]

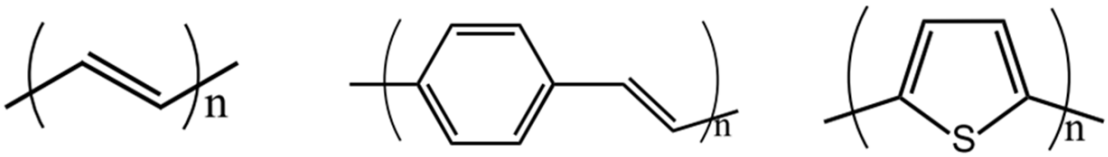

Polyacetylene poly(p-phenylene vinylene) Poly(thiophene)

Figure 1.1 Chemical structure of some common conjugated polymers

The mechanisms of charge transport conjugated polymers are fundamentally different from crystalline inorganic semiconductors. Carrier mobilities in conjugated polymers are necessarily highly anisotropic, occurring at different rates, depending on the path taken by the carriers (Figure 1.2). Intrachain carrier transport along the backbone segment of a chain, free of local distortions, is relatively fast. However, when the conjugation in conjugated polymer is disrupted, carrier will not be able to continue moving along the polymer backbone. In this case, charge carrier can hop to another adjacent polymer chain via so-called pi-pi stacking direction, providing that their wave functions overlap (Figure 1.2). The interchain hopping transport between polymer chains is very slow and this is known to be responsible for low carrier mobility in conjugated polymers.

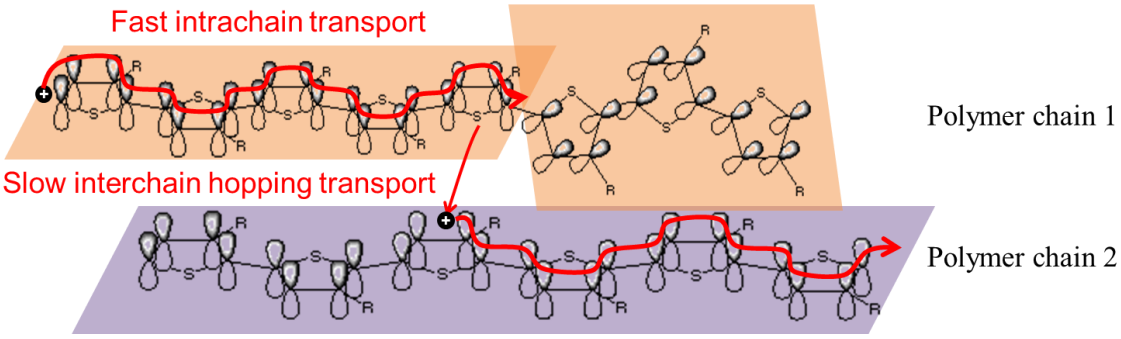

Figure 1.2: Illustration of intra- and inter- chain transport in conjugated polymers

The interplay between microstructure and carrier transport processes in conjugated polymers is still far away from being clearly articulated. The difficulties partially originate from the complex morphology of conjugated polymers. In contrast to crystalline inorganic semiconductor, conjugated polymer chains are bonded together by weak Van der Waals forces with numerous degrees of conformational freedom, resulting in complex and disordered microstructures. Typical conjugated polymer films are semicrystalline in which ordered (aggregate) and disordered (amorphous) regions coexist (Figure 1.3a). The aggregates part composes of co-facially stacked molecules having strong π-orbital overlap. In a semicrystalline film, the reduced conjugation lengths and increased band gaps of the amorphous regions are responsible for reduced carrier mobilities and confine transport within the aggregate regions because carrier moves from aggregate to amorphous region will encounter an energy barrier (Figure 1.3b). It is suggested that the carriers only move across the amorphous regions from aggregate to aggregate via single polymer chains known as tie-molecules.[12,13] This concept of transport was proved by measuring the electroluminescence (EL) of a mixture of regioregular poly(3-hexylthiophene) (RR-P3HT) nanofibrils and regiorandom poly(3-hexylthiophene) (RRa-P3HT). It was shown that the EL spectra of the blends resemble with that of pure RR-P3HT, suggesting that the charges are traveling within the ordered regions of the samples.[12] Molecular weight also has a profound

impact on carrier transport in conjugated polymers. High molecular weight provides electrical connectivity between ordered regions, allowing efficient charge transport and resulting in higher carrier mobility, despite the fact that high molecular weight polymers are usually more disordered and have lower degree of crystallinity (Figure 1.3c).[14,15]

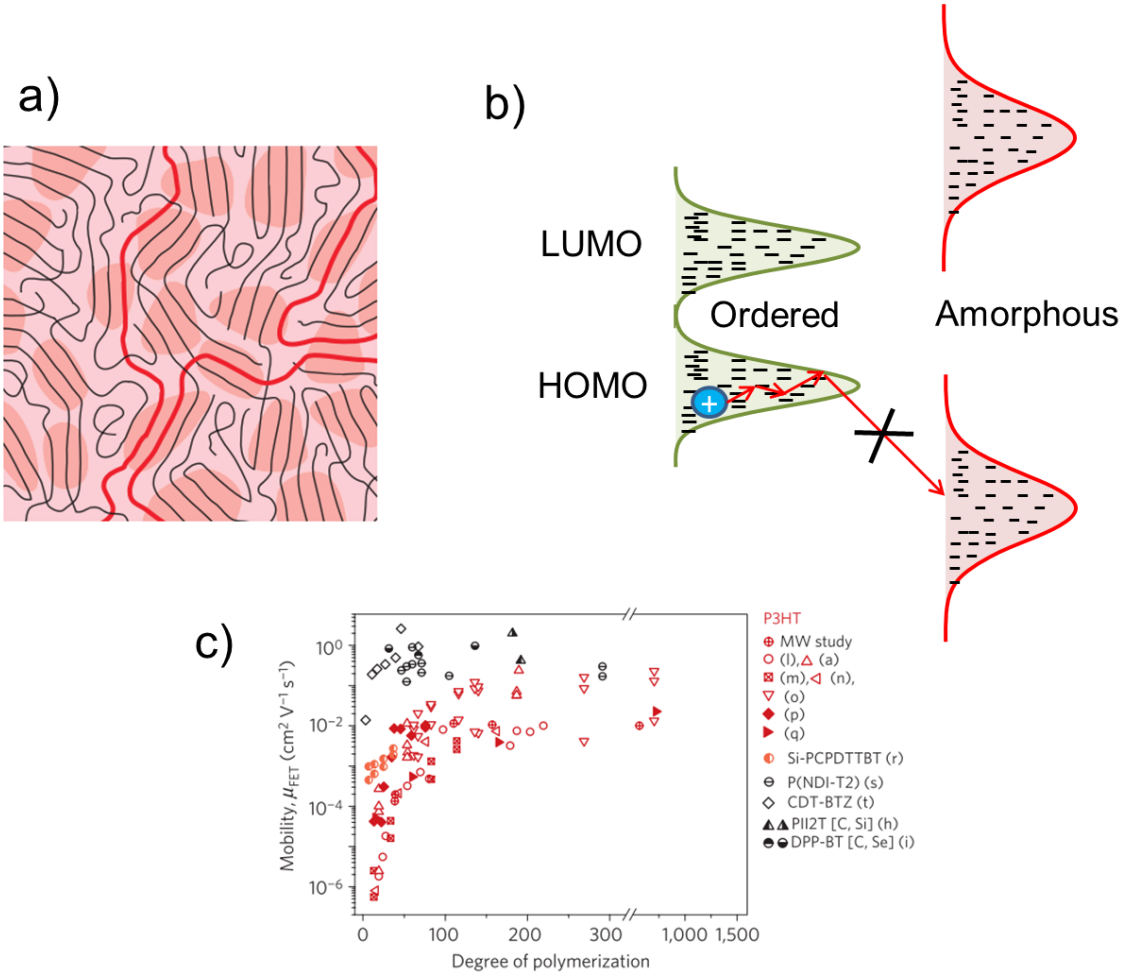

Figure 1.3: a) Microstructure of conjugated polymer films, demonstrating the coexistence of ordered and amorphous regions (Reproduced from[12]). b) Energy level of ordered and amorphous regions c) Dependence of carrier mobility on molecular weight, or degree of polymerization (Reproduced from[12]).

1.3. CHARGE TRANSPORT THEORY: GAUSSIAN DISORDER MODEL

In order to extract more information about the transport mechanism of conjugated polymers, we can fit transport behavior to a charge transport model. While there is a variety of charge transport model exists in literature to describe charge transport in disordered semiconductors, in this thesis we mainly use the Gaussian Disorder Model (GDM) proposed by Bässler.[16,17] This model is frequently used to explain the temperature and electric field dependence of mobility in semiconducting polymers. In brief, the GDM proposes that charge carrier hopping within an energy landscape characterized by both energetic and positional disorder. The system is considered as a manifold of uncorrelated transport sites whose energies adopt a Gaussian density of state (DOS) distribution in which carrier can hop with rates determined by Miller-Abrahams form:

$$\begin{aligned} \nu_{ij} &= \nu_0 e^{-2\gamma a\frac{r_{ij}}{a}} \times e^{-\frac{\varepsilon_j-\varepsilon_i}{kT}} \quad for\ \varepsilon_j > \varepsilon_i \\ \nu_{ij} &= \nu_0 e^{-2\gamma a\frac{r_{ij}}{a}} \times 1 \qquad for\ \varepsilon_j \le \varepsilon_i \end{aligned} \tag{1-1}$$

Here, ν_{ij} is the hopping rate between site i and j having the energy ε_i and ε_j; a is the average lattice distance; r_{ij}/a is the relative jump distance between sites *i* and *j*; γ is the parameter related to the electronic coupling matrix between adjacent sites and ν_0 is the frequency pre-factor. The equation above predicts that only charge carriers move to sites higher in energy are thermally activated and affected by electric field. Downward jumps from high to low energy sites, however, are not affected by electric field and thus the charge carriers can execute a random walk and they tend to relax toward the equilibrium energy $\langle\varepsilon_\infty\rangle = -\sigma^2/kT$ below the center of DOS as depicted in Figure 1.4.

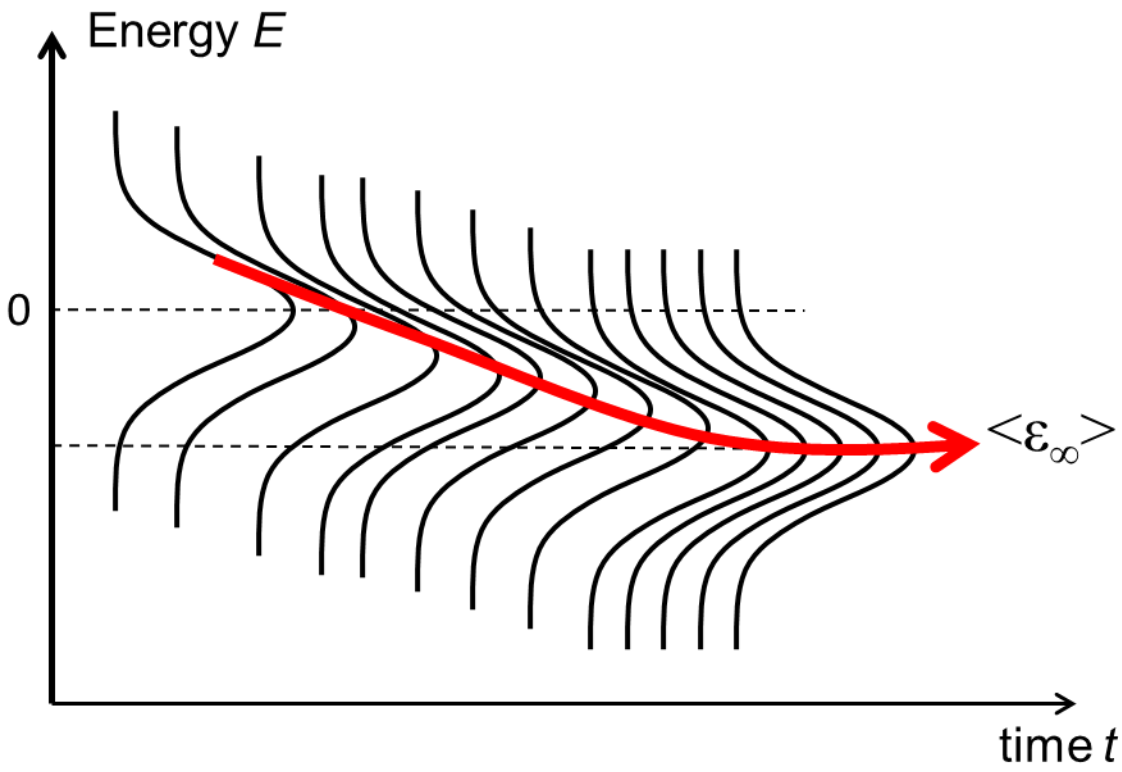

Figure 1.4: Carrier energy relaxation in a Gaussian DOS

Since the activation energy is a function of 1/T, the logarithm of carrier mobility as described by the GDM linearly scales with $1/T^2$ as opposed to the typical Arrhenius dependent of mobility on temperature. In the GDM, the temperature and electric field dependencies of mobility are described using the following equation:

$$\mu(T,E) = \mu_0 \exp[-\frac{2}{3}(\frac{\sigma}{kT})^2]\exp\{C[(\frac{\sigma}{kT})^2 - \Sigma^2]E^{1/2}\} \qquad (1\text{-}2)$$

Here, σ is the width of the Gaussian DOS, Σ is a parameter that describes the positional disorder, E is the electric field and C is a fitting parameter. As mentioned above, the GDM predicts non-Arrhenius temperature dependence of carrier mobility which has been widely observed.[18,19] Moreover, GDM predicts that the slope of the E-dependence of mobility plot may

turn negative is systems having high degree of positional disorder. In such systems, there is large fluctuation of the electronic coupling between the charge transport sites, creating fast and slow routes for charge carrier transport. At higher fields, detour routes around unfavorable transport sites are gradually diminished, resulting in negative electric field dependence of carrier mobility.

1.4. CHARGE CARRIER MOBILITY MEASUREMENT TECHNIQUES

1.4.1. Out-of-plane mobility measurement method 1: Time-of-flight

Time-of-flight (or ToF) is a very well-developed and commonly used technique to characterize out-of-plane mobility (transport in the direction perpendicular to the electrode) of low conductivity organic semiconductors.[20,21,18] A typical experimental set-up for ToF measurement is shown in Figure 1.5a.

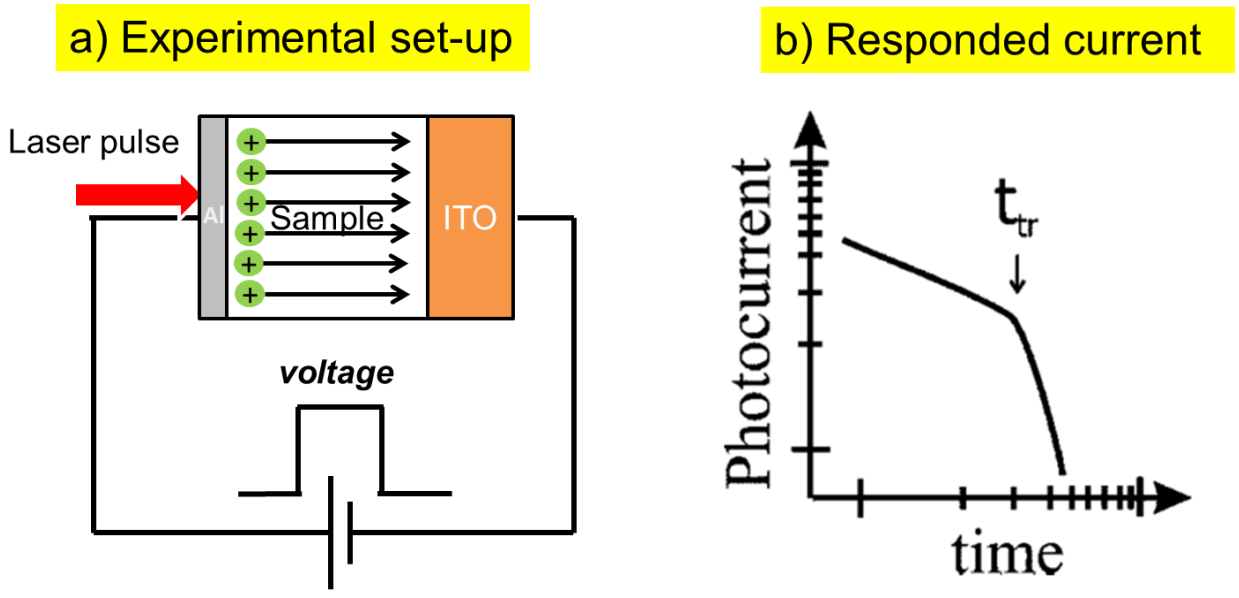

Figure 1.5: a) Experimental set-up of ToF measurement. b) Typical responded current in a ToF measurement plot in log-log scale. (reproduced with permission from ref[18]. Copyright © 2005 American Physical Society).

In a ToF measurement, a semiconductor film with thickness *h* is sandwiched between a semi-transparent electrode Al and ITO electrode. To measure hole mobility, a laser pulse with appropriate wavelength (typically the wavelength of the laser should match with the peak absorption of the semiconducting materials) is applied to the Al side of the device in order to generate a thin sheet free carriers. An external voltage pulse *U* is then applied across the device after some certain delay time in order to transport the photogenerated carriers from the Al electrode to the ITO electrode. The main idea of ToF is that the surface-generated carriers drift under a constant electric field, creating a current transient in the external circuit which is ultimately recorded by the oscilloscope. The polarity of the applied bias *U* can be controlled to selectively measure hole or electron mobilities. Such an example of recorded current transient is plotted in Figure 1.5b.

If there is no carrier trap so that transport is non-dispersive (the mobility of all carriers is the same), the current transient is ideal and there would be a clear turning point indicating the moment at which all carriers reach the opposite electrode. However, trapping is ubiquitous in organic semiconductors due to their highly disordered structure. Therefore in a real current transient as exemplified in Figure 1.5b, the current decreases slowly with time due largely to carrier trapping during the transport within the film; and the "kink" that marks the transit time t_{tr} of the carriers from one electrode to the other electrode is typically not easy to detect unless plotting in log-log scale. From the transit time t_{tr}, the bias *U* and the film thickness *h*, the carrier mobility μ can be calculated according to:

$$\mu = \frac{d^2}{U \times t_{tr}} \qquad (1\text{-}3)$$

In practice, photogenerated carriers have the space charge effect, disturbing the uniformity of the external electric field. Thus in practice the photogenerated carrier density and consequently the laser intensity should be as low as is consistent with the sensitivity of the oscilloscope. One simple but effective way is applying the laser pulses with both electrode grounded before turning on the voltage pulse.[22] One drawback of ToF is that because the generated carrier layer upon laser excitation is ca.100 nm (as calculated from the absorption coefficient), the film thickness should be much larger than that in order to give a clear "kink" in the current transient data. Therefore ToF is usually applied to films with thickness larger than 1 μm.

1.4.2. Out-of-plane mobility measurement method 2: photo-induced charge carrier extraction by linearly increasing voltage (Photo-CELIV)

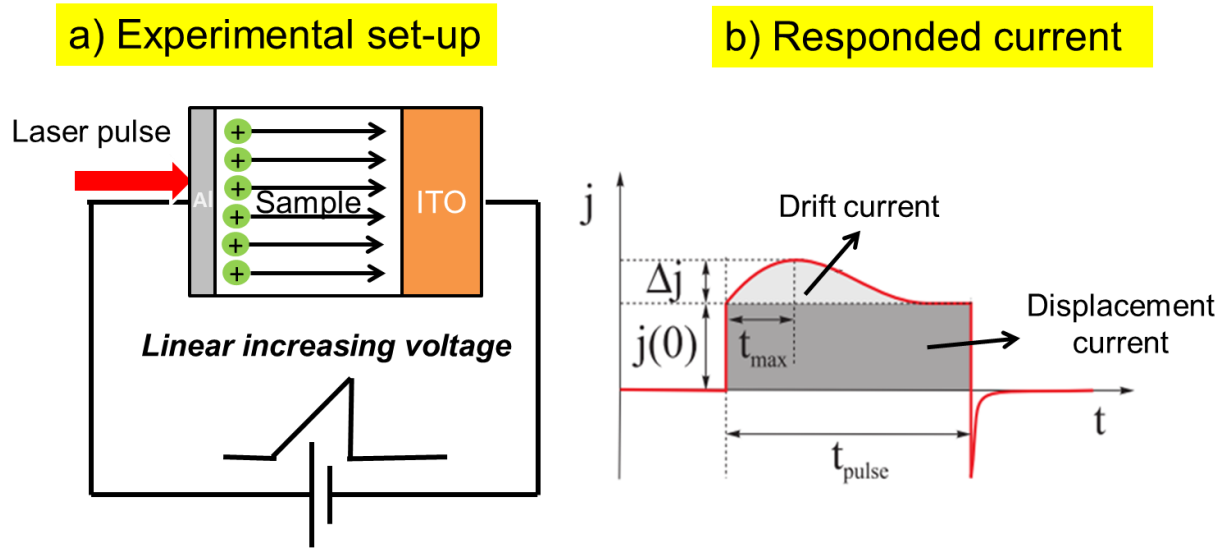

Figure 1.6: a) Experimental set-up of photo-CELIV measurement. b) Typical responded current in a photo-CELIV measurement. (reproduced with permission from ref[23]. Copyright © 2007 Wiley Periodicals, Inc., A Wiley Company).

The CELIV technique has been introduced by Juška et al. [24] to first measure carrier mobility in microcrystalline silicon and then the mobility in conjugated polymer systems as

well.[25] As depicted in Figure 1.6a, the experimental set-up of CELIV measurement is similar to ToF measurement, except that a linearly increasing voltage (or triangle voltage) instead of a square-shaped voltage pulse is applied across the sample. The CELIV technique was developed to overcome the limitation of ToF, enabling the measurement of carrier mobility of films with thickness less than 1 μm. In case of samples with sufficiently high equilibrium carrier concentration, the use of the laser pulses is not needed. However, in systems with relatively low intrinsic carrier concentration, a variant of CELIV technique named photo-CELIV is frequently used.[26,27] In photo-CELIV measurement, a laser pulse is incident to the sample in order to generate extra carriers before applying the triangle voltage pulse.

Similar to ToF measurement, the response current in photo-CELIV measurement is recorded by the oscilloscope as illustrated in Figure 1.6b. The response current in photo-CELIV measurement has two component: the displacement current $j(0) = \varepsilon\varepsilon_0 A/h$ originating from the capacitance response of the device and the drift current $\Delta j = j - j(0)$ originating from extraction of photo-generated charge carriers within the sample. Here, ε, ε_0 and A are the relative permittivity, vacuum permittivity and the ramping rate of the triangle voltage. To calculate carrier mobility in photo-CELIV measurement, the light absorption profile in the sample needs to be accounted for. In such case, the photogenerated carrier mobility may be calculated using the following equations:[27]

$$\mu = K^2 \frac{2d^2}{At_{\max}^2} = \left(\frac{t_{\max}}{t_{tr}}\right)^2 \frac{2d^2}{At_{\max}^2} \qquad (1\text{-}4)$$

$$e^{-\alpha d\left(1-t_{\max}^2/t_{tr}^2\right)}\left(1+2\alpha d t_{\max}^2/t_{tr}^2\right)=1 \qquad (1\text{-}5)$$

Here, K is a correction factor, t_{tr} is the transit time, defined as the time that a charge takes to move through the entire film thickness beginning from the surface and α is the absorption

coefficient at the laser wavelength. The electric field determined from each CELIV measurement is calculated at time $t = t_{max}$, when the most of the carriers have been extracted and moving toward the counter electrode.

1.4.3. In-plane mobility measurement using thin-film transistors

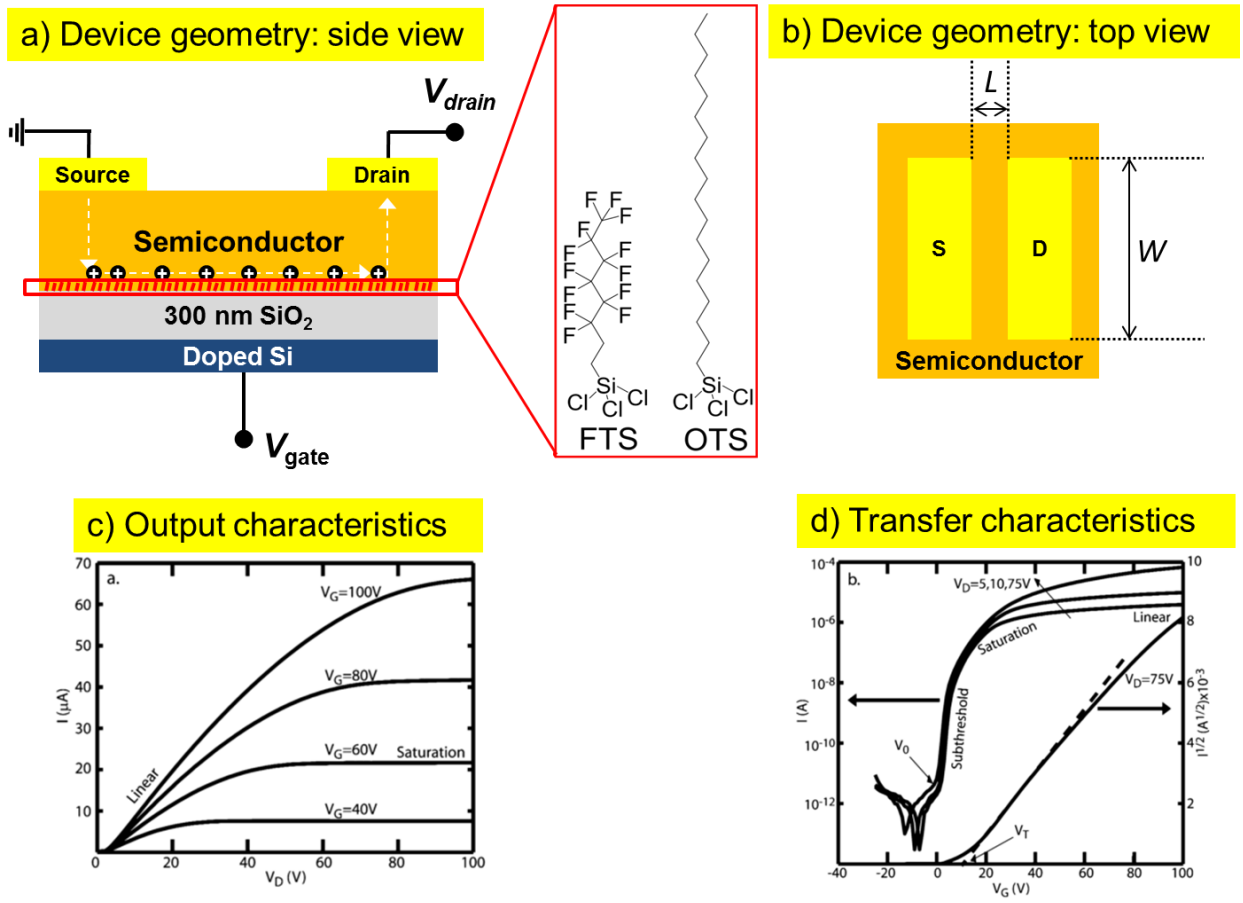

Figure 1.7: Device geometry of a bottom gate, top contact TFT with surface treatment in (a) side view and (b) top view. The top view shows definitions of channel width *W* and length *L*. (c) and (d) show exemplary transistor out-put characteristics and transfer characteristics (Reproduced with permission from ref[8]. Copyright © 2004 American Chemical Society).

In order to measure in-plane mobility, we use the thin-film transistors (TFTs) set-up as shown in Figure 1.7a and b. In TFT measurement charge carrier moves laterally (or in the in-plane direction) as opposed to ToF or CELIV measurements in which carriers move in the out-of-plane direction. Also, TFTs are 3 terminal devices that consist of gate, source and drain

electrodes. While there exist several common geometry types for TFTs including (i) bottom-gate bottom-contact, (ii) top-gate bottom-contact and (iii) bottom-gate top-contact, we choose to use bottom-gate top-contact configuration (Figure 1.7a and b) throughout this thesis due to the ease of fabrication without the use of lithography. In our work, the gate electrode is made of highly doped Si whereas the source and drain electrodes are made of gold to match with the common HOMO level of p-type conjugated polymers.[4,28] Charge transport in TFTs is known to happen near the buried interface[29,30] as opposed to bulk out-of-plane transport measured by ToF or CELIV. Therefore for our TFT devices, we treat the dielectric substrate SiO_2 with self-assemblied monolayers (SAMs) such as octadecyltrichlorosilane (OTS) or trichloro (1H, 1H, 2H, 2H-perfluorooctyl) silane (FTS) in order to improve polymer order near the buried interface and thus enhance carrier mobility (Figure 1.7a).[31,32]

All TFT devices presented in this thesis are p-type in which the majority of the transport carriers are positively charged. The semiconductor film and the gate electrode is capacitively coupled such as when a negative bias V_G is applied to the gate electrode, a population of positively charged holes will accumulate at the buried interface. The carrier density is controlled by the magnitude of the gate voltage. When the gate voltage is high enough, mobile charges are induced, and the transistor is on if a drain voltage V_D is applied between the source and drain electrode. TFT electrical properties are usually characterized two different ways: one is holding the gate voltage V_G constant and sweeping the drain voltage V_D (output characteristics, Figure 1.7c) and one is holding V_D constant and sweeping V_G (transfer characteristics, Figure 1.7d). Charge carrier mobility is calculated from the transfer characteristics curves either in linear regime or saturation regime. When V_G is small, the transistor operates in linear regime. The drain-source current I_D in this case is dependent on the device geometry (W/L), the capacitance

of the insulating dielectric C_i, the gate voltage V_G, the threshold voltage V_{th}, the drain voltage V_D and the mobility μ:

$$I_D = \mu \frac{W}{L} C_i (\mathrm{V}_G - \mathrm{V}_{th}) \mathrm{V}_d \qquad (1\text{-}6)$$

When V_d is sufficiently high, the current is in the saturation regime and no longer dependent on the drain voltage. The carrier mobility in saturation regime can be calculated using the following equation:[8]

$$I_D = \mu \frac{W}{2L} C_i (\mathrm{V}_G - \mathrm{V}_{th})^2 \qquad (1\text{-}7)$$

1.5. STRUCTURAL CHARACTERIZATION TECHNIQUES

This dissertation utilizes various techniques to characterize the morphology of conjugated polymer films. Here we will describe specifically the principles of the three most important techniques used to measure the polymer structures: variable angle spectroscopic ellipsometry (VASE), grazing incidence wide angle X-ray scattering (GIWAXS) and X-ray based complete pole figure construction.

1.5.1. Variable angle spectroscopic ellipsometry (VASE)

VASE is a versatile, non-destructive optical characterization method that can be used to characterize the optical constants and film thickness of supported thin films. Although the detailed descriptions of VASE have been discussed widely in literature,[33–36] here we will briefly outlined its basic principles for the purpose of clarity of this dissertation. Then we will go further to discuss the more sophisticated VASE methods we use to measure the chain orientation in thin polymer film.

In any VASE measurement, the optical constants and film thickness are deduced from the changes in the polarization state of light upon interacting and reflecting from the investigated sample. When linearly polarized light is incident and reflected from a sample, it becomes elliptically polarized. VASE measures the shift in the polarization of light in term of the ellipsometric angles ψ and Δ. In the case of a homogeneous and isotropic material with a flat surface, the complex reflectance ratio ρ coincides with the ratio of the complex Fresnel reflection coefficients r_p and r_s as:

$$\rho = \tan\Psi e^{i\Delta} = \frac{r_p}{r_s} \qquad (1\text{-}8)$$

Although VASE does not require a reference and is an extremely precise technique, it is however an indirect measurement technique. The parameters of interest are the film thickness d and the optical constants, either complex refractive index $\tilde{n}(\lambda) = \mathrm{n}(\lambda) + \mathrm{ik}(\lambda)$ or complex dielectrics function $\varepsilon(\lambda) = \varepsilon'(\lambda) + \mathrm{i}\,\varepsilon''(\lambda)$. These parameters can be obtained by fitting the ellipsometric data to a forward simulation via transfer matrix algebra. As a typical drawback of forward simulation technique, the uniqueness of the fit cannot be proven. Second, one must be aware of the robustness of the analysis because the fitting parameters are usually very highly correlated.[33] Realizing the unique solution set is specifically problematic in the case of highly anisotropic samples such as spin-cast conjugated polymer films, uniaxial or biaxial crystalline materials due to the large number of unknown fit parameters.

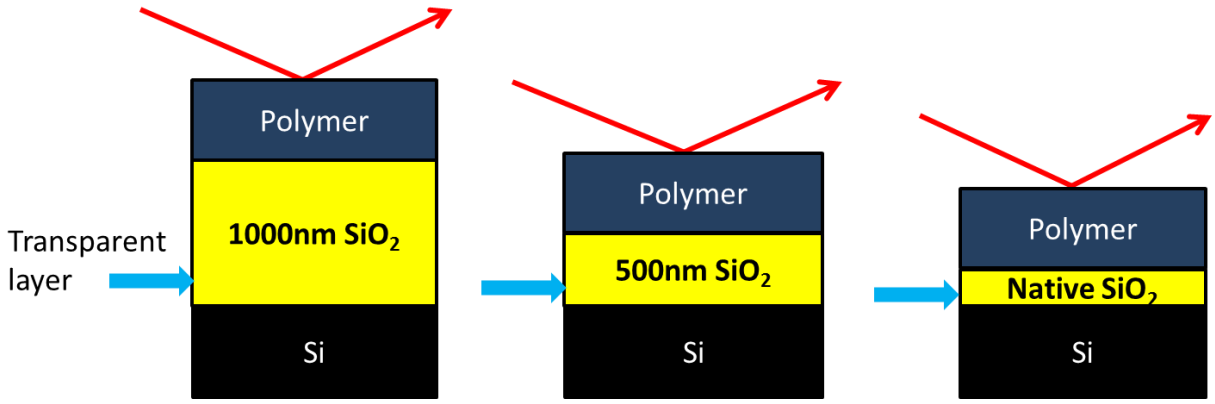

Figure 1.8: Schematic of a VASE measurement utilizing both interference enhancement and multi-sample analysis methods.

Therefore, in order to increase the uniqueness of the fit, we use a combination of interference enhancement and multi-sample analysis as shown in Figure 1.8. In interference enhancement method, a thick transparent layer (usually 300-1000 nm in thickness) is sandwiched between the substrate and the absorbing polymer film. Since the thick transparent layer underneath the absorbing layer enhances the change in path length of light, data at multiple angles will provide additional information.[37] Here we use SiO_2 as the dielectric transparent layer and Si as the substrate. In multi-sample analysis method, by measuring multiple samples but fitting the data simultaneously, more information about the same sample can be achieved without increasing the number of fitting parameters. Thus by depositing the polymer layer under the same fabrication conditions on Si/SiO_2 substrates with different thicknesses of SiO_2 layer and fitting the data simultaneously, accurate information about the anisotropic optical constants of the sample can be achieved.[38,39]

1.5.2. Grazing incidence wide-angle X-ray scattering (GIWAXS)

Synchrotron X-ray diffraction is a powerful, non-destructive technique to probe the structure of thin conjugated polymer films. Although some lab-scale X-ray measurement can be

done for strong scattering films,[40] the majority of X-ray diffraction measurement of organic semiconductor thin films is performed at a synchrotron due to the strong intensity and high collimation of the synchrotron X-ray source. Moreover, by appropriately selecting experiment conditions, synchrotron radiation allows characterization of a vast range of size scales ranging from local molecular packing scale (1 Å−10 nm) to phase segregation, domains and device scale (10 nm−100 μm).[41]

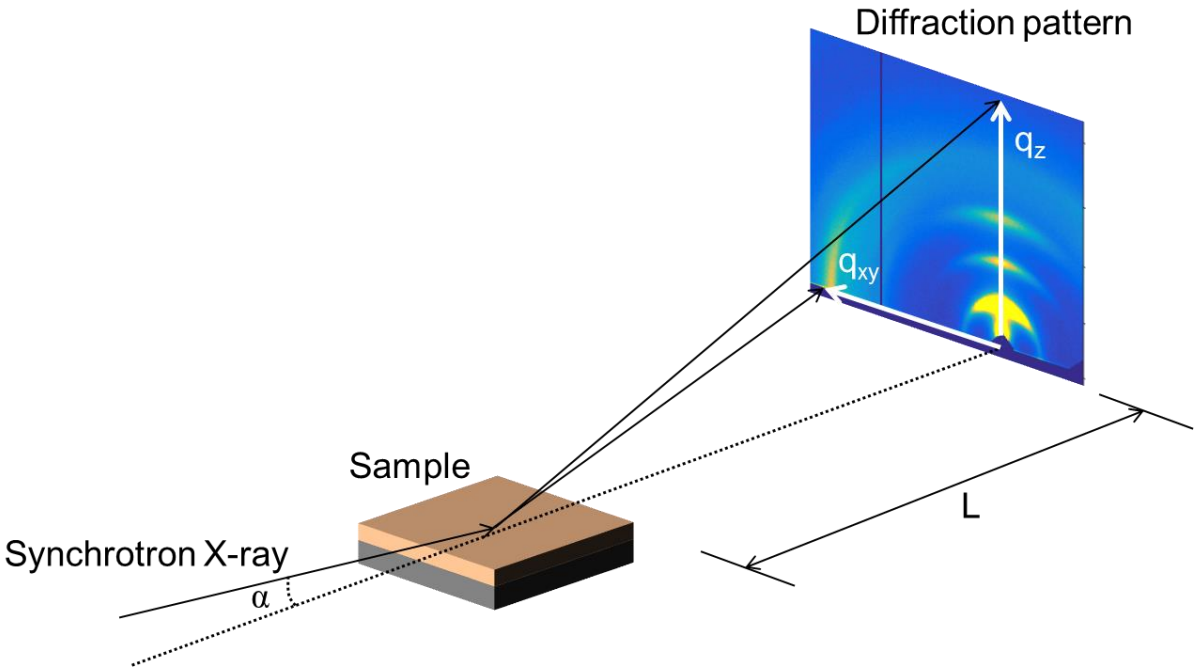

Figure 1.9: Schematic representation of a grazing incidence wide angle X-ray scattering measurement.

Perhaps one the most commonly used techniques to measure structure of conjugated polymers and other organic semiconductor thin films is grazing incidence wide angle X-ray scattering (GIWAXS). Similar to many other X-ray diffraction techniques, GIWAXS principles are based on the coherent scattering of radiation beams reflected off from ordered lattice planes. The schematic of GIWAXS measurement is shown in Figure 1.9. In a GIWAXS measurement, the X-ray beams is incident at a shallow angle α that is below the critical angle of the substrate

but above that of the films in order to probe the structure of the whole samples. The shallow angle used in GIWAXS also permits large sample volume probed by the X-ray radiations and thus improves signal to noise ratio. As the X-ray beams propagate through the, a fraction of it will be diffracted. Constructive interference of the diffracted beams results in observable diffraction peaks on the 2D detector. The use of an area 2D detector allows rapid data collection over a relatively large scale of scattering angle. Therefore in GIWAXS measurement the sample exposing time is reduced and the sample beam damage is minimized.[42] For a given scattering angle 2θ, the Bragg condition satisfies if the magnitude of the scattering vector q equals the reciprocal lattice vector q_B as:

$$\vec{q} = \overrightarrow{q_B} = \frac{4\pi}{\lambda}\sin\theta_B \qquad (1\text{-}9)$$

From the angle of the diffraction spots and direction of the diffracted beams, the plane spacing and orientation within the samples can be measured. GIWAXS measurement can provide information about crystallite size, crystallite orientation, disorder, relative degree of crystallinity and molecular packing within the unit cells.[41,43–45]

1.5.3. X-Ray based complete pole figure construction

A pole figure is a plot of the diffraction intensity of a particular reciprocal lattice plane *hkl* as a function of the polar angle χ between the substrate normal and the q_{hkl} vector. Pole figure thus can provide information about orientation distribution and the relative degree of crystallinity of the sample. Traditionally, the pole figure of bulk samples is constructed in either reflection or transmission modes using a point detector.[46–48] However, collection of data using a point detector is time consuming which could result in beam damage to the sample, particularly to thin films. Thus in this dissertation, we construct pole figures by taking advantage of the 2D detector in

order to facilitate more rapid collection of intensity across a large section of reciprocal space.[49,50] To preface our discussion, it is important to note the limitation of GIWAXS measurement. The GIWAXS 2D diffraction patterns although offer helpful information for qualitative characterization of the sample structure, it is geometrically distorted and does not reflect the true reciprocal space maps of the samples. In order to understand the distortion in GIWAXS diffraction patterns, it is useful to illustrate the sphere of crystallite orientation (orientation sphere) in reciprocal space and the Ewald sphere.

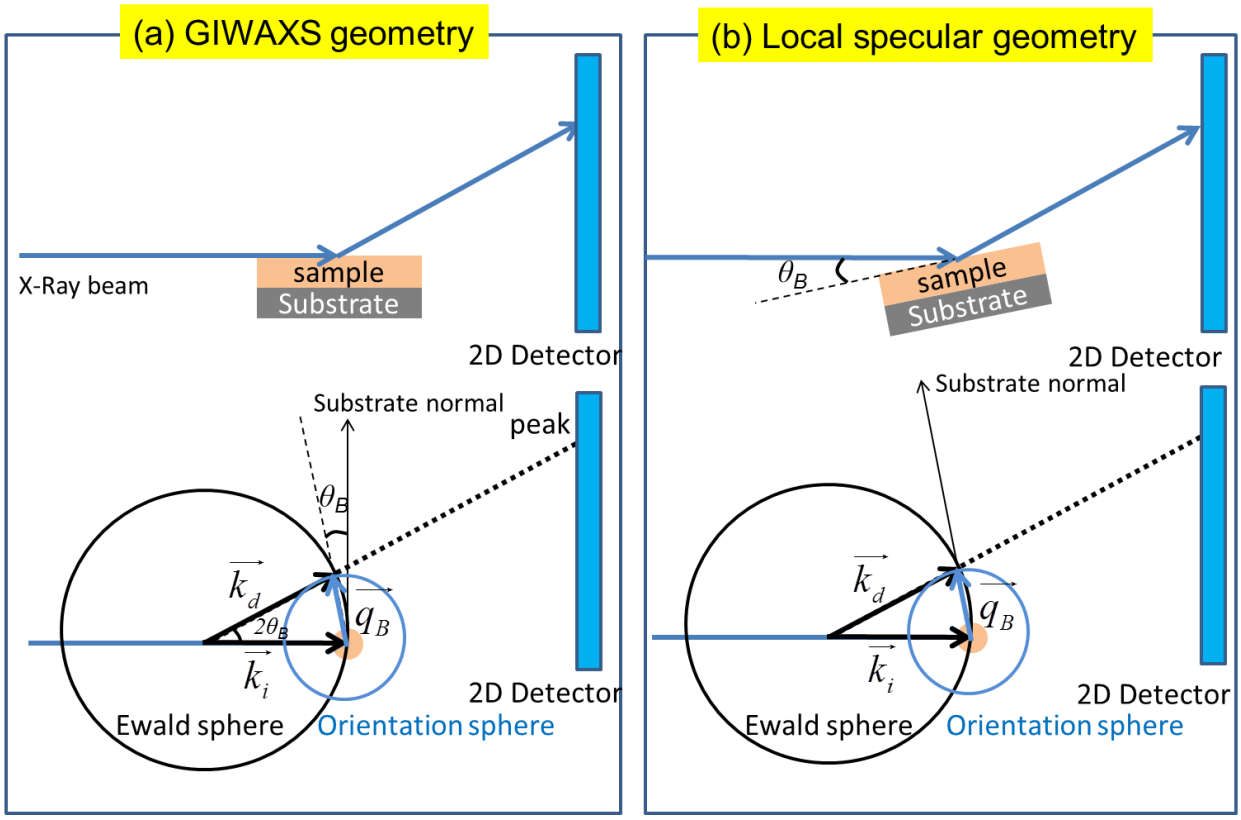

Figure 1.10: Illustrations of (a) GIWAXS geometry and (b) local specular geometry together with the construction of Ewald sphere and orientation sphere in each measurement.

Here, we define the orientation sphere of a reflection of interest as the sphere having the radius q_B and center being placed on the surface of the Ewald sphere at the head of the incoming

vector $\overrightarrow{k_i}$. Bragg law can be satisfied if the difference between the diffracted vector $\overrightarrow{k_d}$ and the incoming wave vector $\overrightarrow{k_i}$ equal to the q_B vector of the reflection of interest as:

$$\overrightarrow{q} = \overrightarrow{k_d} - \overrightarrow{k_i} = \overrightarrow{q_B} = \frac{4\pi}{\lambda}\sin\theta_B \quad (1\text{-}10)$$

In other words, the intersection between Ewald sphere and orientation sphere will result in all observable peaks in the 2D detector. As illustrated in Figure 1.10a, in GIWAXS geometry the X-ray beams are incident at very shallow angle (α almost close to zero), thus crystallites having polar angle χ smaller than the critical angle θ_B are not detectable because the Ewald sphere and orientation sphere does not intersect in this regime. In order to reveal crystallites with $\chi < \theta_B$, a local specular measurement is needed, as depicted in Figure 1.10b.[49] In local specular geometry, the sample is tilted at the critical angle $\alpha = \theta_B$. In this case, because the pole of the orientation sphere intersects with the Ewald sphere, crystallite having $\chi < \theta_B$ can be resolved. The accessible range of χ in local specular measurement is from 0 to 20°. Thus by combining partial pole figures extracted from local specular and GIWAXS measurements, the complete pole figure having the accessible range of χ from 0° to 90° can be constructed. An example of complete pole figure construction of (100) reflection in P3HT is shown in Figure 1.11.

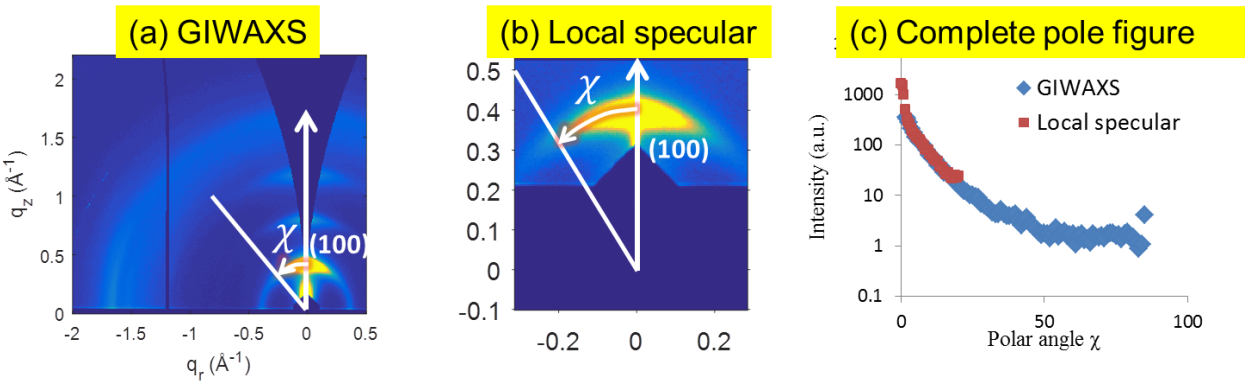

Figure 1.11: Examples of (a) GIWAXS diffraction pattern, (b) local specular diffraction pattern and (c) complete pole figure of (100) reflection constructed by combining data from local specular and GIWAXS measurements.

1.6. DISSERTATION OUTLINE

It is well accepted that the polymer's chemical structures, fabricating, processing conditions greatly affect the film morphology and consequently the film morphology strongly affect charge transport properties. The aim of this dissertation is to better understand the role of substrates, interfaces, fabricating and processing conditions on carrier transport over different length scales in order to guild improved design principles and processing conditions of materials for high performance organic semiconductor devices.

Chapter one provides a general introduction to organic semiconductors, transport mechanisms in conjugated polymer films, detailed of important experimental techniques and an outline of the dissertation. In chapter two, we investigate the role of substrate on the domain orientation and out-of-plane transport in a low-bandgap conjugated polymer. We discover that the charge carrier mobilities were not intrinsic properties of the material, but are dictated by the local morphology; they could vary by up to an order of magnitude, based on the proximity of the carrier to the substrate. The findings demonstrated the profound impact of the substrate on the morphology and of the morphology on the charge carrier mobility. Chapter three introduces a

novel processing procedure for conjugated polymer films using supercritical carbon dioxide. We will show how to use supercritical carbon dioxide processing to selectively manipulate the polymer structure near polymer/substrate interface. Subsequently, we observe a significant enhancement in the in-plane carrier mobility that is accompanied by rather a subtle change in polymer morphology. In chapter four, we will discuss the structure and carrier transport characteristics of conjugated polymer films fabricated using a novel vacuum deposition technique known as Matrix-Assisted Pulse Laser Evaporation (MAPLE). We discover that MAPLE-deposited films possess a higher degree of disorder and more random orientations of polymer crystallites compared to theirs spin-cast counterparts. Surprisingly, the seemingly unfavorable morphologies MAPLE samples are not detrimental to in-plane transport: MAPLE samples exhibit superior transport characteristics compared to spin-cast samples. In chapter five, we investigate in more detail the crystallization mechanism in MAPLE using an advanced X-Ray characterization method. We discover that despite the highly disordered morphology, in MAPLE-deposited samples there exists a large population of highly-oriented crystals at the polymer/substrate interface and that polymer layer dictates transport in MAPLE-deposited thin-film transistors. Chapter six provides conclusion and an outlined description of several on-going projects.

1.7. REFERENCES

(1) Borsenberger, P. M.; Weiss, D. S. *Organic Photoreceptors for Xerography*; CRC Press: New York, 1998.

(2) Geffroy, B.; le Roy, P.; Prat, C. Organic Light-Emitting Diode (OLED) Technology: Materials, Devices and Display Technologies. *Polym. Int.* **2006**, *55* (6), 572–582.

(3) Müllen, K.; Scherf, U. *Organic Light Emitting Devices: Synthesis, Properties and Applications*; Wiley: New York, 2006.

(4) Sirringhaus, H. 25Th Anniversary Article: Organic Field-Effect Transistors: The Path Beyond Amorphous Silicon. *Adv. Mater.* **2014**, *26* (9), 1319–1335.

(5) Günes, S.; Neugebauer, H.; Sariciftci, N. S. Conjugated Polymer-Based Organic Solar Cells. *Chem. Rev.* **2007**, *107* (4), 1324–1338.

(6) Kroon, R.; Lenes, M.; Hummelen, J. C.; Blom, P. W. M.; de Boer, B. Small Bandgap Polymers for Organic Solar Cells (Polymer Material Development in the Last 5 Years). *Polym. Rev.* **2008**, *48* (3), 531–582.

(7) Giebink, N. C.; Forrest, S. R. Quantum Efficiency Roll-off at High Brightness in Fluorescent and Phosphorescent Organic Light Emitting Diodes. *Phys. Rev. B* **2008**, *77* (23), 1–9.

(8) Newman, C. R.; Frisbie, C. D.; Demetrio, A.; Filho, S.; Bre, J. Introduction to Organic Thin Film Transistors and Design of N-Channel Organic Semiconductors. **2004**, 4436–4451.

(9) Hoth, C. N.; Schilinsky, P.; Choulis, S. a.; Brabec, C. J. Printing Highly Efficient Organic Solar Cells. *Nano Lett.* **2008**, *8* (9), 2806–2813.

(10) Hideki Shirakawa, Edwin J. Louis, Alan G. MacDiarmid, Chwan K. Chiang, A. J. H. Synthesis of Electrically Conducting Organic Polymers: Halogen Derivatives of Polyacetylene, (CH). *J. Chem. Soc. Chem. Commun.* **1977**, No. 16, 578–580.

(11) Heeger, A.; MacDiarmid, A. G.; Shirakawa, H. The Nobel Prize in Chemistry, 2000: Conductive Polymers. *Stock. Sweden R. Swedish Acad. Sci.* **2000**, 1–16.

(12) Noriega, R.; Rivnay, J.; Vandewal, K.; Koch, F. P. V; Stingelin, N.; Smith, P.; Toney, M. F.; Salleo, A. A General Relationship between Disorder, Aggregation and Charge Transport in Conjugated Polymers. *Nat. Mater.* **2013**, *12* (11), 1038–1044.

(13) Himmelberger, S.; Salleo, A. Engineering Semiconducting Polymers for Efficient Charge Transport. *MRS Commun.* **2015**, *5* (3), 383–395.

(14) Zen, A.; Saphiannikova, M.; Neher, D.; Grenzer, J.; Grigorian, S.; Pietsch, U.; Asawapirom, U.; Janietz, S.; Scherf, U.; Lieberwirth, I.; et al. Effect of Molecular Weight on the Structure and Crystallinity of poly(3-Hexylthiophene). *Macromolecules* **2006**, *39* (6), 2162–2171.

(15) Kline, R. J.; Mcgehee, M. D.; Kadnikova, E. N.; Liu, J.; Fre, J. M. J.; Toney, M. F. Dependence of Regioregular Poly (3-Hexylthiophene) Film Morphology and Field-Effect Mobility on Molecular Weight. *Macromolecules* **2005**, 3312–3319.

(16) Carlo, A. M.; Study, S.; Bassler, H. Charge Transport in Disordered Organic Photoconductors. **1993**, *15*.

(17) Bässler, H.; Köhler, A. Charge Transport in Organic Semiconductors. *Top. Curr. Chem.* **2007**, *312*, 1–65.

(18) Mozer, A.; Sariciftci, N.; Pivrikas, A.; Österbacka, R.; Juška, G.; Brassat, L.; Bässler, H. Charge Carrier Mobility in Regioregular poly(3-Hexylthiophene) Probed by Transient Conductivity Techniques: A Comparative Study. *Phys. Rev. B* **2005**, *71* (3), 35214.

(19) Hoffmann, S. T.; Jaiser, F.; Hayer, A.; Bässler, H.; Unger, T.; Athanasopoulos, S.; Neher, D.; Köhler, A. How Do Disorder, Reorganization, and Localization Influence the Hole Mobility in Conjugated Copolymers? *J. Am. Chem. Soc.* **2013**, *135* (5), 1772–1782.

(20) Spear, W. E. Transit Time Measurements of Charge Carriers in Amorphous Selenium Films. *Proc. Phys. Soc. Sect. B* **1957**, *70* (7), 669–675.

(21) Mozer, a. J.; Sariciftci, N. S.; Lutsen, L.; Vanderzande, D.; Österbacka, R.; Westerling, M.; Juška, G. Charge Transport and Recombination in Bulk Heterojunction Solar Cells Studied by the Photoinduced Charge Extraction in Linearly Increasing Voltage Technique. *Appl. Phys. Lett.* **2005**, *86* (11), 112104.

(22) Spear, W. E. Drift Mobility Techniques for the Study of Electrical Transport Properties in Insulating Solids. *J. Non. Cryst. Solids* **1969**, *1* (3), 197–214.

(23) Pivrikas, A.; Sariciftci, N. S.; Juška, G.; Österbacka, R. A Review of Charge Transport and Recombination in Polymer/Fullerene Organic Solar Cells. *Prog. PHOTOVOLTAICS Res. Appl.* **2007**, *15*, 677–696.

(24) Juška, G.; Arlauskas, K.; Viliūnas, M.; Kočka, J. Extraction Current Transients: New Method of Study of Charge Transport in Microcrystalline Silicon. *Phys. Rev. Lett.* **2000**, *84* (21), 4946–4949.

(25) Juška, G.; Arlauskas, K.; Viliūnas, M.; Genevičius, K.; Österbacka, R.; Stubb, H. Charge Transport in π-Conjugated Polymers from Extraction Current Transients. *Phys. Rev. B* **2000**, *62* (24), R16235–R16238.

(26) Österbacka, R.; Pivrikas, A.; Juška, G.; Genevičius, K.; Arlauskas, K.; Stubb, H. Mobility and Density Relaxation of Photogenerated Charge Carriers in Organic Materials. *Curr. Appl. Phys.* **2004**, *4* (5), 534–538.

(27) Juška, G.; Nekrašas, N.; Valentinavičius, V.; Meredith, P.; Pivrikas, A. Extraction of Photogenerated Charge Carriers by Linearly Increasing Voltage in the Case of Langevin Recombination. *Phys. Rev. B* **2011**, *84* (15), 155202.

(28) Dong, H.; Fu, X.; Liu, J.; Wang, Z.; Hu, W. 25th Anniversary Article: Key Points for High-Mobility Organic Field-Effect Transistors. *Adv. Mater.* **2013**, *25* (43), 6158–6183.

(29) Joseph Kline, R.; McGehee, M. D.; Toney, M. F. Highly Oriented Crystals at the Buried Interface in Polythiophene Thin-Film Transistors. *Nat. Mater.* **2006**, *5* (3), 222–228.

(30) Dinelli, F.; Murgia, M.; Levy, P.; Cavallini, M.; Biscarini, F.; De Leeuw, D. M. Spatially Correlated Charge Transport in Organic Thin Film Transistors. *Phys. Rev. Lett.* **2004**, *92* (11), 116802–1.

(31) Dong, B. X.; Amonoo, J. A.; Purdum, G. E.; Loo, Y. L.; Green, P. F. Enhancing Carrier Mobilities in Organic Thin-Film Transistors Through Morphological Changes at the Semiconductor/Dielectric Interface Using Supercritical Carbon Dioxide Processing. *ACS Appl. Mater. Interfaces* **2016**, *8* (45), 31144–31153.

(32) Chabinyc, M. L.; Salleo, A.; Wu, Y.; Liu, P.; Ong, B. S.; Heeney, M.; McCulloch, I. Lamination Method for the Study of Interfaces in Polymeric Thin Film Transistors (SI). *J. Am. Chem. Soc.* **2004**, *126* (43), 13928–13929.

(33) Campoy-Quiles, M.; Alonso, M. I.; Bradley, D. D. C.; Richter, L. J. Advanced Ellipsometric Characterization of Conjugated Polymer Films. *Adv. Funct. Mater.* **2014**, *24* (15), 2116–2134.

(34) Tompkins, H. G.; McGahan, W. A. *Spectroscopic Ellipsometry and Reflectometry: A User's Guide*; Wiley, 1999.

(35) Azzam, R. M. A.; Bashara, N. M. *Ellipsometry and Polarized Light*; North-Holland personal library; North-Holland Pub. Co., 1977.

(36) Fujiwara, H. *Spectroscopic Ellipsometry: Principles and Applications*; Wiley, 2007.

(37) Hilfiker, J. N.; Singh, N.; Tiwald, T.; Convey, D.; Smith, S. M.; Baker, J. H.; Tompkins, H. G. Survey of Methods to Characterize Thin Absorbing Films with Spectroscopic Ellipsometry. *Thin Solid Films* **2008**, *516* (22), 7979–7989.

(38) Tammer, M.; Monkman, A. P. Measurement of the Anisotropic Refractive Indices of Spin Cast Thin poly(2-Methoxy-5-(2'-ethyl-Hexyloxy)-P-Phenyl-Enevinylene) (MEH-PPV) Films. *Adv. Mater.* **2002**, *14* (3), 210–212.

(39) Gurau, M. C.; Delongchamp, D. M.; Vogel, B. M.; Lin, E. K.; Fischer, D. a; Sambasivan, S.; Richter, L. J. Measuring Molecular Order in poly(3-Alkylthiophene) Thin Films with Polarizing Spectroscopies. *Langmuir* **2007**, *23* (2), 834–842.

(40) Gundlach, D. J.; Royer, J. E.; Park, S. K.; Subramanian, S.; Jurchescu, O. D.; Hamadani, B. H.; Moad, A. J.; Kline, R. J.; Teague, L. C.; Kirillov, O.; et al. Contact-Induced Crystallinity for High-Performance Soluble Acene-Based Transistors and Circuits. *Nat. Mater.* **2008**, *7* (3), 216–221.

(41) Rivnay, J.; Mannsfeld, S. C. B.; Miller, C. E.; Salleo, A.; Toney, M. F. Quantitative Determination of Organic Semiconductor Microstructure from the Molecular to Device Scale. *Chem. Rev.* **2012**, *112* (10), 5488–5519.

(42) Vaselabadi, S. A.; Shakarisaz, D.; Ruchhoeft, P.; Strzalka, J.; Stein, G. E. Radiation Damage in Polymer Films from Grazing-Incidence X-Ray Scattering Measurements. *J. Polym. Sci. Part B Polym. Phys.* **2016**, 1–13.

(43) Salleo, A.; Kline, R. J.; DeLongchamp, D. M.; Chabinyc, M. L. Microstructural Characterization and Charge Transport in Thin Films of Conjugated Polymers. *Adv. Mater.* **2010**, *22* (34), 3812–3838.

(44) Himmelberger, S.; Duong, D. T.; Northrup, J. E.; Rivnay, J.; Koch, F. P. V.; Beckingham, B. S.; Stingelin, N.; Segalman, R. a.; Mannsfeld, S. C. B.; Salleo, A. Role of Side-Chain Branching on Thin-Film Structure and Electronic Properties of Polythiophenes. *Adv. Funct. Mater.* **2015**, *25* (17), 2616–2624.

(45) Mannsfeld, S. C. B.; Virkar, A.; Reese, C.; Toney, M. F.; Bao, Z. Precise Structure of Pentacene Monolayers on Amorphous Silicon Oxide and Relation to Charge Transport. *Adv. Mater.* **2009**, *21* (22), 2294–2298.

(46) Schulz, L. G. A Direct Method of Determining Preferred Orientation of a Flat Reflection Sample Using a Geiger Counter X-Ray Spectrometer. *J. Appl. Phys.* **1949**, *20* (11), 1030–1033.

(47) Gilbert, M.; Ross, D. H.; Bowen, a. X-Ray Pole Figures for Oriented PVC. *Polymer (Guildf).* **1999**, *40* (5), 1233–1239.

(48) Schwartz, M. Method for Obtaining Complete Quantitative Pole Figures for Flat Sheets Using One Sample and One Sample Holder. *J. Appl. Phys.* **1955**, *26* (12), 1507–1513.

(49) Baker, J. L.; Jimison, L. H.; Mannsfeld, S.; Volkman, S.; Yin, S.; Subramanian, V.; Salleo, A.; Alivisatos, A. P.; Toney, M. F. Quantification of Thin Film Crystallographic Orientation Using X-Ray Diffraction with an Area Detector. *Langmuir* **2010**, *26* (11), 9146–9151.

(50) Jimison, L. H.; Himmelberger, S.; Duong, D. T.; Rivnay, J.; Toney, M. F.; Salleo, A. Vertical Confinement and Interface Effects on the Microstructure and Charge Transport of P3HT Thin Films. *J. Polym. Sci. Part B Polym. Phys.* **2013**, *51* (7), 611–620.

Chapter 2 :NANOSCALE ORIENTATION EFFECTS ON CARRIER TRANSPORT IN A LOW-BAND-GAP POLYMER

Reprinted with permission from:

Dong, B. X.; Huang, B.; Tan, A.; Green, P. F. Nanoscale Orientation Effects on Carrier Transport in a Low-Band- Gap Polymer. *J. Phys. Chem. C* 2014, 118 (31), 17490−17498.

2.1. INTRODUCTION

Conjugated polymers (CPs) are semicrystalline, possessing amorphous regions and crystalline regions of varying orientations and volume fractions, so they are capable of exhibiting a range of morphologies that influence carrier transport.[1,2] A primary advantage of semiconducting polymers over their inorganic counterparts is that cost-effective and low-temperature processing strategies, such as spin-coating, drop casting, inkjet printing, and roll-to-roll manufacturing, may be used to prepare them for diverse applications that include xerography,[3] lighting and display applications[4–6] and solar energy applications.[7,8]

A fundamental understanding of the connection between carrier transport processes and morphology of semiconducting polymers is important to achieve effective control of quantum efficiencies in organic light emitting diodes (OLEDs),[9] switching speeds in organic field effect transistors (OFETs)[10] and carrier collection efficiencies in organic photovoltaics (OPVs).[11] Among the strategies used to measure carrier mobilities of CPs, FET configurations have been most widely used. FET configurations enable measurements of in-plane hole and electron

mobilities (i.e. transport direction parallel to the substrate) in organic semiconductors.[10] However knowledge of the out-of-plane mobilities (i.e. transport direction normal to the substrate) is important for devices such as OPVs where charge transport and extraction occur normal to the electrodes. The time-of-flight (TOF) technique is most commonly used to measure out-of-plane mobilities in organic semiconductor-based devices.[12] However, this technique is not well suited for analyzing carrier transport in films in the thickness range from nanometers to hundreds of nanometers, typically employed for devices. The space-charge-limited-current (SCLC) method has been widely used[13] to measure carrier transport in films in the thickness range not well suited for TOF measurements. However, the values of the carrier mobilities extracted from this measurement often differ significantly with those determined using TOF for films in appropriate thickness ranges, for reasons that include the nature of the contact at the electrode/organic interface, asymmetric contacts and doping.[14–16] Recently, the charge extraction by linearly increasing voltage (CELIV)[17] technique and its derivatives—the photo-CELIV[18] and metal-insulator-semiconductor (MIS)-CELIV[19] techniques—were introduced to measure the out-of-plane mobilities of CP-based devices of a range of thicknesses. The CELIV measurements provide values that are the same as those obtained using TOF measurements of films of appropriate thicknesses.

Carrier mobilities in CPs are necessarily highly anisotropic, occurring at different rates, depending on the path taken by the carriers.[20] Distortions along the backbone of a chain have the effect of reducing intrachain carrier mobilities. With regard to regioregular poly(3-hexylthiophene) (P3HT), the chain segments are packed in so-called "face-on" (π-π stacking direction) and "edge-on" packing configurations.[21] Intrachain carrier transport along the backbone segment of a chain, free of local distortions, is faster than interchain hopping transport

along the "face-on" packing direction; carrier hopping in the transverse "edge-on" direction is slowest of the three directions. The role of an underlying substrate on the structure has been shown to be responsible for a strong thickness dependence of the hole mobilities in P3HT;[22] near the substrate the molecules are organized in predominantly "edge-on" configurations, whereas at distances away from the substrate the fraction of "edge-on" configurations increase and eventually the structure becomes macroscopically anisotropic at further distances. Generally, in addition to the packing efficiencies of these lamellar aggregates, their relative orientations,[23] interconnectivities[24] and the effective conjugation lengths of polymer chains[12] have a profound impact on carrier mobilities. Understanding the connection between morphology and carrier transport is crucial for designing and optimizing the performance of CP-based devices.

In this study, we investigate charge carrier transport properties of the polymer poly[4,8-bis-((2-ethylhexyl)-oxy)-benzo[1,2-*b*:4,5-*b*']dithiophene-2,6-diyl-alt-4-(2-ethylhexan-1-one) thieno[3,4-*b*]thiophene-2,6-diyl] (PBDTTT-C).[25] With thieno[3,4-b]-thiophene and benzodithiophene alternating units, PBDTTT-C belongs to a new class of semiconducting polymers that exhibit solar power conversion efficiencies (PCEs) greater than 7%.[26,27] Although significant work has been performed to understand transport mechanisms in P3HT, to our best knowledge, no detailed study of carrier transport has been reported about this emerging class of polymers.

We show that due to a substrate-induced orientation of the local morphology in PBDTTT-C, the out-of-plane hole mobility, μ, exhibits a strong film-thickness dependence, increasing with increasing film thickness, h. Specifically, the hole mobility increased by approximately a factor of 4, within the thickness ranging from 60 to 100 nm; beyond this thickness range it remained unchanged. The temperature and electric field dependencies of μ,

measured using photoinduced charge extraction by linearly increasing voltage (photo-CELIV) and time of flight (TOF) techniques, are in agreement with predictions by the well-known Gaussian disorder model (GDM) developed to describe charge transport via a hopping mechanism in an energetically and structurally disordered medium. A negative dependence of μ on the electric field, exhibited by this polymer suggests the presence of large positional disorder, as described within the framework of the GDM. Using the combination of structural characterization techniques, we report a strong correlation between the thickness dependence of the PBDTTT-C hole mobilities and changes in the optical anisotropy of the films, quantified by the average angle of orientation θ of the planar polymer segments in relation to the underlying substrate. Specifically, at distances further removed from the substrate the average angle increased and then became constant; so the structure is macroscopically isotropic, characterized by random domain orientations, at distances sufficiently far from the substrate. In such a thickness regime, the carrier mobility was independent of film thickness. The thickness dependence of the mobility is consistent with the notion that inter and intrachain carrier mobilities are different, and therefore sensitive to microstructural features, in these conjugated polymer systems. It should, moreover, be clear that the substrate-induced effects on the local structure are responsible for the thickness dependence of the mobility.

2.2. EXPERIMENTAL

2.2.1. Materials

PBDTTT-C (M_w = 30 000 g.mol^{-1}, PDI = 1.8),[25] with chemical structure shown in Figure 2.1a, was purchased from Solarmer Energy Inc. P3HT (~95% regioregularity, M_w = 50 000 g.mol^{-1}) was purchased from Rieke Metals Inc. PEDOT–PSS (Clevios PH 500) was purchased from H.C. Starck Inc. All materials were used as received.

2.2.2 Sample Preparations

The substrates, glass, ITO-coated glass and silicon with various oxide layer thicknesses, were cleaned by ultrasonication in acetone and 2-propanol for 15 min, followed by UV-ozone cleaning for 10 min. Filtered PEDOT–PSS solutions were spin-coated onto the substrates and baked at 130°C for 20 min; the coated substrates were then transferred into a nitrogen atmosphere glovebox for next coating steps. Solutions of PBDTTT-C and P3HT were prepared by dissolving these polymers in chlorobenzene and shaken overnight; the solutions were then spin-coated onto the PEDOT:PSS substrates. The mobility measurements were performed on polymer films prepared via spin-coating on ITO-coated glass substrates. The ellipsometric measurements were performed on films supported by Si substrates possessing different thermal oxide layer thicknesses. The UV-vis measurements were performed on polymer films prepared on glass substrates.

The supported P3HT films were annealed at 150°C for 15 min. The PBDTTT-C samples, on the other hand, were analyzed as-cast, because this material performs optimally in OPV applications in its as-cast state.[25,28] We found that nevertheless the PBDTTT-C samples annealed at 150°C for 15 min exhibited the same properties as as-cast samples. Prior to the CELIV and TOF measurements, a semitransparent 15 nm of Al was vapor-deposited on top of the polymer layers. The samples were stored in the glovebox until the measurements were performed; exposure to the outside environment was minimized during transfer.

2.2.3. Hole Mobility Measurements

A BK Precision 4075 function generator was used to generate the triangle voltage for the CELIV measurements. A Keithley Source Meter 4ZA4 was used to generate the constant voltage for the TOF measurements. In both photo-CELIV and TOF experiments, light pulses of a 660

nm dye laser were applied to the Al side of the device to generate charge carriers in PBDTTT-C films. The dye laser was made from [2-[2-[4-(dimethylamino) phenyl]ethenyl]-6-methyl-4*H*-pyran-4-ylidene] propanedinitrile (DCM) (Exciton Inc.) dissolved in dimethyl sulfoxide; the dye cuvette was pumped by the second harmonic (532 nm, 4 ns) of a Nd:YAG pulsed laser (Quantel Inc.). The intensity of each laser pulse was varied from 10 to 100 μJ using a set of neutral energy filters (Thorlab Inc.) to generate reasonable transient curves for mobility calculation. For photo-CELIV, we applied a small negative voltage (~0.5 V) to compensate the built-in potential caused by the difference between Al and ITO's work functions and to ensure that the carriers would not be extracted by the built-in potential prior to the ramping voltage.[29] The photogenerated current transients were then amplified using a FEMTO amplifier and recorded by a Tektronix digital oscilloscope. All of the mobility measurements were conducted in a vacuum cryostat (Janis Inc.) at specific temperatures controlled by a Temperature Monitor (LakeShore Cryotronics). Details of mobility calculations are discussed further in the Results and Discussion.

2.2.4. Morphology Characterizations

The optical anisotropy of PBDTTT-C was measured using variable angle spectroscopic ellipsometry (VASE) (J.A. Woollam Co., M-2000). Measurements were performed on three identical films spin-coated on Si substrates; each Si substrate possessed a different thermally grown oxide layer of thicknesses (Encompass Distribution Services LLC.): 100, 500 and 1000 nm. The thermally grown SiO_2 layers were used for interference enhancement to increase the out-of-plane signal.[30] The sample structure we employed was Si/SiO_2/PEDOT/PBDTTT-C. VASE measurements were performed in the reflection mode at 5 angles: 55°, 60°, 65°, 70°, and 75°. A multisample analysis of three samples was used to increase the uniqueness of the results because of the strong correlations between the fitting parameters.[31] All the data analyses were

performed using the CompleteEASE software, provided by J. A. Woollam Co. Samples of PEDOT, before the PBDTTT-C layer was spin-coated onto each of them, were first measured to correctly determine the optical constants of PEDOT. The anisotropic model provided most reasonable description of the PEDOT's optical constants; our results were similar to those published in the literature.[32] The optical constants obtained for PBDTTT-C in the Si/SiO_2/PEDOT/PBDTTT-C configuration determined by fitting three samples simultaneously while fixing PEDOT's optical constants and thicknesses found in the previous step. The real and imaginary permittivities of the Si and the thermal oxide were taken from CompleteEASE software's library database.

2.3. RESULTS AND DISCUSSION

2.3.1. Electric Field and Temperature Dependence of Out-of-Plane Hole Mobilities

The currents in an h = 110 nm thick PBDTTT-C film, measured at different ramping rates, in a photo-CELIV experiment are plotted in Figure 2.1b and c as a function of time. There are two major contributions to the current: the displacement current $j(0) = \varepsilon\varepsilon_0 A/h$ (A is the voltage ramping rate), due to the geometric capacitance of the sample, and the drift current $\Delta j = j - j(0)$ resulting from the extraction and flow of charge carriers within the film. We note that no drift current is detected in the dark-CELIV current data, which is indicative of very low equilibrium carrier densities in PBDTTT-C at room temperature. Reasonable drift currents were measured only after illuminating the sample with a laser pulse just prior to ramping the voltage. For a typical CELIV experiment the hole mobility μ is calculated using the drift current Δj, the time t_{max} at which the current reaches a maximum value, and the voltage ramping rate A using the following equation:[33]

$$\mu = \frac{2h^2}{3At_{\max}^2(1+0.36\frac{\Delta j}{j(0)})} \qquad (2\text{-}1)$$

The parameter t_{max} is determined from the current versus time data in Figure 2.1b by fitting a polynomial curve, as shown, and identifying the maximum of the curve; time *t=0* corresponds to the initiation of the voltage ramp. $j(0)$ is identified in the figure by the horizontal line using linear fitting. However, in order to calculate the hole mobility from photo-CELIV data, eq 2-1 cannot be used because it is valid only for equilibrium carriers. More recently, Juska *et al.*[34] performed an analysis that accounted for the light absorption profile in order to appropriately interpret the current transients in photo-CELIV measurements.

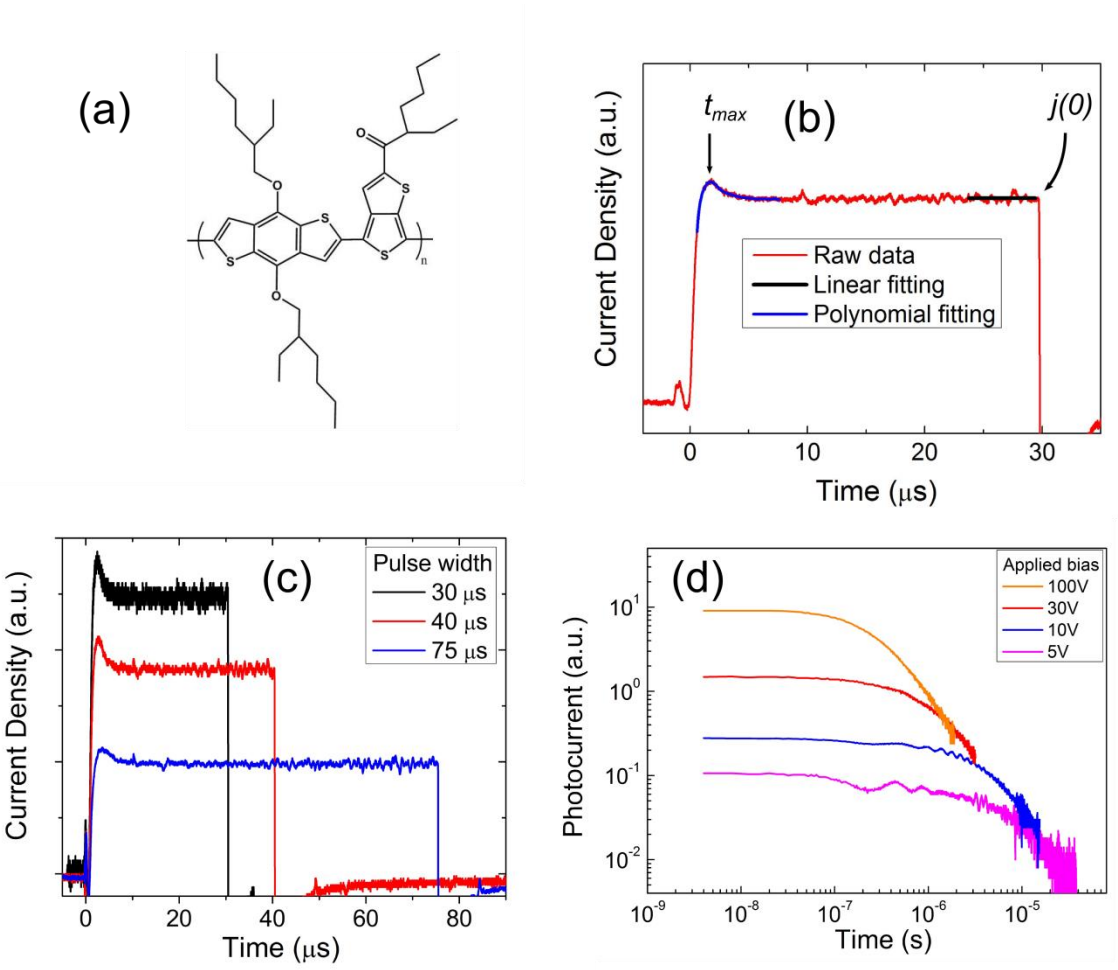

Figure 2.1(a) Chemical structure of PBDTTT-C. (b) Typical photo-CELIV curve of a PBDTTT-C film of thickness h=110 nm, obtained under conditions of a ramp height of 4 V and pulse width 30 μs is shown here. The curve drawn through the data in the range of time between 0 and 8 μs is a polynomial fit to the data. (c) Photo-CELIV curves for different ramping rates, for the same film; The ramp height was 4 V in each case. (d) Raw TOF curves for a h ~ 1 μm thick PBDTTT-C film for different values of the applied bias.

Their analysis suggests that the photogenerated carrier mobility may be calculated using the following equations:

$$\mu = K^2 \frac{2h^2}{At_{\max}^2} = (\frac{t_{\max}}{t_{tr}})^2 \frac{2h^2}{At_{\max}^2} \qquad (2\text{-}2)$$

$$e^{-\alpha h(1-t_{\max}^2/t_{tr}^2)}(1+2\alpha h t_{\max}^2/t_{tr}^2) = 1 \qquad (2\text{-}3)$$

In eq 2.2, K is a correction factor and in eq 2.3, t_{tr} is the transit time, defined as the time that a charge takes to move through the entire film thickness beginning from the surface. In eq 2.3, α is the absorption coefficient at the laser wavelength. For PBDTTT-C, the absorption coefficient at the laser's wavelength (660 nm) is calculated to be 7.7×10^{-3} nm^{-1} using our data from UV-vis absorption spectroscopy. The electric field determined from each CELIV measurement is calculated at time $t = t_{max}$, when the most of the carriers have been extracted and moving toward the counter electrode. We also determined the electric field dependence of the mobility from these measurements from ramping rate A and t_{max}, using the following equation: $E = At_{max}/h$.

Measurements of the carrier mobilities were also performed in films of thicknesses approximately one micron. These measurements were performed to confirm that, throughout appropriate thicknesses ranges, both the well-established TOF technique and the photo-CELIV technique would provide the same results. To this end, the TOF transients of a PBDTTT-C film of thickness 1 μm, determined at different applied biases, are plotted in Figure 2.1c. While the hole mobilities were measured, the laser was first pulsed to illuminate the Al side of the sample to generate a layer of charge pairs near the surface. A reverse bias U (negative side on ITO) is applied across the device to pull holes from Al toward the ITO electrode, thereby generating an induced photocurrent. Our data are consistent with dispersive transport, as normally exhibited by semiconducting polymers. The charge transit time t_{tr} was taken from the point of intersection of the asymptotes of the two linear regimes in the log–log plots of photocurrent versus time. The TOF mobility was then calculated. $\mu = h^2/(V \times t_{tr})$, for different applied biases.

The electric field dependencies of PBDTTT-C's hole mobilities, measured by both photo-CELIV and TOF at room temperature, are plotted in Figure 2.2**.** As a comparison, the measured

electric field dependence of the P3HT hole mobility in a film of comparable thickness, is also plotted in this figure. Note here that the P3HT hole mobilities were measured using CELIV, not photo-CELIV, because the equilibrium carrier densities at room temperature in P3HT are sufficient to generate a measurable signal. Our data are similar to data reported by other groups.[33] The electric field dependence of hole mobilities, plotted in Poole–Frenkel format, is in good agreement with the Poole–Frenkel relationship $\mu = \mu_{E=0}\exp(\beta E^{1/2})$, as indicated by the dashed lines in the graph.

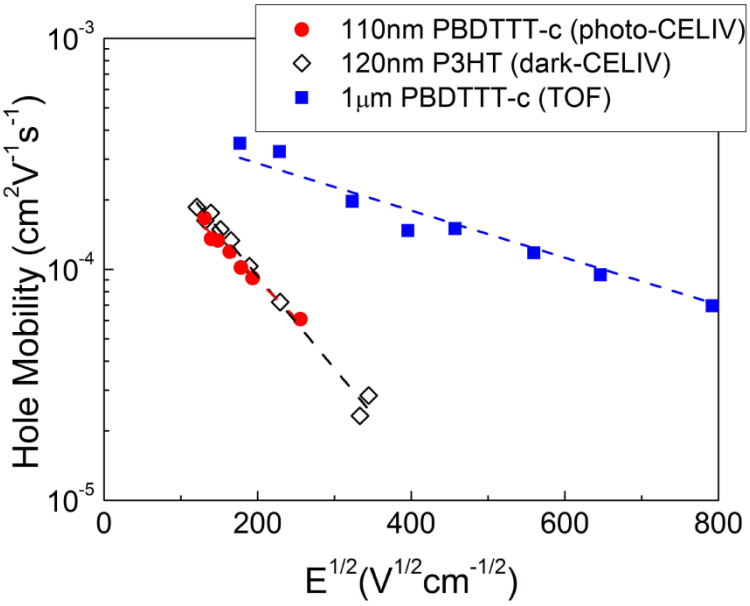

Figure 2.2: Hole mobilities in PBDTTT-C and P3HT films are plotted as a function of electric-field. The data are plotted on a semilog scale to illustrate the agreement with the Poole–Frenkel relations (dash lines).

The out-of-plane hole mobility of PBDTTT-C of thickness h = 110 nm **(**zero field mobility $\mu_{E=0} = 4.7\times10^{-4}$ cm^{2}V^{-1}s^{-1} and slope $\beta = -0.0033$ cm$^{1/2}$V$^{-1/2}$**)** happens to be comparable to that of P3HT (zero field mobility $\mu_{E=0} = 5.9\times10^{-4}$ cm^{2}V^{-1}s^{-1} and slope $\beta = -0.004$ cm$^{1/2}$V$^{-1/2}$) of comparable thickness; generally for thicker films the mobilities in P3HT are higher.[22] It is

noteworthy that at this temperature, the out-of-plane hole mobilities exhibit a negative dependence on the field.

To further understand the carrier transport process in PBDTTT-C, we investigated the electric field dependencies of out-of-plane hole mobilities at different temperatures. The results are shown in Figure 2.3a, where it is evident that negative field dependent mobilities are observed only for higher temperatures.

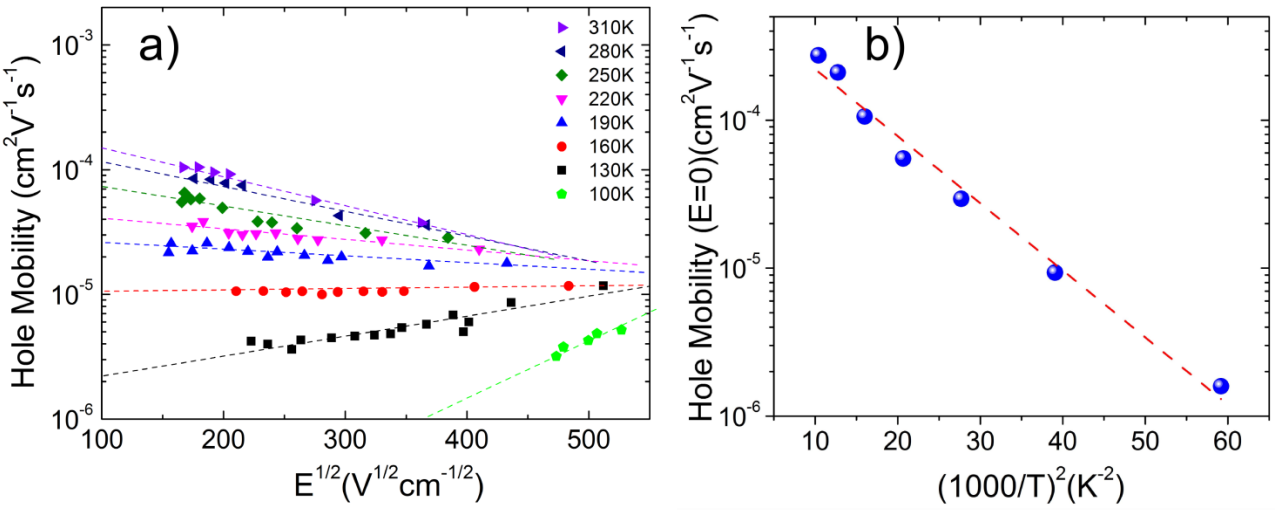

Figure 2.3: a) Electric field dependencies of the out-of-plane hole mobilities plotted for a PBDTTT-C film of thickness h = 110 nm. b) Temperature dependence of the mobilities under conditions of field $E = 0$, $\log \mu_{(E=0)}$, plotted as a function of $1/T^2$

These data in Figure 2.3 may be better understood by considering the Gaussian disorder model (GDM), developed by Bassler,[35] to describe charge transport in a disordered medium. The presence of structural disorder would be responsible for energetic disorder in polymers and therefore suggests that the GDM would provide a reasonable description of carrier transport in polymers, as discussed further below. In the GDM the charges move via a hopping mechanism in

an environment characterized by (1) positional disorder and (2) energetic disorder. Static disorder is associated with variations in interatomic distances and orientations; energetic disorder is generally associated with electrostatic coupling between the moving carriers in an environment of local fluctuating polarization. The GDM proposes an empirical equation that describes the temperature and electric field dependencies of carrier mobilities:

$$\mu(T,E) = \mu_0 e^{[-\frac{2}{3}(\frac{\sigma}{KT})^2]} e^{\{C[(\frac{\sigma}{KT})^2 - \Sigma^2]E^{1/2}\}} \quad (2\text{-}4)$$

In this equation, σ is the width of the density of states, which is assumed to be Gaussian, and characterizes the energetic disorder. Σ is a parameter that describes the positional disorder and C is a fitting parameter. The electric field dependencies of hole mobilities of PBDTTT-C's at various temperatures is well described by the Poole–Frenkel equation: $\log \mu = \log \mu_{E=0} + \beta E^{1/2}$ (see Figure 2.3). First, the log of the temperature dependence of zero field mobilities scales as $1/T^2$ (Figure 2.3b), which is consistent with a carrier hopping mechanism. Second, the parameter β decreases with increasing temperature and becomes negative at temperature above 160 K, in a manner consistent with predictions of the GDM. In light of these observations we reasonably assume that the GDM provides a very good description of our data.

The relative effects of positional and energetic disorder on carrier dynamics determine whether the field dependence of the mobility is positive or negative. If the influence of positional disorder is sufficiently weak, so that energetic disorder dominates, then a positive field dependence of mobility is observed. Such is the case for some polymers that include regiorandom P3HT,[18] poly(1,4-phenylene-1,2-diphenoxyphenylvinylene) (PPV) derivatives[36] and fluorene-based CPs.[37]

A negative field dependence of the mobility is observed when the effects of positional disorder dominate the effects of energetic disorder. When positional disorder dominates, it becomes more favorable for a carrier to follow a longer path along which transitions from one site to another are energetically more favorable than the shorter path in the direction of the field. Therefore, only under conditions of a sufficiently high electric field that the directionality induced by the electric field forces carriers to travel through energetically unfavorable sites, resulting in otherwise lower mobility. The negative field dependence effect has been observed in semicrystalline polymers such as regioregular poly(alkylthiophenes)[38,39] or in films of crystalline molecules embedded in an amorphous matrix.[40,41]

2.3.2. Thickness Dependence of Out-of-Plane Hole Mobility

The out-of-plane hole mobility-electric field dependencies of PBDTTT-C films with different thicknesses are plotted in Figure 2.4. Apart from good agreement with the Poole–Frenkel prediction, the negative dependence of mobilities on electric field is exhibited by all films.

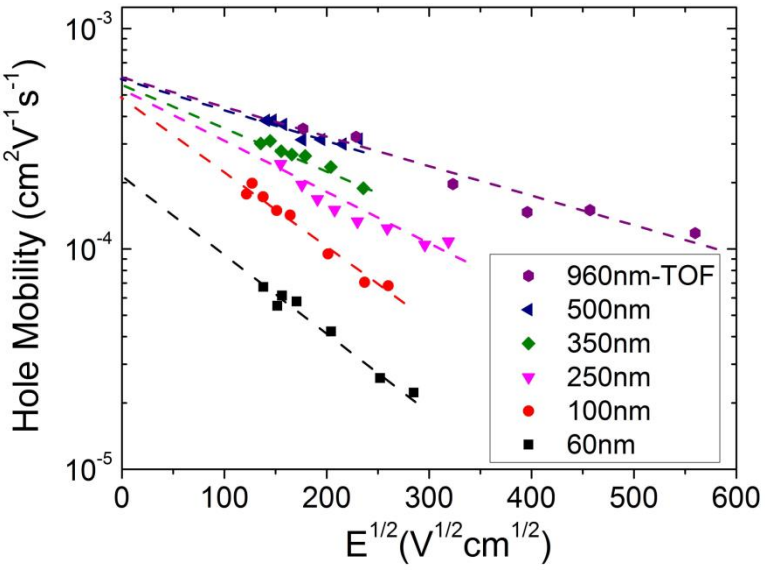

Figure 2.4: Room temperature hole mobilities for PBDTTT-C are plotted here for different thicknesses. The hole mobility for each thickness was extracted at field *E*=0, using the Poole–Frenkel relationship (dashed lines).

To gain further insight into the thickness dependence of μ, we fit the mobility using the Poole-Frenkel equation $\log \mu = \log \mu_{E=0} + \beta E^{1/2}$ and extracted the hole mobility under conditions where the field E=0. The zero-field mobilities at different thicknesses are plotted in Figure 2.5a. Interestingly, the hole mobility increases by approximately a factor of 4 throughout the thickness range from 60 to 100 nm and remains constant for thicker films. The mobilities for films of thickness h > 100 nm are in very good agreement with TOF results, represented by the blue squares. Moreover, with increasing thickness, the hole mobility of PBDTTT-C is found to depend less on the electric field (i.e., the Poole-Frenkel coefficient β becomes "less negative") as thickness increases to 350 nm and remains unchanged for thicker films (Figure 2.5b). To reconcile the thickness dependence of the transport properties in terms of polymer structure, we employ spectroscopic ellipsometry and UV–vis absorption spectroscopy to obtain more insight into the morphology of the films.

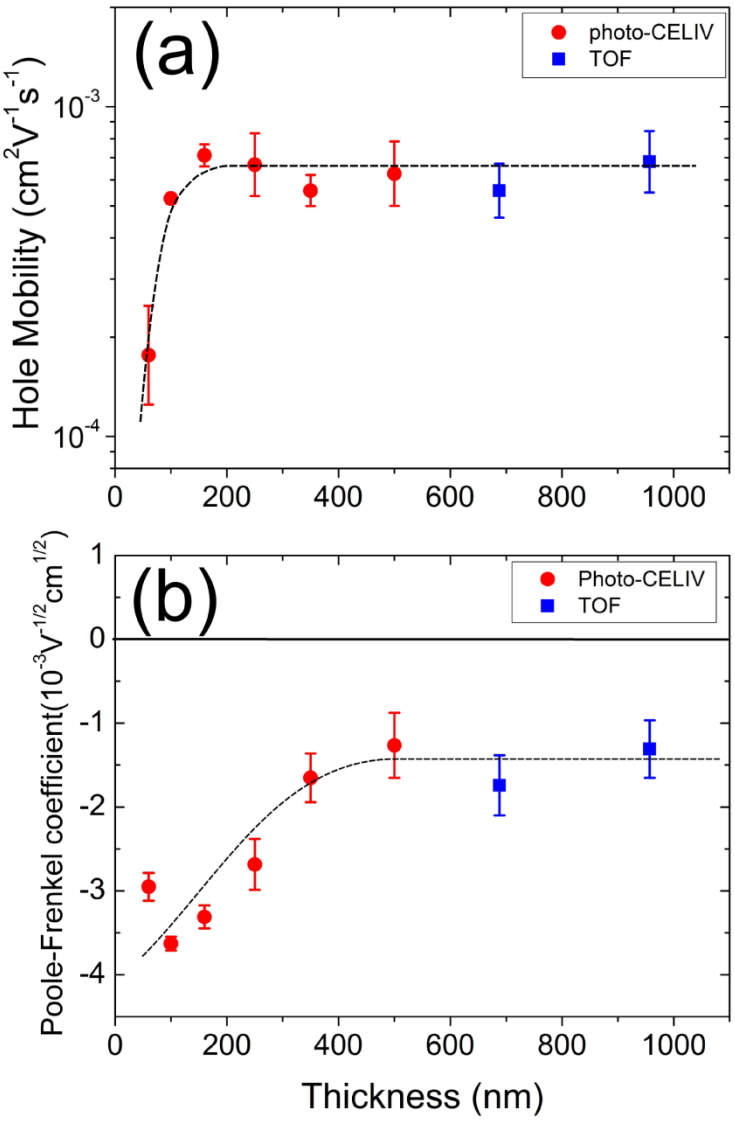

Figure 2.5: (a) PBDTTT-C hole mobilities extracted at field E=0 plotted for different thicknesses. (b) Poole–Frenkel coefficient (or the slopes of the mobility-electric field line) also plotted as a function of thicknesses. Mobilities are measured from photo-CELIV (red circle) and TOF (blue square) techniques.

Spectroscopic ellipsometry has recently emerged as a reliable method to characterize molecular order in CP thin films due to the high sensitivity and noninvasive nature of the technique.[42,43] By accurate analysis of experimental data from VASE, a rich amount of information such as polymer chain orientation,[44,45] optical anisotropy[46,47] and depth profile of

composite films[48] can be revealed. In a typical VASE measurement, the ellipsometer measures the changes in the polarization state of light after reflection from a surface at different angles and for different wavelengths. These changes in polarization state are recorded and are characterized by two ellipsometric angles Δ and Ψ. The thickness and complex permittivity of the polymer film are then obtained by fitting Δ and Ψ with an appropriate model. For all of PBDTTT-C films studied, fits using the anisotropic model always yield results with much lower mean square errors (MSEs) than the isotropic model. This is indicative of a high degree of anisotropy in PBDTTT-C films, similar to data reported from other solution-processed CPs.[31,44,49]

The imaginary parts of complex permittivities ε'' measured at different thicknesses are plotted in Figure 2.6.

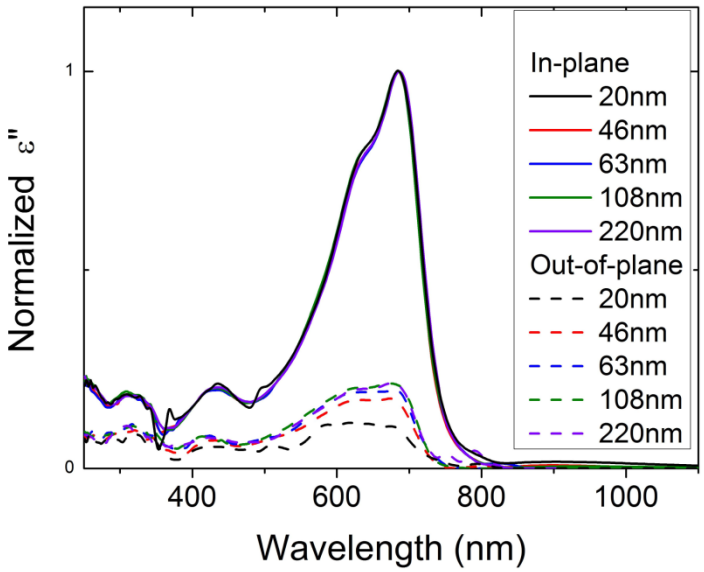

Figure 2.6: In-plane and out-of-plane imaginary permittivities ε'' of PBDTTT-C films with different thicknesses. For comparison the in-plane components are normalized to illustrate how the out-of-plane components change with thickness.

All thicknesses show weak out-of-plane, compared to in-plane, imaginary permittivities, suggesting that the conjugated backbones have an average preferential orientation parallel to the

substrate. The polymer backbone orientation with respect to the substrate can be quantified using the dichroic ratio $R = \varepsilon''_{\text{in-plane}} / \varepsilon''_{\text{out-of-plane}}$ at the position corresponding to the π–π^* transition dipole moment, since this transition dipole moment lies along the polymer chain backbone axis. The average angle of orientation θ, representing the average tilt of the polymer long chain axis with respect to the underlying substrate, is then obtained using McBranch[45] and Gurau[44] *et al.*'s approach :

$$R = 2\frac{<\sin^2\theta>}{<\cos^2\theta>} \qquad (2\text{-}5)$$

Computational calculations of this class of polymers indicate that the location of the π–π^* transition dipole moment is represented by the furthest red peak in the visible absorption spectrum.[491] Therefore the PBDTTT-C's backbone orientation is obtained by using the dichroic ratio calculated at the ~680 nm peak. Figure 2.7a shows the results of a calculation of the average angle of orientation between PBDTTT-C backbones and the substrate for different film thicknesses.

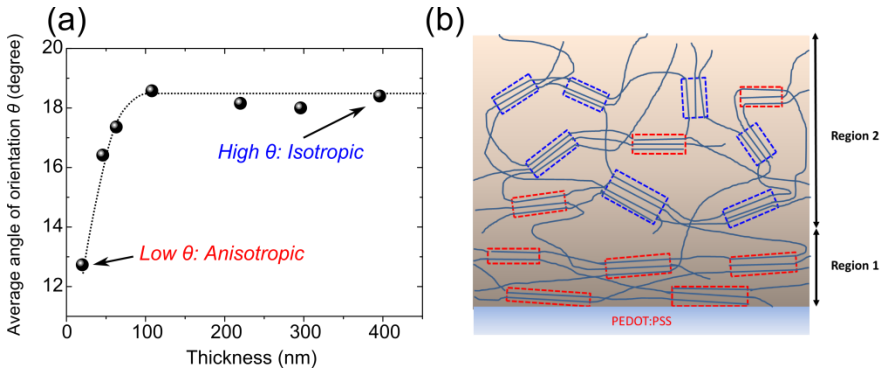

Figure 2.7: (a) Average orientation angle θ with respect to the substrate extracted from eq 5 plotted as a function of thickness and (b) illustration of polymer chains orientation throughout the film. The red rectangles contain polymer chains that orient more parallel to the substrate. The blue rectangles contain chains that have more random orientation. Near the PEDOT:PSS

substrate (i.e., region 1), most of the polymer chains orient parallel to the substrate. Further away from the substrate (i.e., region 2), the polymer chains orient more randomly.

The smallest angles are observed in the thinnest films, suggesting the highest degree of anisotropy (i.e., the predominant parallel orientation of the polymer chains with respect to the substrate), and the influence of the substrate on the average organization of the morphology. As the film thickness increases, the effect of this substrate-induced orientation diminishes and the average orientation of regions far away from the interface dominates the average orientation calculated from VASE. The increase of θ in thicker films thus reveals the tendency of polymer chains to arrange more randomly at distances further away from the substrate. These changes in polymer chain orientations throughout the film thickness are illustrated in Figure 2.7b. As the film thickness further increases above 110 nm, θ reaches a constant value of approximately 18°. We note, however, that this plateau is still below the level of a completely isotropic state. If polymer chains were oriented randomly within the film, we would have observed a value of θ to be close to the isotropic angle θ = 35.3° (at R = 1 and $<\sin^2 \theta> = 1/3$). This suggests the preference of the polymer chains to lie parallel to the substrate plane, even in the thick films. Another noticeable feature is that the shapes of in-plane and out-of-plane ε'' are similar for all films, though different in magnitude, indicating that the transitions observed in the in-plane and out-of-plane directions stem from the same microstructural origins.

The change in average orientation of the morphology with increasing film thickness is further explored using UV–vis absorption spectroscopy. Figure 2.8 shows the absorption spectra of films with different thicknesses, together with the absorption spectrum of PBDTTT-C in chlorobenzene (dashed line).

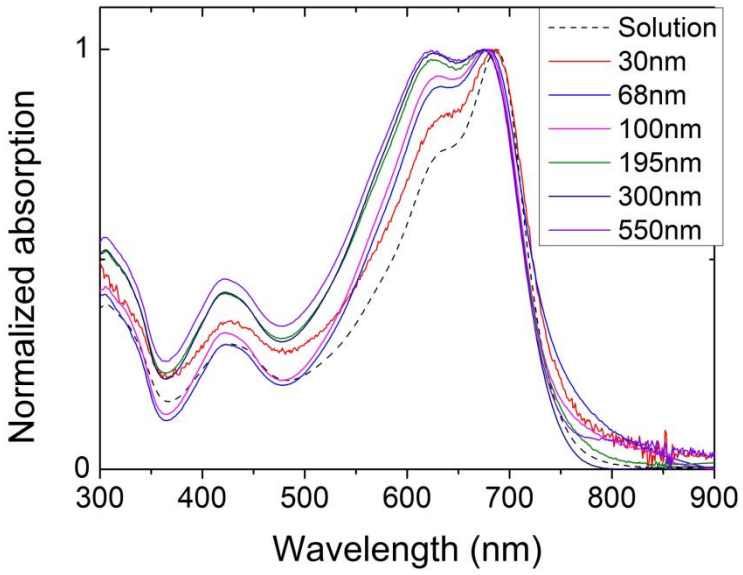

Figure 2.8: UV–vis absorption spectra of films with different thicknesses are shown here. The absorption peaks blue shifts with increasing thickness and remains unchanged at thicknesses above 300 nm

Upon increasing the film thickness from 30 to 300 nm, the absorption positions of the ~620 nm peak and the ~680 nm peak exhibit blue–shifts. Moreover, the relative intensity of the ~620 nm peak also increases with thickness. These changes are denoted by the arrows in Figure 2.8. For films of thickness h > 300 nm, the thickness dependence of the absorption spectrum disappears and the absorption shape remains unchanged for thicker films. The blue shift of absorption peaks as the thickness increases to 300 nm suggests more twisting and bending along the backbone; this naturally leads to a shorter conjugation length.

Both VASE and UV–vis absorption spectroscopies manifest discernible changes in the morphology of PBDTTT-C with increasing thickness. Interestingly, the increase of the average backbone orientation angle θ and out-of-plane hole mobility as functions of thickness are found to follow almost identical trends: both θ and the hole mobility increase until ~100 nm and remain constant beyond this threshold thickness. It is important to note that despite the decrease in

effective conjugation length, the out-of-plane hole mobility is still observed to increase with film thickness.

In conjugated polymers, a carrier would travel along a polymer chain backbone with higher probability than hopping via an interchain mechanism (e.g, π–π stacking direction in P3HT), as long as the chain is not locally twisted or distorted, leading to a localization of the carrier wave functions. The carrier is more likely to travel via an interchain mechanism (e.g., π–π stacking direction in P3HT) when the local distortion is such that the carrier localization time is sufficiently long that it becomes more favorable for inter-chain transport in the π-π stacking direction.[50,51] So in systems where the conjugation length is short, then the probability of carrier transport via an inter-chain mechanism increases. Therefore, typically, shorter conjugation lengths would be responsible for a reduction of the average distance a carrier travels along a single polymer chain without the wave function becoming localized due to a structural defect (distortion). This would lead to a reduction of the mobility.

However, recall that the chains are organized in crystalline domains and amorphous domains. The carrier would travel rapidly along the chain backbones (in the absence of local defects which could act as traps) in the crystalline domains, and in the amorphous domains the transport would be comparatively slow, due to increased disorder. Because of this the orientation of the crystalline domains becomes important. Because in the thinnest films the orientation is parallel to the substrate and in thicker films a larger fraction of the domains have a higher degree of orientation away from the substrate, the out-of-plane carrier mobility in the thickest films would be higher than in thinner films. Therefore, it is because of the structure of semicrystalline thin films (i.e., the orientation effects due to the substrate), shifts in the conjugation length are

not the best indicators of carrier mobilities. On the other hand, this would not necessarily be true for the bulk.

It is interesting to note that the change in the Poole–Frenkel coefficient β coincides with a reduction of the effective conjugation length, revealed by absorption spectroscopy. The magnitude of β decreased, approaching zero, as the thickness increased. For thicknesses $h > 300$ nm, when the absorption spectra shape become unaffected by thickness, the magnitude of β reaches a constant value. The UV–vis and ellipsometric data indicate that the structure is highly oriented near the substrate and becomes more isotropic at distances further from the substrate (the average structure of the sample exhibits a lower degree of orientation parallel to the substrate, with increasing thickness). In other words, with increasing thickness, increased random orientations of the aggregates (lamellar phases) would be consistent with θ approaching the isotropic angle of 35.3°.

Finally, the fact that the hole mobility depends less on electric field (β decreases in magnitude) with increasing thickness would be consistent with the notion that carriers traveling normal to the substrate would encounter larger barriers to transport close to the substrate, due to the high degree of aggregates oriented parallel to the substrate. These barriers to transport would decrease as the morphology becomes more isotropic as a larger fraction of aggregates would be aligned in the direction of the field, normal to the substrate, with increasing thickness. It is therefore not surprising that for film thicknesses $h > 300$ nm, when the average morphology of the film becomes independent of film thickness, as indicated by VASE and UV–vis, both the zero-field hole mobility and Poole-Frenkel coefficient β remain unchanged, independent of h.

2.4. CONCLUSION

In conclusion, we investigated the out-of-plane hole mobilities of a low-band-gap polymer, PBDTTT-C, in relation to its microstructure and predictions by the Gaussian disorder theoretical model, which describes carrier transport in disordered media. PBDTTT-C is especially interesting because in contrast to P3HT, it possesses very low intrinsic carrier densities, yet it exhibits power conversion efficiencies superior to P3HT when used as a donor polymer in OPVs. A temperature dependent study of the hole mobilities revealed that carrier transport in PBDTTT-C agrees with predictions of the Gaussian disorder model, suggesting that transport primarily occurs via a hopping mechanism, not uncommon in organic semiconductors. Using a combination of structural characterization techniques, we found that the out-of-plane hole mobilities in PBDTTT-C are correlated with the thickness-dependent morphological changes. The out-of-plane hole mobilities were lowest in the thinnest films where the average orientation of the chains (lamellar aggregate phases) was predominantly parallel to the substrate. In this thickness range the out-of-plane carrier mobilities were necessarily low and β, a measure of the strength of the field dependence of the mobility, was largest; a large β manifests the largest effect of positional disorder on the carrier transport. The hole mobility depended less on the electric field (β decreases in magnitude) with increasing thickness, due evidently to the increased degree of orientation of the domains with respect to the direction of the field (normal to the interfaces). The fact that the lamellar aggregates possess an increasingly larger degree of orientation normal to the substrate with increasing film thickness is consistent with higher carrier mobilities with increasing *h*. In short, both the conclusions drawn from the transport measurements and model and the optical characterization measurements, VASE and UV–vis, strongly support the notion of thickness dependencies of the carrier transport and the morphology.

2.5. REFERENCES

(1) Hoth, C. N.; Schilinsky, P.; Choulis, S. a.; Brabec, C. J. Printing Highly Efficient Organic Solar Cells. *Nano Lett.* **2008**, *8* (9), 2806–2813.

(2) Li, G.; Shrotriya, V.; Huang, J.; Yao, Y.; Moriarty, T.; Emery, K.; Yang, Y. High-Efficiency Solution Processable Polymer Photovoltaic Cells by Self-Organization of Polymer Blends. *Nat. Mater.* **2005**, *4* (11), 864–868.

(3) Borsenberger, P. M.; Weiss, D. S. *Organic Photoreceptors for Xerography*; CRC Press: New York, 1998.

(4) Veres, J.; Ogier, S. D.; Leeming, S. W.; Cupertino, D. C.; Khaffaf, S. M. Low-K Insulators as the Choice of Dielectrics in Organic Field-Effect Transistors. *Adv. Funct. Mater.* **2003**, *13* (3), 199–204.

(5) Akcelrud, L. Electroluminescent Polymers. *Prog. Polym. Sci.* **2003**, *28* (6), 875–962.

(6) Müllen, K.; Scherf, U. *Organic Light Emitting Devices: Synthesis, Properties and Applications*; Wiley: New York, 2006.

(7) Günes, S.; Neugebauer, H.; Sariciftci, N. S. Conjugated Polymer-Based Organic Solar Cells. *Chem. Rev.* **2007**, *107* (4), 1324–1338.

(8) Kroon, R.; Lenes, M.; Hummelen, J. C.; Blom, P. W. M.; de Boer, B. Small Bandgap Polymers for Organic Solar Cells (Polymer Material Development in the Last 5 Years). *Polym. Rev.* **2008**, *48* (3), 531–582.

(9) Giebink, N. C.; Forrest, S. R. Quantum Efficiency Roll-off at High Brightness in Fluorescent and Phosphorescent Organic Light Emitting Diodes. *Phys. Rev. B* **2008**, *77* (23), 1–9.

(10) Newman, C. R.; Frisbie, C. D.; Demetrio, A.; Filho, S.; Bre, J. Introduction to Organic Thin Film Transistors and Design of N-Channel Organic Semiconductors. **2004**, 4436–4451.

(11) Pivrikas, A.; Sariciftci, N. S.; Juška, G.; Österbacka, R. A Review of Charge Transport and Recombination in Polymer/Fullerene Organic Solar Cells. *Prog. PHOTOVOLTAICS Res. Appl.* **2007**, *15*, 677–696.

(12) Ballantyne, A. M.; Chen, L.; Dane, J.; Hammant, T.; Braun, F. M.; Heeney, M.; Duffy, W.; McCulloch, I.; Bradley, D. D. C.; Nelson, J. The Effect of Poly(3-Hexylthiophene) Molecular Weight on Charge Transport and the Performance of Polymer:Fullerene Solar Cells. *Adv. Funct. Mater.* **2008**, *18* (16), 2373–2380.

(13) Tanase, C.; Meijer, E. J.; Blom, P. W. M.; de Leeuw, D. M. Unification of the Hole Transport in Polymeric Field-Effect Transistors and Light-Emitting Diodes. *Phys. Rev. Lett.* **2003**, *91* (21), 216601.

(14) Wang, Z. B.; Helander, M. G.; Greiner, M. T.; Qiu, J.; Lu, Z. H. Carrier Mobility of

Organic Semiconductors Based on Current-Voltage Characteristics. *J. Appl. Phys.* **2010**, *107* (3).

(15) Dacuña, J.; Salleo, a. Modeling Space-Charge Limited Currents in Organic Semiconductors : Extracting Trap Density and Mobility I . Introduction. *Phys. Rev. B* **2011**, *84* (19), 195209.

(16) Kirchartz, T. Influence of Diffusion on Space-Charge-Limited Current Measurements in Organic Semiconductors. *Beilstein J. Nanotechnol.* **2013**, *4* (1), 180–188.

(17) Juska, G.; Arlauskas, K.; Viliunas, M.; Kocka, J. Extraction Current Transients: New Method of Study of Charge Transport in Microcrystalline Silicon. *Phys. Rev. Lett.* **2000**, *84* (21), 4946–4949.

(18) Österbacka, R.; Pivrikas, A.; Juška, G.; Genevičius, K.; Arlauskas, K.; Stubb, H. Mobility and Density Relaxation of Photogenerated Charge Carriers in Organic Materials. *Curr. Appl. Phys.* **2004**, *4* (5), 534–538.

(19) Armin, A.; Juska, G.; Ullah, M.; Velusamy, M.; Burn, P. L.; Meredith, P.; Pivrikas, A. Balanced Carrier Mobilities: Not a Necessary Condition for High-Efficiency Thin Organic Solar Cells as Determined by MIS-CELIV. *Adv. Energy Mater.* **2013**, n/a-n/a.

(20) Noriega, R.; Rivnay, J.; Vandewal, K.; Koch, F. P. V; Stingelin, N.; Smith, P.; Toney, M. F.; Salleo, A. A General Relationship between Disorder, Aggregation and Charge Transport in Conjugated Polymers. *Nat. Mater.* **2013**, *12* (11), 1038–1044.

(21) Sirringhaus, H.; Brown, P. J.; Friend, R. H.; Nielsen, M. M.; Bechgaard, K.; Langeveld-Voss, B. M. W.; Spiering, A. J. H.; Janssen, R. A. J.; Meijer, E. W.; Herwig, P.; et al. Two-Dimensional Charge Transport in Self-Organized, High-Mobility Conjugated Polymers. *Nature* **1999**, *401* (6754), 685–688.

(22) Huang, B.; Glynos, E.; Frieberg, B.; Yang, H.; Green, P. F. Effect of Thickness-Dependent Microstructure on the out-of-Plane Hole Mobility in poly(3-Hexylthiophene) Films. *ACS Appl. Mater. Interfaces* **2012**, *4* (10), 5204–5210.

(23) Street, R.; Northrup, J.; Salleo, A. Transport in Polycrystalline Polymer Thin-Film Transistors. *Phys. Rev. B* **2005**, *71* (16), 165202.

(24) Kline, R. J.; Mcgehee, M. D.; Kadnikova, E. N.; Liu, J.; Fre, J. M. J.; Toney, M. F. Dependence of Regioregular Poly (3-Hexylthiophene) Film Morphology and Field-Effect Mobility on Molecular Weight. *Macromolecules* **2005**, 3312–3319.

(25) Hou, J.; Chen, H.-Y.; Zhang, S.; Chen, R. I.; Yang, Y.; Wu, Y.; Li, G. Synthesis of a Low Band Gap Polymer and Its Application in Highly Efficient Polymer Solar Cells. *J. Am. Chem. Soc.* **2009**, *131* (43), 15586–15587.

(26) Liang, Y.; Wu, Y.; Feng, D.; Tsai, S.-T.; Son, H.-J.; Li, G.; Yu, L. Development of New Semiconducting Polymers for High Performance Solar Cells. *J. Am. Chem. Soc.* **2009**, *131* (1), 56–57.

(27) LIANG, Y.; YU, L. A New Class of Semiconducting Polymers for Bulk Heterojunction Solar Cells with. *Acc. Chem. Res.* **2010**, *43* (9), 1227–1236.

(28) Chen, H.; Hou, J.; Zhang, S.; Liang, Y.; Yang, G.; Yang, Y. Polymer Solar Cells with Enhanced Open-Circuit Voltage and Efficiency. *Nat. Photonics* **2009**, *3* (November), 649–653.

(29) Mozer, a. J.; Sariciftci, N. S.; Lutsen, L.; Vanderzande, D.; Österbacka, R.; Westerling, M.; Juška, G. Charge Transport and Recombination in Bulk Heterojunction Solar Cells Studied by the Photoinduced Charge Extraction in Linearly Increasing Voltage Technique. *Appl. Phys. Lett.* **2005**, *86* (11), 112104.

(30) McGahan, W. a.; Johs, B.; Woollam, J. a. Techniques for Ellipsometric Measurement of the Thickness and Optical Constants of Thin Absorbing Films. *Thin Solid Films* **1993**, *234* (1–2), 443–446.

(31) Tammer, M.; Monkman, A. P. Measurement of the Anisotropic Refractive Indices of Spin Cast Thin poly(2-Methoxy-5-(2'-ethyl-Hexyloxy)-P-Phenyl-Enevinylene) (MEH-PPV) Films. *Adv. Mater.* **2002**, *14* (3), 210–212.

(32) Pettersson, L. A. A.; Ghosh, S.; Ingan, O. Optical Anisotropy in Thin Films of Poly (3 , 4-Ethylenedioxythiophene)– Poly (4-Styrenesulfonate). **2002**, *3*, 143–148.

(33) Juška, G.; Arlauskas, K.; Viliūnas, M.; Genevičius, K.; Österbacka, R.; Stubb, H. Charge Transport in π-Conjugated Polymers from Extraction Current Transients. *Phys. Rev. B* **2000**, *62* (24), R16235–R16238.

(34) Juška, G.; Nekrašas, N.; Valentinavičius, V.; Meredith, P.; Pivrikas, A. Extraction of Photogenerated Charge Carriers by Linearly Increasing Voltage in the Case of Langevin Recombination. *Phys. Rev. B* **2011**, *84* (15), 155202.

(35) Carlo, A. M.; Study, S.; Bassler, H. Charge Transport in Disordered Organic Photoconductors. **1993**, *15*.

(36) Blom, P. W. M.; Vissenberg, M. C. J. M. Charge Transport in Poly (P-Phenylene Vinylene) Light-Emitting Diodes. *Mater. Sci. Eng.* **2000**, *27* (March), 53–94.

(37) Redecker, B. M.; Bradley, D. D. C.; Inbasekaran, M.; Wu, W. W.; Woo, E. P. High Mobility Hole Transport Fluorene- Triarylamine Copolymers. *Adv. Funct. Mater.* **1999**, *11* (3), 241–246.

(38) Mozer, A.; Sariciftci, N.; Pivrikas, A.; Österbacka, R.; Juška, G.; Brassat, L.; Bässler, H. Charge Carrier Mobility in Regioregular poly(3-Hexylthiophene) Probed by Transient Conductivity Techniques: A Comparative Study. *Phys. Rev. B* **2005**, *71* (3), 35214.

(39) Mozer, A. J.; Sariciftci, N. S. Negative Electric Field Dependence of Charge Carrier Drift Mobility in Conjugated, Semiconducting Polymers. *Chem. Phys. Lett.* **2004**, *389* (4–6), 438–442.

(40) Raj Mohan, S.; Joshi, M. P.; Singh, M. P. Negative Electric Field Dependence of Mobility

in TPD Doped Polystyrene. *Chem. Phys. Lett.* **2009**, *470* (4–6), 279–284.

(41) Auweraer, B. M. Van Der; Schryver, F. C. De; Borsenberger, P. M.; Bassler, H. Disorder in Charge Transport in Doped Polymers **. **1994**, No. 3.

(42) Campoy-Quiles, M.; Alonso, M. I.; Bradley, D. D. C.; Richter, L. J. Advanced Ellipsometric Characterization of Conjugated Polymer Films. *Adv. Funct. Mater.* **2014**, *24* (15), 2116–2134.

(43) Fujiwara, H. *Spectroscopic Ellipsometry: Principles and Applications*; Wiley, 2007.

(44) Gurau, M. C.; Delongchamp, D. M.; Vogel, B. M.; Lin, E. K.; Fischer, D. a; Sambasivan, S.; Richter, L. J. Measuring Molecular Order in poly(3-Alkylthiophene) Thin Films with Polarizing Spectroscopies. *Langmuir* **2007**, *23* (2), 834–842.

(45) McBranch, D.; Campbell, I. H.; Smith, D. L.; Ferraris, J. P. Optical Determination of Chain Orientation in Electroluminescent Polymer Films. *Appl. Phys. Lett.* **1995**, *66* (10), 1175–1177.

(46) Campoy-Quiles, M.; Etchegoin, P.; Bradley, D. On the Optical Anisotropy of Conjugated Polymer Thin Films. *Phys. Rev. B* **2005**, *72* (4), 45209.

(47) Erb, T.; Zhokhavets, U.; Gobsch, G.; Raleva, S.; Stühn, B.; Schilinsky, P.; Waldauf, C.; Brabec, C. J. Correlation Between Structural and Optical Properties of Composite Polymer/Fullerene Films for Organic Solar Cells. *Adv. Funct. Mater.* **2005**, *15* (7), 1193–1196.

(48) Campoy-Quiles, M.; Ferenczi, T.; Agostinelli, T.; Etchegoin, P. G.; Kim, Y.; Anthopoulos, T. D.; Stavrinou, P. N.; Bradley, D. D. C.; Nelson, J. Morphology Evolution via Self-Organization and Lateral and Vertical Diffusion in Polymer:fullerene Solar Cell Blends. *Nat. Mater.* **2008**, *7* (2), 158–164.

(49) Hammond, M. R.; Kline, R. J.; Herzing, A. a; Richter, L. J.; Germack, D. S.; Ro, H.-W.; Soles, C. L.; Fischer, D. a; Xu, T.; Yu, L.; et al. Molecular Order in High-Efficiency Polymer/fullerene Bulk Heterojunction Solar Cells. *ACS Nano* **2011**, *5* (10), 8248–8257.

(50) Noriega, R.; Salleo, A.; Spakowitz, A. J. Chain Conformations Dictate Multiscale Charge Transport Phenomena in Disordered Semiconducting Polymers. *Proc. Natl. Acad. Sci. U. S. A.* **2013**, *110* (41), 16315–16320.

(51) Pearson, D. S.; Pincus, P. A.; Heffner, G. W.; Dahman, S. J. Effect of Molecular Weight and Orientation on the Conductivity of Conjugated Polymers. **1993**, 1570–1575.

Chapter 3 : ENHANCING CARRIER MOBILITIES IN ORGANIC THIN-FILM TRANSISTORS THROUGH MORPHOLOGICAL CHANGES AT THE SEMICONDUCTOR/DIELECTRIC INTERFACE USING SUPERCRITCAL CARBON DIOXIDE PROCESSING

Reprinted with permission from:

Dong, B. X.; Amonoo, J. A.; Purdum, G. E.; Loo, Y. L.; Green, P. F. Enhancing Carrier Mobilities in Organic Thin-Film Transistors Through Morphological Changes at the Semiconductor/Dielectric Interface Using Supercritical Carbon Dioxide Processing. *ACS Appl. Mater. Interfaces* 2016, 8 (45), 31144–31153.

3.1. INTRODUCTION

Conjugated polymers continue to be of interest for diverse applications ranging from xerography,[1] light-emitting diodes,[2] flexible electronics[3] and solar-energy conversion[4,5] due to their mechanical flexibility,[3] solution processiblility[6] and the fact that molecular design strategies can be readily exploited to tailor their optical and electronic properties.[7,8] Charge-carrier mobility, which influences device performance in organic light-emitting diodes (OLEDs)[9], organic field-effect transistors (OFETs)[10] and organic photovoltaics (OPVs),[11] is sensitive to the thin-film morphology of conjugated polymers. A thorough understanding of the relationship between charge carrier mobility and thin-film morphology is critical for the field of organic electronics, as this information would be invaluable for improving device performance.

Poly(3-hexylthiophene) (P3HT) is one of the most commonly used conjugated polymers in organic electronics. The morphology of P3HT films is composed of crystallites, whose

orientation and size vary relative to each other, and amorphous regions. The crystallites are composed of P3HT chains stacked in both the π-π and alkyl side-chain stacking directions, forming the so-called lamella structure.[12,13] Charge transport in P3HT is highly anisotropic, as it is dictated by local chain conformation. Charge transport is most efficient along the polymer chain backbone, i.e., along the (001) direction (intrachain transport), provided the backbone is free of distortions and defects. Interchain hopping in the π-stacking direction (010) is slower, and carrier hopping in the (100) direction along the alkyl side chains is the slowest (Figure 3.1(a)).[12,14–16]

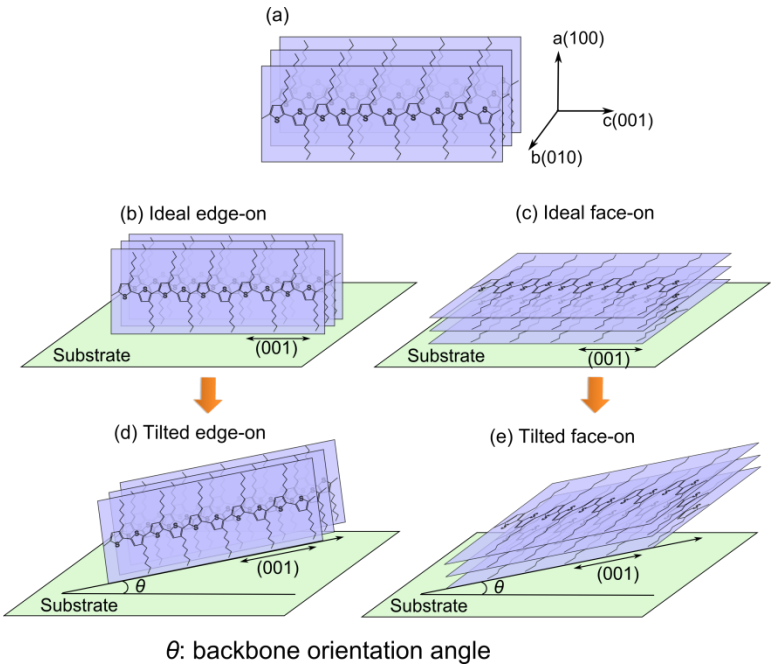

Figure 3.1: (a) Illustration of P3HT crystal structure, with side chain stacking along the a-axis, π-stacking along the b-axis and the polymer backbone direction along the c-axis. (b)(c) Ideal edge-on and face-on orientations with the c-axis parallel to the substrate. (d)(e) Possible edge-on and face-on configurations with the polymer backbone not parallel to the substrate but tilting away from it by the orientation angle θ.

In OTFT devices, in which carriers move laterally, it is generally accepted that the best transport properties are achieved when the polymer chains are preferentially oriented in an edge-

on orientation with a high degree of in-plane π-stacking (Figure 3.1(b)) as opposed to a face-on orientation (Figure 3.1(c)). The highest carrier mobilities for devices comprised of P3HT are reported under these conditions,[12,17,18] as well as for devices comprising many other high performance polymers.[19–22] Nevertheless, some notable exceptions exist; Gargi et al. reported mobilities near 0.05 $cm^2V^{-1}s^{-1}$ in devices comprised of P3HT films exhibiting a high degree of face-on stacking.[23] Moreover, many high performing polymers, such as {[N,N-9-bis(2-octyldodecyl)naphthalene-1,4,5,8-bis(dicarboximide)-2,6-diyl]- alt-5,59-(2,29-bithiophene)} [P(NDI2OD-T2)][24] and diketopyrrolopyrrole (DPP) copolymers,[25–27]adopt either a face-on or a mixture of face-on and edge-on orientations. Rivnay et al. reported dramatic transformations from face-on to edge-on orientations in P(NDI2OD-T2) thin films after thermal annealing, yet no significant changes in the device mobility were observed.[28]

The observations suggest that adopting an edge-on orientation may not be the only prerequisite for polymer thin films to achieve high in-plane device carrier mobilities as other morphological factors are likely to also influence charge transport. It is now understood that subtle changes in the packing and orientation of polymer chain segments[7,29-30], along with the stacking order and interdigitation of side groups,[31] can lead to changes in the local and long-range carrier mobilities. Specifically, the orientation of the conjugated backbone, characterized by the backbone orientation angle, θ (Figure 3.1(d) and (e)), can have a significant impact on carrier transport since carrier transport occurs both along the polymer backbone and through π-orbital overlap direction. In OTFT devices, the charge carriers are believed to travel primarily within the channel at the gate dielectric/polymer interface. Therefore, the structure the polymer adopts at this buried interface should influence the transport characteristics in TFTs.[32,33] The foregoing suggests a potential role of the backbone orientation on carrier transport in OTFTs. If

true, it would be important to find a method to control θ near the dielectric interface without significantly altering other morphological features, such as the degree of crystallinity and the polymer stacking efficiency, in order to further improve OTFT mobility.

The work of adhesion, or interfacial tension, between the polymer and the substrate should influence the chain mobility at the charge transport interface and could result in different sensitivity of the polymer film toward processing. One approach to control the strength of the interactions between the polymer chains and substrate is by treating the dielectric surface with different self-assembled monolayers (SAMs). In this manuscript, we report a strategy to control and investigate the influence of the backbone orientation on the in-plane carrier mobility of P3HT devices using post-deposition supercritical carbon dioxide ($scCO_2$) processing on P3HT thin films atop two different SAM-treated silicon dioxide substrates: octadecyltrichlorosilane (OTS) and trichloro (1H, 1H, 2H, 2H-perfluorooctyl)silane (FTS). Compared to other processing methods, such as thermal annealing,[20,34] solvent casting,[35] solvent annealing,[36,37] or sequential solvent casting,[38] $scCO_2$ processing has the advantages of being environmental-friendly, abundant and nonflammable. Additionally, the solvent quality of $scCO_2$ can be finely tuned by changing temperature (35-70ºC) and pressure (7-20MPa).[39–42]

By varying the $scCO_2$ solvent quality and treatment duration, P3HT films with different backbone orientation angles were achieved. The orientation angles θ were extracted from spectroscopic ellipsometry data using a theoretical model developed by Spano.[43] Atomic force microscopy (AFM) images of the free and buried interfaces of P3HT films indicate that $scCO_2$ preferentially changes the polymer structure at the buried interfaces. The highest carrier mobilities were measured in devices comprised of films with the highest in-plane alignments, or smallest θ. As grazing-incidence X-ray diffraction measurements indicate minimal

morphological changes in the depths of the films, our results suggest that the enhancement in carrier mobility originates from changes in backbone orientation at the dielectric interface.

3.2. EXPERIMENTAL

3.2.1. Sample Preparation

All substrates were cleaned by ultrasonication in Alconox® detergent solution, DI water, acetone, hot Hellmanex® solution, isopropanol and boiling isopropanol for 5 min each; the substrates were subsequently exposed to UV-ozone cleaning for 20 min. The substrates were then transferred to a nitrogen glovebox, where self-assembled monolayers (SAM) of either octadecyltrichlorosilane (OTS) (Gelest Inc.) or trichloro (1H, 1H, 2H, 2H-perfluorooctyl)silane (FTS) were prepared. OTS was deposited by immersing the substrates in a mixture of OTS and hexadecane (1:250 by volume) for 14 hours while stirring. FTS was deposited by placing the substrates inside a close vessel together with a small glass container filled with ca. 200 μl FTS and heating up to 150°C for 2 hours.[44,45] Unlike OTS deposition, FTS deposition was carried out in the vapor phase. The chemical structures of OTS and FTS are shown in Appendix.

Solutions of 4 mg/ml P3HT (Rieke Metal, ~95% regioregularity, M_w = 50 000 g·mol^{-1}) were prepared by dissolving the polymer in chloroform and shaken overnight before filtering. The filtered solutions were then spun onto the OTS- or FTS-treated substrates at spin-speeds of 1000 rpm for 2 min. To deposit P3HT on FTS, the solution was allowed to sit on FTS for 20-30 seconds before spin-casting due to the low surface energy of FTS. The thicknesses of the as-cast P3HT films ranged from 30 to 35 nm, as measured by ellipsometry. All samples were stored in the glovebox until the devices were made and measurements were performed; exposure to the outside environment was minimized during transfer to a separate glovebox for OTFT

measurements. All chemicals used in this study were purchased from Sigma Aldrich unless otherwise noted.

3.2.2. Supercritical Carbon Dioxide ($scCO_2$) Processing of Polymers

The solvent quality of super-critical CO_2 can be easily tuned by varying temperature and pressure. In this study, two $scCO_2$ processing conditions were chosen, as identified on the CO_2 phase diagram in Appendix. The first processing condition is at T = 35°C and P = 15 MPa, which results in a high-density CO_2 (0.8 g/mL). The second processing condition, which results in a low-density CO_2 (0.45 g/mL), is at T = 50°C and P = 10.5 MPa. The polymer films were first loaded into a stainless steel cell for $scCO_2$ annealing. Prior to annealing, the cell was twice purged with CO_2 (Cryogenic gases, purity 99.98%) to minimize the amount of air inside the cell. The entire cell was then immersed in a water bath, which had been preheated to the desired temperature using a heating circulator (Julabo Inc.). CO_2 was then introduced into the cell using a manual pressure generator (High-Pressure Equipment Co.), with the pressure being monitored with a strain gauge pressure transducer (Sensotec). After annealing, the cell was immersed in an ice bath for slow depressurization, at a rate of approximately 1.5 MPa/min.

3.2.3. Carrier Mobility Measurements

OTFTs were fabricated in top-contact, bottom-gate configurations on highly doped Si substrates with a 300 nm thermally-grown SiO_2 layer (Encompass Inc.). Source and drain gold electrodes (Kurt J. Lesker, 99.99%) were vacuum-deposited on top of the polymer film to form transistors with a channel length and width of 50 μm and 500 μm, respectively. All OTFT measurements were performed in an oxygen-free and moisture-free N_2-filled glove box using the Agilent 4156C Parameter Analyzer. The mobility μ was extracted from the current measured at

the drain (I_{DS}) by fitting the transfer curve in the saturation regime (V_D = -80 V) using the following equation:

$$I_{DS} = \frac{WC_i}{2L}\mu(V_g - V_{th})^2 \qquad (3\text{-}1)$$

In this equation, W and L are the channel width and length, C_i = 10 nF/cm^2 is the capacitance per unit area for a 300-nm thick SiO_2 layer, and V_g and V_{th} are the gate and threshold voltages, respectively.

3.2.4. Ellipsometry

Variable angle spectroscopic ellipsometry (VASE) measurements were performed using the M-2000 Ellipsometer (J. A. Woollam Co.,). The experiments were carried out on polymer films deposited using identical conditions onto two different Si substrates; one substrate with a thin layer of native oxide and the other with a layer of thermally grown SiO_2 that is 500 nm thick (Encompass Inc.). The measurements were performed in reflection mode at 55°, 60°, 65°, 70° and 75°. The data were then fit simultaneously using the CompleteEASE software, provided by J. A. Woollam Co., in order to determine the thickness and optical constants of P3HT. In order to identify the best fit for P3HT optical constants, we "built" a model such that the sample's structure was Si/SiO_2/SAM/P3HT. Before spin-coating the polymer layer, the SAM-modified substrates were measured to correctly determine the optical constants of both SAMs. The optical constants of P3HT in the Si/SiO_2/SAM/P3HT configuration were then determined by fitting two samples simultaneously, using the optical constants for the SAMs found in the previous step. The optical constants of the Si, native oxide and thermally grown SiO_2 were taken from CompleteEASE software's library database. The multi-sample analysis was necessary to increase the uniqueness of the fits due to the strong correlations between the fitting parameters.[30,46,47]

3.2.5. Grazing-incidence X-ray diffraction (GIXD)

GIXD experiments were performed on the G1 line (9.95 +/- 0.1 keV) at the Cornell High Energy Synchrotron Source. The beam was 0.05 mm tall and 1 mm wide. The x-ray beam was aligned such that it was above the critical angle of the polymer film, yet below the critical angle of the substrate. The scattered intensity was collected using a two-dimensional CCD detector, positioned 111.5 mm from the center of the sample. A background image collected from a 500 nm SiO_2 substrate has been subtracted from each image.

3.2.6. Atomic Force Microscopy (AFM)

Surface topographies of the top and buried interfaces of P3HT films were measured using an Asylum Research MFP-3D stand-alone AFM in tapping mode with a CT300-25 Aspire probe (spring constant 40 N/m and radius of curvature of 8 nm). The buried interfaces were obtained by delaminating P3HT films from the SAM-treated SiO_2 substrates using a featureless poly(dimethyl siloxane) (PDMS) (Dow Corning Sylgard 184) layer. Details of the delamination technique are reported elsewhere.[48,49]

3.3. RESULTS AND DISCUSSIONS

The in-plane hole mobilities of devices comprised of P3HT films spun on top of OTS and FTS are shown in Figure 3.2(a) as a function of high-density $scCO_2$ annealing time. The transfer curves of all devices are available in the Appendix. A clear difference between samples spun on top of OTS and FTS is observed. While the device mobilities of films cast atop OTS appear to be unaffected by $scCO_2$ processing, mobilities for devices comprised of films cast on FTS increase with processing time, saturating after approximately 1 hour. In addition to the increase in mobility for devices on FTS substrates, we observe a gradual shift of the threshold voltage toward positive values with increasing treatment time, as seen in Figure 3.2(b). The shift in

threshold voltage typically indicates a change in the interfacial dipoles or charge carriers/traps density at the dielectric/polymer interfaces.[50–52] While the exact origin of the threshold voltage shift in our work is unclear, this observation suggests that $scCO_2$ interacts and alters the structure of P3HT and/or FTS at the polymer/dielectric interface.

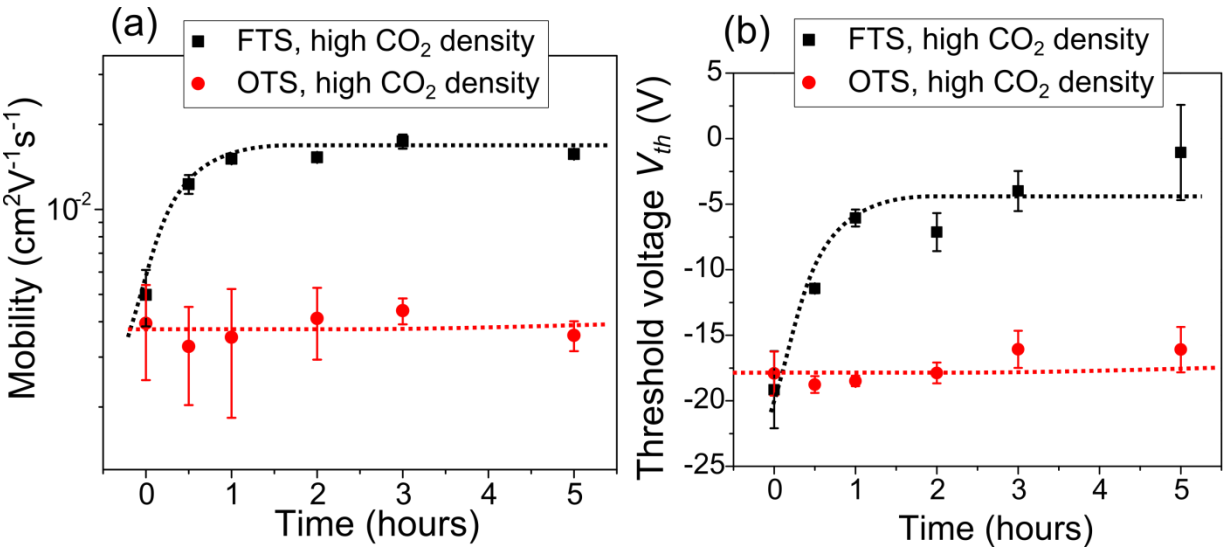

Figure 3.2: (a) In-plane hole mobilities and (b) threshold voltage as a function of CO_2 processing time. Data at $t = 0$ corresponds to as-cast samples.

In order to definitively probe whether the improved mobilities originate from changes in the structure of P3HT or FTS or both, two sets of control experiments were performed. In the first set of experiments, we anneal the P3HT/FTS films in high-density $scCO_2$ for 5 hours. Afterwards, we delaminate and transfer the annealed P3HT film onto OTS-treated Si/SiO_2 substrates. We also delaminate as-cast P3HT/FTS and transfer these films onto OTS-treated Si/SiO_2 substrates. Details of the transfer process are demonstrated in Appendix and reported elsewhere.[48,49] The mobilities of devices comprising annealed then transferred P3HT show a similar enhancement in carrier mobility compared to devices comprising as-cast then transferred P3HT. In the second set of control experiments, we anneal the FTS treated Si/SiO_2 substrates in high density $scCO_2$ for 5 hours, followed by spin-casting P3HT on top of both annealed FTS and

fresh FTS. Interestingly, we do not observe any changes in carrier mobilities between these two types of devices. In light of these observations, we believe that the enhanced mobilities observed in P3HT/FTS devices after $scCO_2$ annealing must stem from changes in the morphology of P3HT films and not changes in the structure of FTS. The transfer curves of all 4 devices together with the delamination procedures are available in the Appendix. To further understand the impact of $scCO_2$ processing on the morphology of P3HT films, VASE, GIXD, and AFM measurements were performed.

Ellipsometry measurements were carried out to determine the average backbone orientation of the polymer chains. In an ellipsometry measurement, the complex reflectance ratio (ρ) of the reflected and incident light polarization states is determined and typically presented in terms of the ellipsometric angles, Ψ and Δ. By fitting Δ and Ψ with the uniaxial anisotropic model, both the in-plane and out-of-plane extinction coefficients k can be determined. The extinction coefficient k is then converted to the absorption coefficient, α, using the equation $\alpha = 4\pi k/\lambda$ for each wavelength λ. The absorbance, A, is then calculated by multiplying α by the sample thickness d. Figure 3.3(a) depicts an example of the in-plane and the out-of-plane absorption spectra of the same P3HT film spun on top of FTS before and after annealing in high density $scCO_2$ for 5 hours.

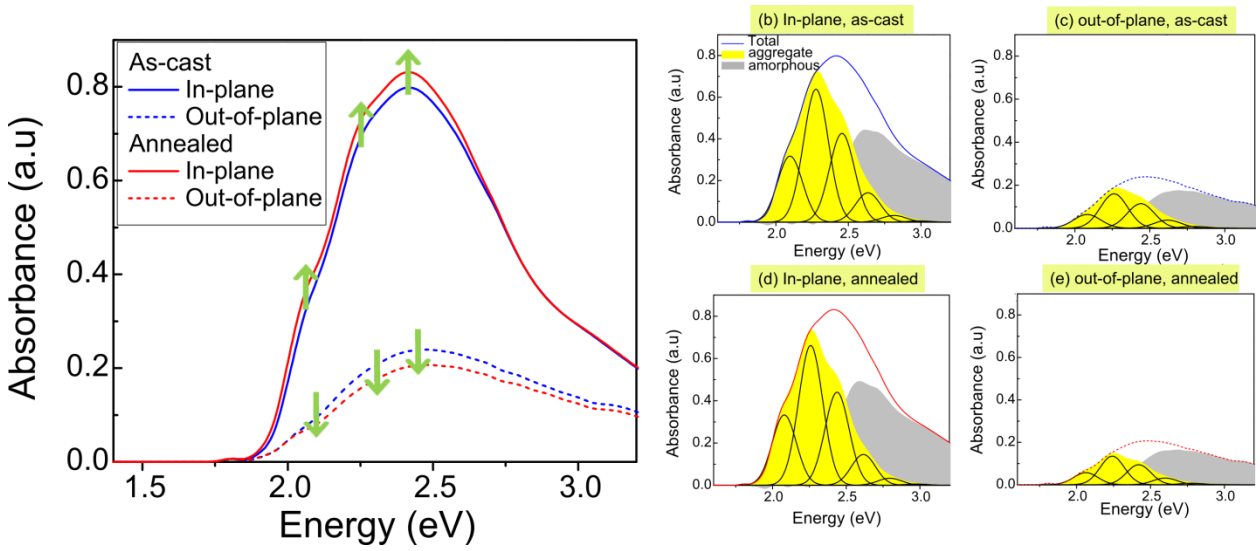

Figure 3.3: (a) An example of in-plane and out-of-plane absorption spectra of a P3HT film spun on top of FTS-treated SiO_2 measured by ellipsometry before and after annealing with high density $scCO_2$ for 5 hours. (b)(c)(d)(e) The individual in-plane and out-of-plane absorption spectra fitted using Spano Model. The aggregate part (yellow-shaded area) is fitted using equation (1). The amorphous part (gray-shaded area) is the difference between the total and the aggregate part.

Upon annealing with high-density $scCO_2$ for 5 hours, we observe enhanced absorption in the in-plane direction and reduced absorption in the out-of-plane direction, indicating that the polymer chains are more preferentially oriented parallel to the substrate after $scCO_2$ annealing. The polymer backbone orientation with respect to the substrate can be quantified using the dichroic ratio, *R*, defined by the ratio between the out-of-plane and in-plane oscillation strength at the position corresponding to the π–π^* transition dipole moment.[47,53] With respect to P3HT, the dichroic ratios at either ~2.05 eV or ~2.25 eV are normally used to calculate backbone orientation. However, because the 0-0 oscillation strength in P3HT is affected by intermolecular interactions,[43] quantification with individual peaks alone is insufficient to account for the oscillation strength of this transition. Therefore, we calculated the total oscillation strength by integrating over the entire P3HT spectrum rather than using the oscillation strength of individual

peaks. In order to deconvolute the relative contributions of the aggregate and amorphous domains from the total absorption spectra, we applied a model developed by Spano.[43,54] According to this model, the absorption spectra of P3HT thin films are composed of a low-energy regime attributed to the absorption by interchain π-stacked aggregates and a broader high-energy regime resulting from the amorphous portion of the films. At the limit of weak excitonic coupling, the cofacial interchain coupling of adjacent conjugated segments in P3HT leads to a formation of vibration bands, which can be determined using a Frank-Condon fit to the absorption spectrum as follows:

$$A_{aggregate} \propto \sum_{m=0} \left(\frac{S^m}{m!}\right) \times \left(1 - \frac{We^{-S}}{2E_p} \sum_{n \neq m} \frac{S^n}{n!(n-m)}\right)^2 \times e^{\frac{(E - E_0 - mE_p - \frac{1}{2}WS^m e^{-S})^2}{2\sigma^2}} \quad (3\text{-}2)$$

In this equation, A is the absorption of the aggregates as a function of photon energy, E; S is the Huang-Rhys factor, representing the overlap between vibrational states and assumed to be 1; m corresponds to different energy levels and E_p = 0.179 eV is the energy of C=C symmetric stretch mode. Here, the three fitting parameters are the exciton bandwidth, W, the transition energy, E_0 and the energetic disorder, σ (or the Gaussian width of the absorption peaks)**.** The fits for the aggregate region of each component using equation (3.2) are illustrated in Figure 3.3 (b-e).

As seen in Figure 3.3(b-e), the Spano model successfully reproduces the aggregate features in both the in-plane and out-of-plane absorption spectra before and after annealing. Moreover, because the amorphous spectra can be obtained from the absorption spectra, it is also possible to compute the average backbone orientation in the amorphous regions using a similar approach. We integrate the amorphous spectra in order to calculate the total oscillation strength

of the transition in the amorphous region. The average backbone orientation angle θ within the aggregate and the amorphous regions were computed using the same approach previously reported:[47,53]

$$R_{aggregate} = \frac{A_{aggregate}^{out-of-plane}}{A_{aggregate}^{in-plane}} = 2\frac{<\sin^2\theta_{aggregate}>}{<\cos^2\theta_{aggregate}>} \quad (3\text{-}3)$$

$$R_{amorphous} = \frac{A_{amorphous}^{out-of-plane}}{A_{amorphous}^{in-plane}} = 2\frac{<\sin^2\theta_{amorphous}>}{<\cos^2\theta_{amorphous}>} \quad (3\text{-}4)$$

Here, and $A_{aggregate}$ and $A_{amorphous}$ are the areas of the aggregate and amorphous spectra; and $\theta_{aggregate}$ and $\theta_{amorphous}$ are ensemble-average backbone orientation angles in the aggregate and amorphous regions, respectively. Using the aforementioned approach, we calculate the backbone orientation angles of P3HT on top of FTS and OTS after processing with $scCO_2$. Figure 3.4 shows the time evolution of both $\theta_{aggregate}$ and $\theta_{amorphous}$ under the influence of $scCO_2$ annealing, with the data at $t = 0$ corresponding to those extracted from the as-cast samples. We observe a higher orientation angle of polymer chains in the amorphous region compared with that in the aggregates, indicating that the average preferential orientation of the aggregates is more parallel to the substrate than that of the amorphous region. We note, however, that the orientation of the amorphous region is not completely random; a polymer chain oriented randomly within the film would have a value of θ close to the isotropic angle $\theta_{isotropic} = 35.3°$, corresponding to $R = 1$ and $\langle\sin^2\theta\rangle = 1/3$. The orientation angles for amorphous regions are within the range of 23° to 25°, well below this isotropic angle, suggesting that even in the amorphous region, polymer chains still have a tendency to lie parallel to the substrates. This preferential orientation in the amorphous region could be due to confinement effects in thin film, in which the polymer chains are constrained by the air/polymer and polymer/substrate.[30] Under

the influence of $scCO_2$, we see a similar decrease of $\theta_{amorphous}$ within 30 min in P3HT that had been deposited on both OTS and FTS cases. The fast response of the amorphous region is not surprising, because $scCO_2$ can penetrate and swell the amorphous regions more easily compared to their aggregate counterpart due to their lower density. The aggregate regions, on the other hand, respond slower and characteristically differently to $scCO_2$ annealing when P3HT is deposited on OTS and FTS. Figure 3.4 shows that while $scCO_2$ processing reduces $\theta_{aggregate}$ for films spun on FTS after 2 hours, it has almost no effect on $\theta_{aggregate}$ for films spun on OTS.

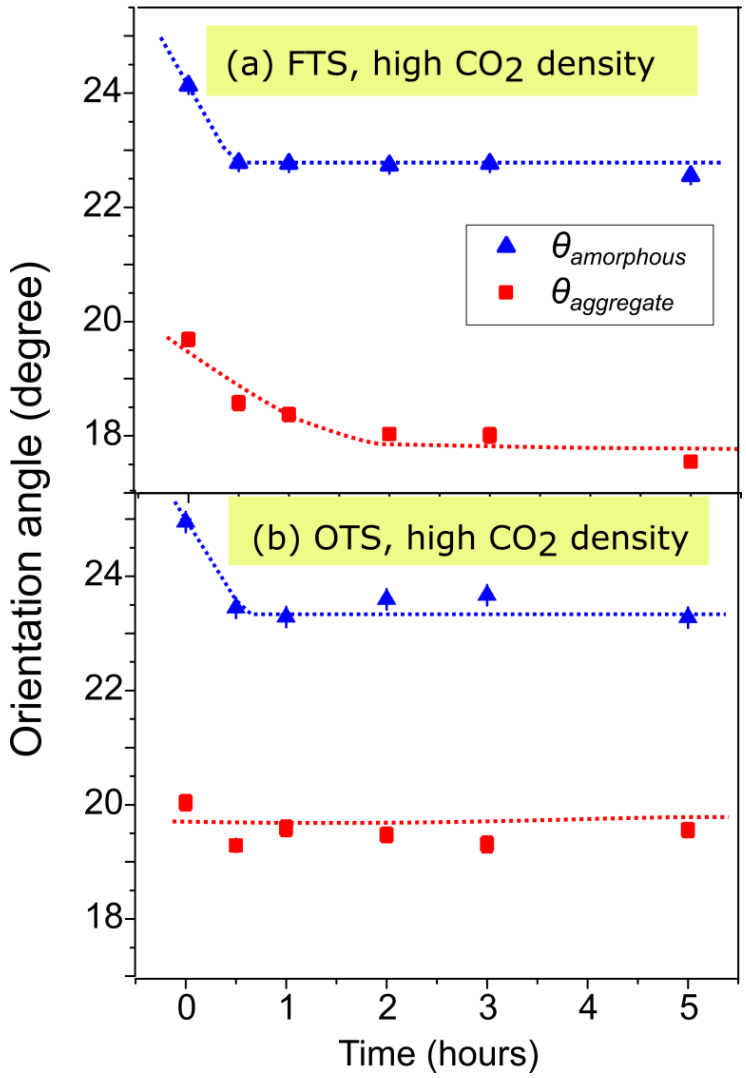

Figure 3.4: Evolution of the orientation angle θ in the aggregate and amorphous regions under the influence of $scCO_2$ fluid. The films are prepared using high density CO_2 on top of FTS (a) and OTS (b). Data at t = 0 corresponding to as-cast samples.

To illustrate the importance of the polymer backbone orientation, Figure 3.5 shows the relationship between the device mobility and the polymer backbone orientation angle. We note that on a given substrate, the mobilities and orientation angles are identical after processing with either high- or low-density $scCO_2$. We found that the hole mobilities increase with decreasing $\theta_{aggregate}$, or with the tendency of the aggregate domains to lie parallel to the substrates. We note that the significant changes in the in-plane transport characteristics are accompanied by only

subtle changes in morphology probed by ellipsometry. A mere decrease of 3° in the average backbone orientation angle results in a five-fold improvement in carrier mobility. In light of these observations, along with the observed threshold voltage shift shown Figure 3.2(b), we hypothesize that the changes might occur strictly at the P3HT/SAM interface. In order to confirm our hypothesis, we further investigate the film morphology using GIXD and AFM.

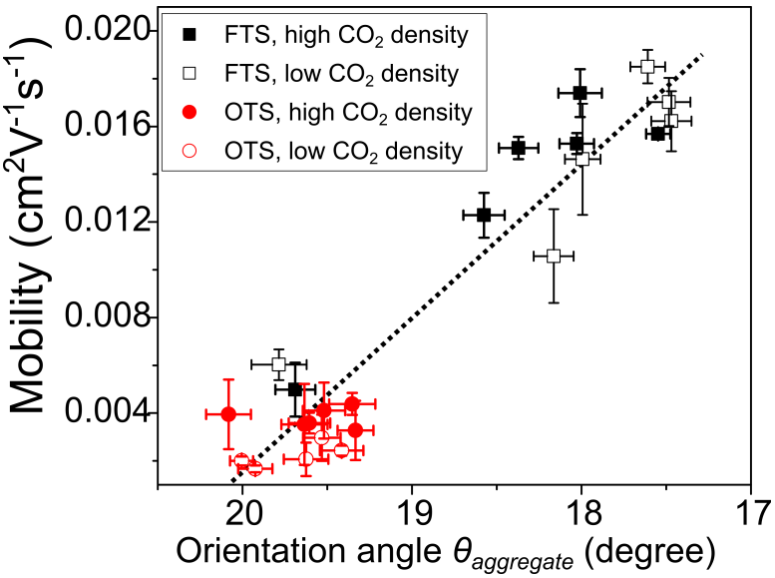

Figure 3.5: In-plane hole mobilities as a function of orientation angle for all cases studied in this work.

To investigate any changes in the bulk morphology of the films, we employed GIXD measurements on the neat P3HT films and those treated with high-density $scCO_2$ fluid for 5 hours. The two-dimensional GIXD patterns are shown in Figure 3.6(a)-(d). Figure 3.6(e), (f) show line cuts of the two-dimensional GIXD patterns taken at q_{xy} = 0 and q_z = 0, respectively, representing one-dimensional X-ray traces in the out-of-plane and in-plane directions. The traces reveal the (100) and (010) reflections at 0.40 $Å^{-1}$ and 1.7 $Å^{-1}$ respectively, consistent with a prior report on P3HT.[12] For films deposited atop either OTS-treated or FTS-treated SiO_2, the GIXD patterns show the (100) and (010) reflections along both the meridian and the equator. That the

(100) and (010) reflections are present in both the in-plane and out-of-plane traces indicates that there are at least two populations of P3HT crystallites adopting either edge-on or face-on orientations, in good agreement with previous reports on P3HT films spun from volatile solvents.[35] To further investigate the effect of $scCO_2$ processing on the structure of the P3HT films deposited atop OTS and FTS substrates, Figure 3.6(g) shows the intensity distribution of the (010) reflection as a function of the azimuthal angle. The azimuthal dependence of the (010) reflection is invariant across samples, indicating that the orientation of P3HT crystallites remain unchanged after post-deposition $scCO_2$ processing. These results suggest that bulk morphological changes cannot account for the observed increase in mobility for devices atop FTS-treated SiO_2/Si with increased $scCO_2$ annealing time.

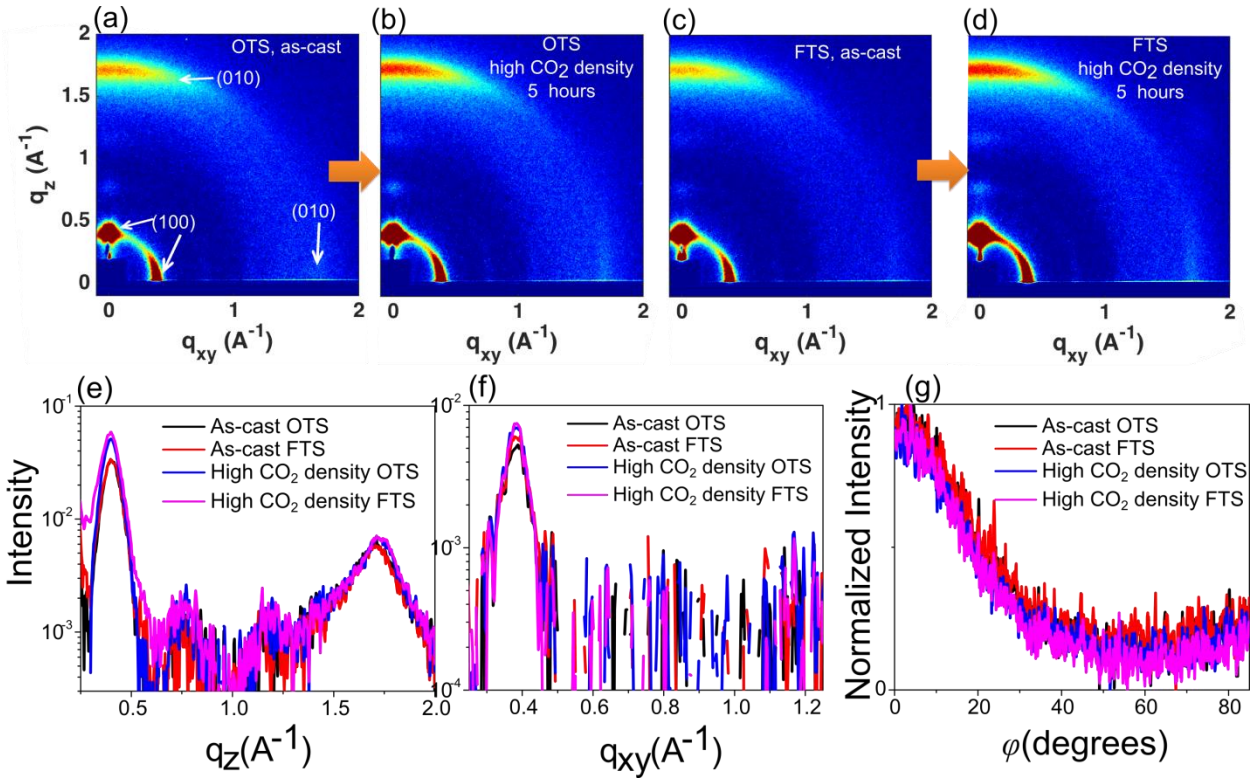

Figure 3.6: (a)-(d): Grazing-incidence X-ray diffraction (GIXD) patterns of as-cast and $scCO_2$ annealed samples spun on top of OTS and FTS. (e), (f): Intensity traces of the 4 samples along

the out-of-plane direction (q_z) and in-plane direction (q_{xy}). (g): Normalized angular distribution of (010) reflections.

As the increase in mobility with $scCO_2$ processing does not stem from the bulk morphology, we performed atomic force microscopy (AFM) on both the polymer/air interface and the buried interface of P3HT films on OTS and FTS before and after $scCO_2$ annealing. The AFM images in Figure 3.7 demonstrate that under all processing conditions and independent of dielectric surface treatment, the P3HT/air interface is featureless with no discernable differences. In sharp contrast, the buried interface of as-cast P3HT reveals distinct wrinkle structures with slightly larger features on FTS than on OTS. Upon annealing, these features are still present in films on OTS but vanish entirely for films on FTS. We note that the roughness of all surfaces here is less than 1 nm, suggesting that the observed wrinkles are not deformation or cracks induced by the delamination process.

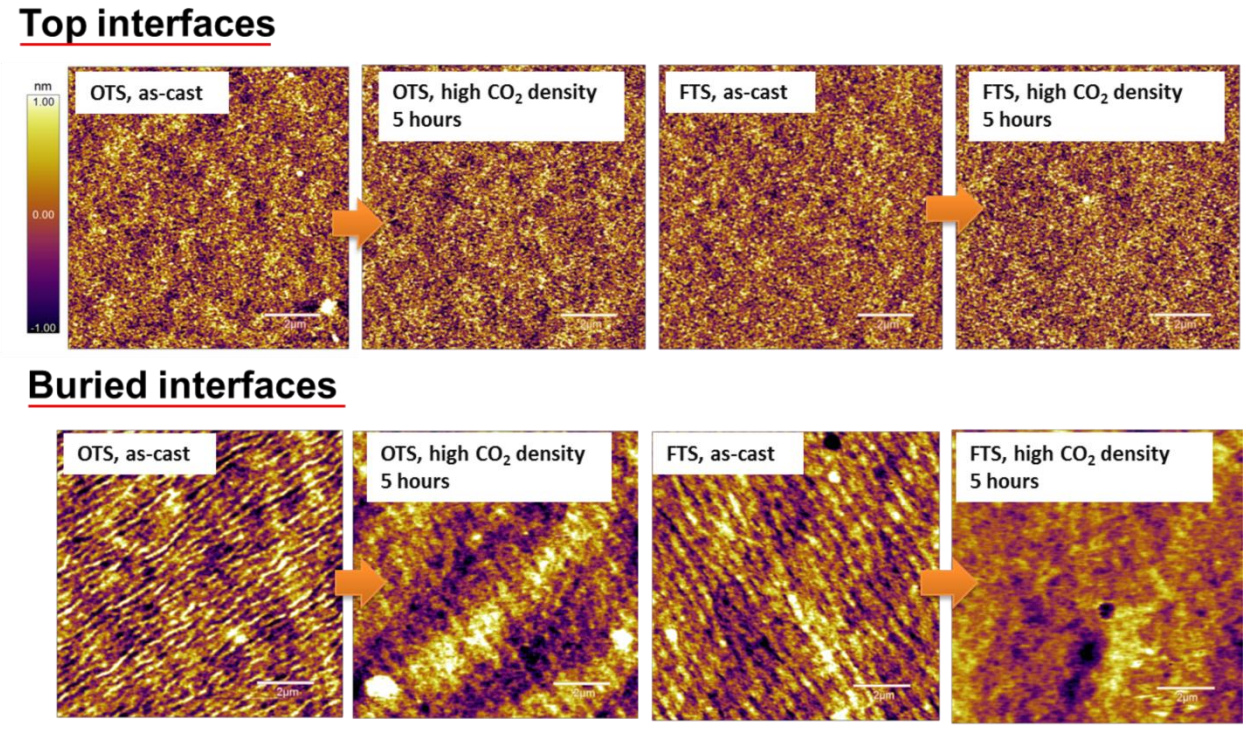

Figure 3.7: 10 x 10 μm AFM images of P3HT's top and buried interfaces, before and after $scCO_2$ annealing. The scale bar is 2 μm.

Our AFM results unambiguously indicate that $scCO_2$ annealing selectively alters the morphology of P3HT near the SAM/P3HT interface. The morphological changes in P3HT films on FTS are more significant than films on OTS, in good agreement with the ellipsometry measurements. A schematic of the film structure before and after $scCO_2$ annealing is illustrated in Figure 3.8, in which most of the changes in morphology happen close to the buried interfaces.

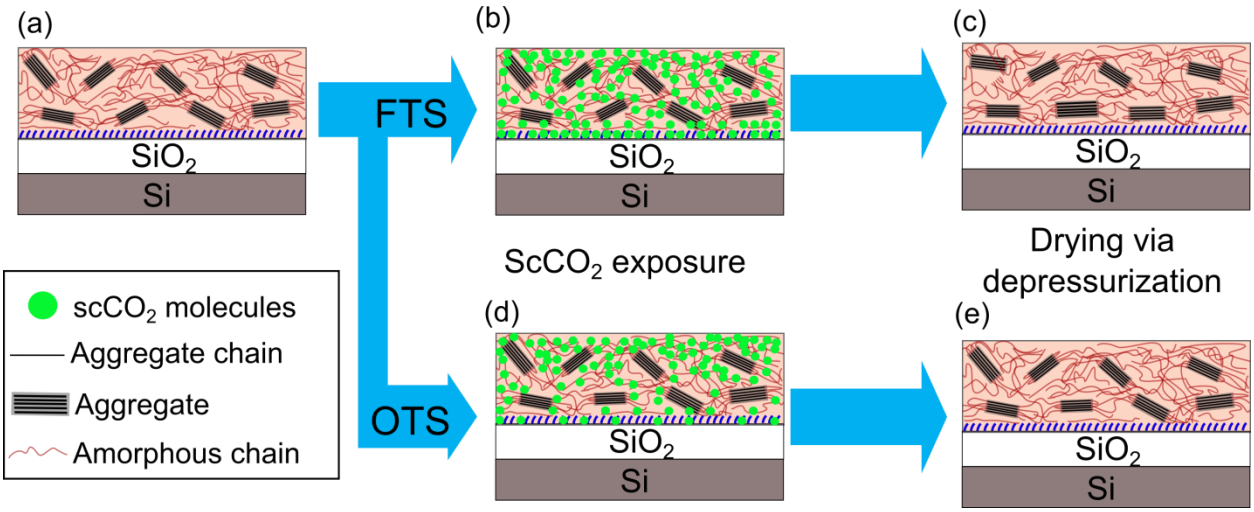

Figure 3.8: The schematic of $scCO_2$ processing on P3HT films. (a) Ascast films, spun either on OTS and FTS. (b),(d) P3HT films under exposure to $scCO_2$ fluid. (c),(e) CO_2 drying via slow depressurization. (b) and (c) are for films spun on FTS. (d) and (e) are for films spun on OTS. The low surface energy of FTS and high CO_2 density near the P3HT/FTS interface plays an important role in crystal reorganization, as illustrated in (c). On the case of OTS, $scCO_2$ processing does not influence the orientation of aggregate regions, as illustrated in (e).

The reasons for the larger morphological changes at the buried interface compared to the top interface could be understood from the following. When a film is cast onto a substrate, the chains at the polymer/substrate interface experience larger configurational entropy changes and thus higher state of stress than chains at the free surface. This hypothesis is corroborated by the observed wrinkle structure at the buried interface but rather smooth feature at the top surface. The presence of the $scCO_2$ solvent at the buried interface would lead to structural reorganization

to relax the stresses. Hence it is unsurprising that the morphological structure would show larger changes at the polymer/substrate interface than the free surface, despite the fact that the $scCO_2$ concentration near the free surface might be higher than at the bottom interface.[55] We note that for an unstable/metastable film, dewetting instabilities would generally be responsible for larger structural changes, typically evident at the free surface. The P3HT films examined here are however structurally stable.

On the other hand, the apparent difference in behavior of P3HT on top of OTS and FTS could stem from multiple reasons. First, because the interaction of any material with $scCO_2$ depends markedly on its chemical structure,[39,40] we expect that using SAMs with different affinities toward $scCO_2$ would result in different interactions and hence different polymer morphologies. The specific interaction between $scCO_2$ and the dipoles of the C-F bond lead to an increased swelling and solubility of $scCO_2$ in fluorine-containing polymers, which is well-documented in the literature.[56,57] Notably, due to their amphiphilicity in $scCO_2$, fluorine-containing copolymers have been widely used in dispersion polymerization using $scCO_2$ as reaction medium.[58,59] We hypothesize that in the presence of $scCO_2$, FTS swells more than OTS, resulting in the P3HT/FTS interface being more $scCO_2$-rich than the P3HT/OTS interface and thus enhancing $scCO_2$-P3HT interactions at the buried interface as illustrated in Figure 3.8(b) and (d). Second, fluoroalkyl compounds, such as FTS, are known to have lower surface energy than OTS due to the high electronegativity of florine.[60–62] The lower surface energy of FTS would increase the segmental mobility of polymer chains near the substrate, making the polymer chains on FTS more prone to processing compared to those on OTS. As a result, a larger morphological change after $scCO_2$ annealing is observed in samples using FTS than samples using OTS.

We have shown that charge transport strongly correlates with the polymer backbone orientation angle in aggregate domains. In a semicrystalline film, the reduced conjugation lengths and increased band gaps of the amorphous regions are responsible for reduced carrier mobilities and thus confine transport within the aggregate regions. It is suggested that the carriers only move across the amorphous regions from aggregate to aggregate via single polymer chains known as tie-molecules.[14,63,64] The orientation and molecular order within the aggregates therefore should influence charge transport. If the polymer chains within the aggregates have a low degree of in-plane alignment, a carrier would undergo inter-chain hopping in order to continue traveling laterally, resulting in lower mobilities. Carrier mobilities are significantly different for films cast on OTS and FTS, implicating the role of the backbone orientation.

Finally, we would like to point out that there exists other convincing evidence that this morphological factor is vital for carrier transport. The role of backbone orientation has been demonstrated by our previous work to be the main morphological factor affecting out-of-plane transport of the low band gap polymer poly[4,8-bis((2-ethylhexyl)-oxy) benzo[1,2-b:4,5-b′] dithiophene-2,6-diyl-alt-4-(2-ethylhexan-1-one)thieno[3,4-b]-thiophene-2,6-diyl] (PBDTTT-C).[30] Also, the degree of in-plane alignment of some high performing polymers used in OTFTs is shown to be exceptionally high, including poly[2,5-bis (3-tetradecylthiophen-2-yl)thieno[3,2-b]thiophene] (PBTTT)[19] and some high mobility diketopyrrolopyrrole (DPP) copolymers,[25] all exhibiting orientation angle $\theta < 10°$, in good agreement with our findings here.

3.4. CONCLUSION

In conclusion, we investigated the effect of $scCO_2$ processing on the structure and charge transport in P3HT films supported by two SAMs having different chemical structures and surface energies. The carrier mobilities increased five-fold in the P3HT/FTS/SiO_2 OTFTs after processing in $scCO_2$, while the carrier mobility of P3HT/OTS/SiO_2 OTFTs remained unchanged. $ScCO_2$ has a strong affinity with the C-F bonds, providing enhanced mobility to the P3HT chains at the substrate. The changes in the topography at the buried interface are consistent with the predicted enhanced solubility of polymer chains in $scCO_2$ in that region. While no noticeable effects on the structure of P3HT/OTS films were observed, the in-plane alignment of the conjugated polymer backbone in the P3HT/FTS films improved as a result of $scCO_2$ processing. A close relationship between in-plane hole mobilities and backbone orientation in P3HT was measured; the highest mobilities were measured in devices comprised of films with the highest in-plane alignments, or smallest θ. Our data suggest that possessing polymer backbone orientation more parallel to the substrate is favorable for lateral charge transport. Our work suggests an effective way to control the morphology of conjugated polymers at the semiconductor/substrate interface. Further enhancement of carrier mobilities via this benign processing method is also expected for other conjugated polymer systems, such as fluorine-containing polymers, which are known to have a strong affinity toward $scCO_2$ annealing.

3.5. APPENDIX

3.5.1. CO_2 phase diagram and the chemical structures of FTS and OTS.

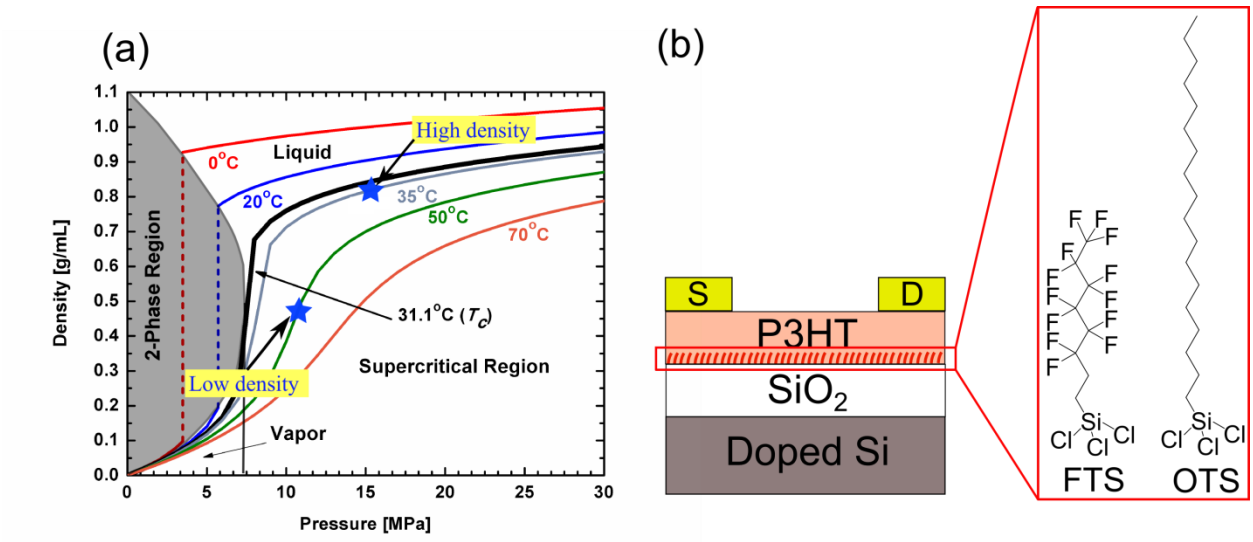

Figure 3.9. (a) Density-pressure phase diagram of pure CO_2 (Data provided by Lemmon, E. W.; McLinden, M. O.; Friend, D. G. *Thermophysical Properties of Fluid Systems.* In NIST Chemistry WebBook, NIST Standard Reference Database Number 69; Linstrom, P. J., Mallard, W. G.). The stars indicate the two pressure/temperature conditions investigated herein. (b) Schematic device structure of P3HT thin film transistors along with the chemical structure of the SAMs.

3.5.2. Transfer curves of all devices

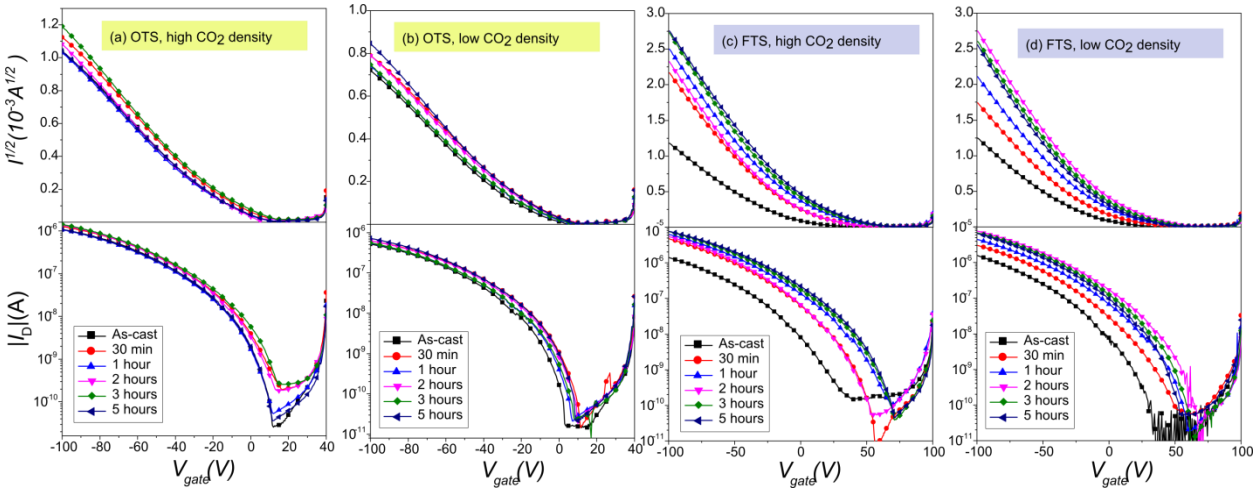

Figure 3.10. Transfer characteristics of devices fabricated on top of OTS, annealed with either (a) high or (b) low CO_2 density. Similar transfer characteristics of devices fabricated on top of FTS annealed with either (c) high or (d) low CO_2 density. The upper figures are plots of $|I|^{1/2}$ versus V_{gate} while the lower figures are plots of $\log|I|$ versus V_{gate}

3.5.3. Controlled experiments

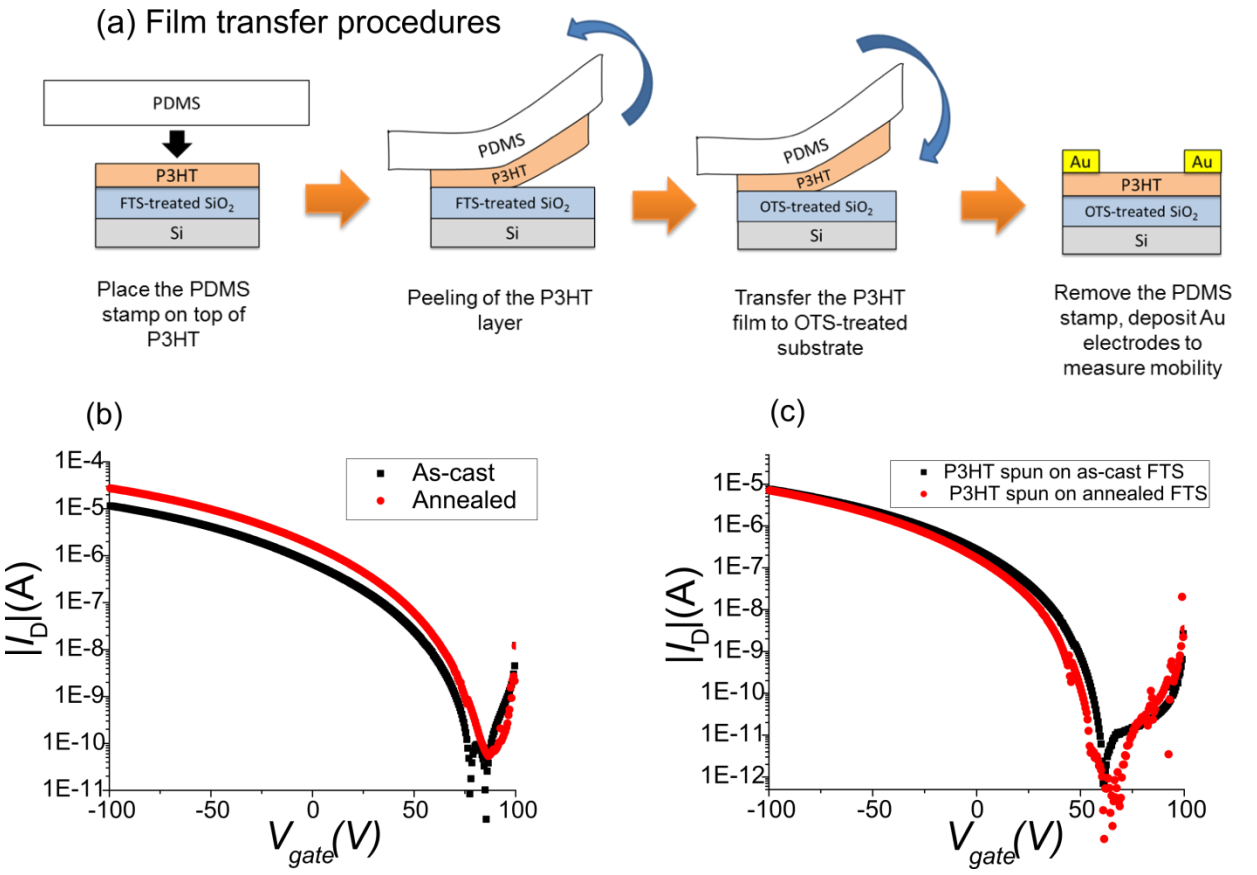

Figure 3.11. (a) Procedures of transferring films from FTS-treated substrate to OTS-treated substrate. (b) Transfer curves of P3HT device annealed on top of FTS and then transferred to the OTS substrate (red) and of as-cast P3HT spun on FTS and then transferred to OTS substrate (black). (c) Transfer curves of P3HT device spun on as-cast and annealed FTS. The annealing conditions used were 2100 psi at 35°C for 5 hours (high $scCO_2$ density)

In the first set of the control experiments, we first anneal the P3HT/FTS films and then transfer both the annealed P3HT film on FTS and the freshly fabricated P3HT film on FTS onto OTS-treated Si/SiO_2 substrates (Figure 3.11a). The mobilities of the transferred devices show similar enhancement in carrier mobility from the ascast P3HT to annealed P3HT, from 1.6 x 10^{-2} $cm^{-2}V^{-1}S^{-1}$ to 3.8 x 10^{-2} $cm^{-2}V^{-1}S^{-1}$ (Figure 3.11b). In the second set of control experiments, we anneal the FTS treated Si/SiO2 substrates, followed by spin-casting P3HT on top of both

annealed FTS and fresh FTS. The mobilities of the as-cast FTS and annealed FTS devices are 1.3 x 10^{-2} $cm^{-2}V^{-1}S^{-1}$ and 1.4 x 10^{-2} $cm^{-2}V^{-1}S^{-1}$ (Figure S3c).

3.1 REFERENCES

(1) Borsenberger, P. M.; Weiss, D. S. *Organic Photoreceptors for Xerography*; CRC Press: New York, 1998.

(2) Müllen, K.; Scherf, U. *Organic Light Emitting Devices: Synthesis, Properties and Applications*; Wiley: New York, 2006.

(3) Sekitani, T.; Zschieschang, U.; Klauk, H.; Someya, T. Flexible Organic Transistors and Circuits with Extreme Bending Stability. *Nat. Mater.* **2010**, *9* (12), 1015–1022.

(4) Günes, S.; Neugebauer, H.; Sariciftci, N. S. Conjugated Polymer-Based Organic Solar Cells. *Chem. Rev.* **2007**, *107* (4), 1324–1338.

(5) Kroon, R.; Lenes, M.; Hummelen, J. C.; Blom, P. W. M.; de Boer, B. Small Bandgap Polymers for Organic Solar Cells (Polymer Material Development in the Last 5 Years). *Polym. Rev.* **2008**, *48* (3), 531–582.

(6) Hoth, C. N.; Schilinsky, P.; Choulis, S. a.; Brabec, C. J. Printing Highly Efficient Organic Solar Cells. *Nano Lett.* **2008**, *8* (9), 2806–2813.

(7) Sirringhaus, H. 25Th Anniversary Article: Organic Field-Effect Transistors: The Path Beyond Amorphous Silicon. *Adv. Mater.* **2014**, *26* (9), 1319–1335.

(8) Dong, H.; Fu, X.; Liu, J.; Wang, Z.; Hu, W. 25th Anniversary Article: Key Points for High-Mobility Organic Field-Effect Transistors. *Adv. Mater.* **2013**, *25* (43), 6158–6183.

(9) Giebink, N. C.; Forrest, S. R. Quantum Efficiency Roll-off at High Brightness in Fluorescent and Phosphorescent Organic Light Emitting Diodes. *Phys. Rev. B* **2008**, *77* (23), 1–9.

(10) Newman, C. R.; Frisbie, C. D.; Demetrio, A.; Filho, S.; Bre, J. Introduction to Organic Thin Film Transistors and Design of N-Channel Organic Semiconductors. **2004**, 4436–4451.

(11) Pivrikas, A.; Sariciftci, N. S.; Juška, G.; Österbacka, R. A Review of Charge Transport and Recombination in Polymer/Fullerene Organic Solar Cells. *Prog. PHOTOVOLTAICS Res. Appl.* **2007**, *15*, 677–696.

(12) Sirringhaus, H.; Brown, P. J.; Friend, R. H.; Nielsen, M. M.; Bechgaard, K.; Langeveld-Voss, B. M. W.; Spiering, A. J. H.; Janssen, R. A. J.; Meijer, E. W.; Herwig, P.; et al. Two-Dimensional Charge Transport in Self-Organized, High-Mobility Conjugated Polymers. *Nature* **1999**, *401* (6754), 685–688.

(13) Rivnay, J.; Mannsfeld, S. C. B.; Miller, C. E.; Salleo, A.; Toney, M. F. Quantitative Determination of Organic Semiconductor Microstructure from the Molecular to Device Scale. *Chem. Rev.* **2012**, *112* (10), 5488–5519.

(14) Noriega, R.; Rivnay, J.; Vandewal, K.; Koch, F. P. V; Stingelin, N.; Smith, P.; Toney, M. F.; Salleo, A. A General Relationship between Disorder, Aggregation and Charge Transport in Conjugated Polymers. *Nat. Mater.* **2013**, *12* (11), 1038–1044.

(15) Noriega, R.; Salleo, A.; Spakowitz, A. J. Chain Conformations Dictate Multiscale Charge Transport Phenomena in Disordered Semiconducting Polymers. *Proc. Natl. Acad. Sci. U. S. A.* **2013**, *110* (41), 16315–16320.

(16) Pearson, D. S.; Pincus, P. A.; Heffner, G. W.; Dahman, S. J. Effect of Molecular Weight and Orientation on the Conductivity of Conjugated Polymers. **1993**, 1570–1575.

(17) Street, R.; Northrup, J.; Salleo, A. Transport in Polycrystalline Polymer Thin-Film Transistors. *Phys. Rev. B* **2005**, *71* (16), 165202.

(18) Kim, D. H.; Park, Y. D.; Jang, Y.; Yang, H.; Kim, Y. H.; Han, J. I.; Moon, D. G.; Park, S.; Chang, T.; Chang, C.; et al. Enhancement of Field-Effect Mobility due to Surface-Mediated Molecular Ordering in Regioregular Polythiophene Thin Film Transistors. *Adv. Funct. Mater.* **2005**, *15* (1), 77–82.

(19) DeLongchamp, D. M.; Kline, R. J.; Lin, E. K.; Fischer, D. a.; Richter, L. J.; Lucas, L. a.; Heeney, M.; McCulloch, I.; Northrup, J. E. High Carrier Mobility Polythiophene Thin Films: Structure Determination by Experiment and Theory. *Adv. Mater.* **2007**, *19* (6), 833–837.

(20) Jimison, L.; Salleo, A.; Chabinyc, M.; Bernstein, D.; Toney, M. Correlating the Microstructure of Thin Films of poly[5,5-bis(3-Dodecyl-2-Thienyl)-2,2-Bithiophene] with Charge Transport: Effect of Dielectric Surface Energy and Thermal Annealing. *Phys. Rev. B* **2008**, *78* (12), 125319.

(21) Chen, H.; Guo, Y.; Yu, G.; Zhao, Y.; Zhang, J.; Gao, D.; Liu, H.; Liu, Y. Highly π-Extended Copolymers with Diketopyrrolopyrrole Moieties for High-Performance Field-Effect Transistors. *Adv. Mater.* **2012**, *24* (34), 4618–4622.

(22) Cheng, C.; Yu, C.; Guo, Y.; Chen, H.; Fang, Y.; Yu, G.; Liu, Y. A Diketopyrrolopyrrole-Thiazolothiazole Copolymer for High Performance Organic Field-Effect Transistors. *Chem. Commun.* **2013**, *49* (20), 1998–2000.

(23) Gargi, D.; Kline, R. J.; DeLongchamp, D. M.; Fischer, D. a.; Toney, M. F.; O'Connor, B. T. Charge Transport in Highly Face-On Poly(3-Hexylthiophene) Films. *J. Phys. Chem. C* **2013**, *117* (34), 17421–17428.

(24) Rivnay, J.; Toney, M. F.; Zheng, Y.; Kauvar, I. V.; Chen, Z.; Wagner, V.; Facchetti, A.; Salleo, A. Unconventional Face-on Texture and Exceptional in-Plane Order of a High Mobility N-Type Polymer. *Adv. Mater.* **2010**, *22* (39), 4359–4363.

(25) Zhang, X.; Richter, L. J.; DeLongchamp, D. M.; Kline, R. J.; Hammond, M. R.; McCulloch, I.; Heeney, M.; Ashraf, R. S.; Smith, J. N.; Anthopoulos, T. D.; et al. Molecular Packing of High-Mobility Diketo Pyrrolo-Pyrrole Polymer Semiconductors with Branched Alkyl Side Chains. *J. Am. Chem. Soc.* **2011**, *133* (38), 15073–15084.

(26) Lee, J.; Han, a. R.; Kim, J.; Kim, Y.; Oh, J. H.; Yang, C. Solution-Processable Ambipolar Diketopyrrolopyrrole-Selenophene Polymer with Unprecedentedly High Hole and

Electron Mobilities. *J. Am. Chem. Soc.* **2012**, *134* (51), 20713–20721.

(27) Lee, J.; Han, A. R.; Yu, H.; Shin, T. J.; Yang, C.; Oh, J. H. Boosting the Ambipolar Performance of Solution-Processable Polymer Semiconductors via Hybrid Side-Chain Engineering. *J. Am. Chem. Soc.* **2013**, *135* (25), 9540–9547.

(28) Rivnay, J.; Steyrleuthner, R.; Jimison, L. H.; Casadei, A.; Chen, Z.; Toney, M. F.; Facchetti, A.; Neher, D.; Salleo, A. Drastic Control of Texture in a High Performance N-Type Polymeric Semiconductor and Implications for Charge Transport. *Macromolecules* **2011**, *44* (13), 5246–5255.

(29) Zhang, X.; Bronstein, H.; Kronemeijer, A. J.; Smith, J.; Kim, Y.; Kline, R. J.; Richter, L. J.; Anthopoulos, T. D.; Sirringhaus, H.; Song, K.; et al. Molecular Origin of High Field-Effect Mobility in an Indacenodithiophene-Benzothiadiazole Copolymer. *Nat. Commun.* **2013**, *4*, 2238.

(30) Dong, B. X.; Huang, B.; Tan, A.; Green, P. F. Nanoscale Orientation Effects on Carrier Transport in a Low-Band- Gap Polymer. *J. Phys. Chem. C* **2014**, *118* (31), 17490–17498.

(31) McCulloch, I.; Heeney, M.; Bailey, C.; Genevicius, K.; Macdonald, I.; Shkunov, M.; Sparrowe, D.; Tierney, S.; Wagner, R.; Zhang, W.; et al. Liquid-Crystalline Semiconducting Polymers with High Charge-Carrier Mobility. *Nat. Mater.* **2006**, *5* (4), 328–333.

(32) Dinelli, F.; Murgia, M.; Levy, P.; Cavallini, M.; Biscarini, F.; De Leeuw, D. M. Spatially Correlated Charge Transport in Organic Thin Film Transistors. *Phys. Rev. Lett.* **2004**, *92* (11), 116802–1.

(33) Joseph Kline, R.; McGehee, M. D.; Toney, M. F. Highly Oriented Crystals at the Buried Interface in Polythiophene Thin-Film Transistors. *Nat. Mater.* **2006**, *5* (3), 222–228.

(34) Cho, S.; Lee, K.; Yuen, J.; Wang, G.; Moses, D.; Heeger, A. J.; Surin, M.; Lazzaroni, R. Thermal Annealing-Induced Enhancement of the Field-Effect Mobility of Regioregular poly(3-Hexylthiophene) Films. *J. Appl. Phys.* **2006**, *100* (11), 114503.

(35) Chang, J.-F.; Sun, B.; Breiby, D. W.; Nielsen, M. M.; Sölling, T. I.; Giles, M.; McCulloch, I.; Sirringhaus, H. Enhanced Mobility of Poly(3-Hexylthiophene) Transistors by Spin-Coating from High-Boiling-Point Solvents. *Chem. Mater.* **2004**, *16* (23), 4772–4776.

(36) Kim, D. H.; Park, Y. D.; Jang, Y.; Kim, S.; Cho, K. Solvent Vapor-Induced Nanowire Formation in poly(3-Hexylthiophene) Thin Films. *Macromol. Rapid Commun.* **2005**, *26* (10), 834–839.

(37) Fu, Y.; Lin, C.; Tsai, F. Y. High Field-Effect Mobility from poly(3-Hexylthiophene) Thin-Film Transistors by Solvent-Vapor-Induced Reflow. *Org. Electron.* **2009**, *10* (5), 883–888.

(38) Kim, S.; Kang, B.; Lee, M.; Lee, S. G.; Cho, K.; Yang, H.; Park, Y. D. Sequential Solvent Casting for Improving the Structural Ordering and Electrical Characteristics of Polythiophene Thin Films. *RSC Adv.* **2014**, *4* (77), 41159–41163.

(39) Tomasko, D. L.; Li, H. B.; Liu, D. H.; Han, X. M.; Wingert, M. J.; Lee, L. J.; Koelling, K. W. A Review of CO2 Applications in the Processing of Polymers. *Ind. Eng. Chem. Res.* **2003**, *42* (25), 6431–6456.

(40) Kazarian, S. G. Polymer Processing with Supercritical Fluids. *Polym. Sci.* **1999**, *28* (2), 179–220.

(41) Amonoo, J. A.; Glynos, E.; Chen, X. C.; Green, P. F. An Alternative Processing Strategy for Organic Photovoltaic Devices Using a Supercritical Fluid. *J. Phys. Chem. C* **2012**, *116* (39), 20708–20716.

(42) Kokubu, R.; Yang, Y. Vertical Phase Separation of Conjugated Polymer and Fullerene Bulk Heterojunction Films Induced by High Pressure Carbon Dioxide Treatment at Ambient Temperature. *Phys. Chem. Chem. Phys.* **2012**, *14* (23), 8313–8318.

(43) Spano, F. C. Modeling Disorder in Polymer Aggregates: The Optical Spectroscopy of Regioregular poly(3-Hexylthiophene) Thin Films. *J. Chem. Phys.* **2005**, *122* (23), 234701.

(44) Hozumi, A.; Ushiyama, K.; Sugimura, H.; Takai, O. Fluoroalkylsilane Monolayers Formed by Chemical Vapor Surface Modification on Hydroxylated Oxide Surfaces. *Langmuir* **1999**, *15* (22), 7600–7604.

(45) Sugimura, H.; Ushiyama, K.; Hozumi, A.; Takai, O. Micropatterning of Alkyl- and Fluoroalkylsilane Self-Assembled Monolayers Using Vacuum Ultraviolet Light. *Langmuir* **2000**, *16* (3), 885–888.

(46) Tammer, M.; Monkman, A. P. Measurement of the Anisotropic Refractive Indices of Spin Cast Thin poly(2-Methoxy-5-(2'-ethyl-Hexyloxy)-P-Phenyl-Enevinylene) (MEH-PPV) Films. *Adv. Mater.* **2002**, *14* (3), 210–212.

(47) Gurau, M. C.; Delongchamp, D. M.; Vogel, B. M.; Lin, E. K.; Fischer, D. a; Sambasivan, S.; Richter, L. J. Measuring Molecular Order in poly(3-Alkylthiophene) Thin Films with Polarizing Spectroscopies. *Langmuir* **2007**, *23* (2), 834–842.

(48) Wang, H.; Gomez, E. D.; Kim, J.; Guan, Z.; Jaye, C.; Fischer, D. A.; Kahn, A.; Loo, Y. L. Device Characteristics of Bulk-Heterojunction Polymer Solar Cells Are Independent of Interfacial Segregation of Active Layers. *Chem. Mater.* **2011**, *23* (8), 2020–2023.

(49) Kim, J. B.; Guan, Z.-L.; Lee, S.; Pavlopoulou, E.; Toney, M. F.; Kahn, A.; Loo, Y.-L. Modular Construction of P3HT/PCBM Planar-Heterojunction Solar Cells by Lamination Allows Elucidation of Processing–structure–function Relationships. *Org. Electron.* **2011**, *12* (11), 1963–1972.

(50) Possanner, S. K.; Zojer, K.; Pacher, P.; Zojer, E.; Schürrer, F. Threshold Voltage Shifts in Organic Thin-Film Transistors Due to Self-Assembled Monolayers at the Dielectric Surface. *Adv. Funct. Mater.* **2009**, *19* (6), 958–967.

(51) Pernstich, K. P.; Haas, S.; Oberhoff, D.; Goldmann, C.; Gundlach, D. J.; Batlogg, B.; Rashid, a. N.; Schitter, G. Threshold Voltage Shift in Organic Field Effect Transistors by Dipole Monolayers on the Gate Insulator. *J. Appl. Phys.* **2004**, *96* (11), 6431–6438.

(52) Gholamrezaie, F.; Andringa, A. M.; Roelofs, W. S. C.; Neuhold, A.; Kemerink, M.; Blom, P. W. M.; De Leeuw, D. M. Charge Trapping by Self-Assembled Monolayers as the Origin of the Threshold Voltage Shift in Organic Field-Effect Transistors. *Small* **2012**, *8* (2), 241–245.

(53) McBranch, D.; Campbell, I. H.; Smith, D. L.; Ferraris, J. P. Optical Determination of

Chain Orientation in Electroluminescent Polymer Films. *Appl. Phys. Lett.* **1995**, *66* (10), 1175–1177.

(54) Spano, F. C. Absorption in Regio-Regular poly(3-Hexyl)thiophene Thin Films: Fermi Resonances, Interband Coupling and Disorder. *Chem. Phys.* **2006**, *325* (1), 22–35.

(55) Sirard, S. M.; Gupta, R. R.; Russell, T. P.; Watkins, J. J.; Green, P. F.; Johnston, K. P. Structure of End-Grafted Polymer Brushes in Liquid and Supercritical Carbon Dioxide: A Neutron Reflectivity Study. *Macromolecules* **2003**, *36* (9), 3365–3373.

(56) Shah, V. M.; Hardy, B. J.; Stern, S. a. Solubility of Carbon Dioxide, Methane, and Propane in Silicone Polymers. Effect of Polymer Backbone Chains. *J. Polym. Sci. Part B Polym. Phys.* **1993**, *31* (3), 313–317.

(57) Tuminello, W. H.; Dee, G. T.; McHugh, M. a. Dissolving Perfluoropolymers in Supercritical Carbon Dioxide. *Macromolecules* **1995**, *28* (5), 1506–1510.

(58) Canelas, D. a.; Betts, D. E.; DeSimone, J. M. Dispersion Polymerization of Styrene in Supercritical Carbon Dioxide: Importance of Effective Surfactants. *Macromolecules* **1996**, *29* (8), 2818–2821.

(59) Guan, Z.; DeSimone, J. M. Fluorocarbon-Based Heterophase Polymeric Materials. 1. Block Copolymer Surfactants for Carbon Dioxide Applications. *Macromolecules* **1994**, *27* (20), 5527–5532.

(60) Katano, Y.; Tomono, H.; Nakajima, T. Surface Property of Polymer Films with Fluoroalkyl Side Chains. *Macromolecules* **1994**, *27* (8), 2342–2344.

(61) Ma, J.; Hashimoto, K.; Koganezawa, T.; Tajima, K. End-on Orientation of Semiconducting Polymers in Thin Films Induced by Surface Segregation of Fluoroalkyl Chains. *J. Am. Chem. Soc.* **2013**, *135* (26), 9644–9647.

(62) Wang, J.; Mao, G.; Ober, C. K.; Kramer, E. J. Liquid Crystalline, Semifluorinated Side Group Block Copolymers with Stable Low Energy Surfaces: Synthesis, Liquid Crystalline Structure, and Critical Surface Tension. *Macromolecules* **1997**, *30* (96), 1906–1914.

(63) Himmelberger, S.; Salleo, A. Engineering Semiconducting Polymers for Efficient Charge Transport. *MRS Commun.* **2015**, *5* (3), 383–395.

(64) Mollinger, S. a.; Krajina, B. a.; Noriega, R.; Salleo, A.; Spakowitz, A. J. Percolation, Tie-Molecules, and the Microstructural Determinants of Charge Transport in Semicrystalline Conjugated Polymers. *ACS Macro Lett.* **2015**, *4* (7), 708–712.

Chapter 4 : MOLECULAR ORGANIZATION IN MAPLE-DEPOSITED CONJUGATED POLYMER THIN FILMS AND THE IMPLICATIONS FOR CARRIER TRANSPORT CHARACTERISTICS

Reprinted with permission from:

Dong, B. X.; Li, A.; Strzalka, J.; Stein, G. E.; Green, P. F. Molecular Organization in MAPLE-Deposited Conjugated Polymer Thin Films and the Implications for Carrier Transport Characteristics. *J. Polym. Sci. Part B Polym. Phys.* 2017, 55 (1), 39–48.

4.1. INTRODUCTION

With their important applications including thin film transistors,[1] lighting, displays[2,3] and organic solar cells,[4,5] the molecular design, synthesis and processing of conjugated polymers is of significant scientific and technological interest. Charge carrier mobilities, and hence device performance, are strongly influenced by the morphology of conjugated polymers.[6–8] Therefore, understanding the interrelations between chemistry, processing, morphology, and thus optoelectronic performance is crucial for designing high performance polymeric semiconductor materials.

Thin conjugated polymer films can be prepared by solution or vacuum-based deposition techniques. Whereas solution-based methods offer advantages of low-cost and high-throughput manufacturing, the fabrication of complex systems such as layered, nano-patterned structures, or in cases of underlying surfaces having poor wettability poses significant challenges. Recently, the vacuum-based deposition technique matrix-assisted pulsed laser evaporation (MAPLE) has been increasingly employed for fabrication of thin polymer films by different research groups.[9–

[12] The film deposition process in MAPLE involves the absorption of light with a specific wavelength from a laser by a frozen dilute polymer/solvent mixture. Ideally, the sacrificial host solvent is chosen such that it absorbs the majority of the laser energy, thereby minimizing or altogether avoiding the photochemical degradation of the guest polymer. Together with its advantages of being a vacuum-based deposition technique, the MAPLE technique enables the production of films with unique morphologies and associated physical properties.[13,14] With its unprecedented capabilities, MAPLE has readily been exploited for growing thin polymer films for a wide range of applications including sensors,[15,16] drug delivery and medical implants.[17] Recently, promising findings have also been reported for the use of MAPLE in depositing conjugated polymers for solar cells, organic light emitting diodes and other organic electronic applications.[18–26] Although operational devices have been made, the detailed molecular structure and the fundamental connection between processing, morphology and transport in those devices are still poorly understood.

In our prior work, we investigated the carrier transport properties of MAPLE-deposited poly(3-hexylthiophene) (P3HT) films in connection with the unique morphology in an effort to understand carrier transport characteristics of devices fabricated by the MAPLE technique. UV-vis absorption spectroscopy indicated that MAPLE-deposited samples possessed higher degrees of morphological disorder, compared to their spin-cast analogs. Notably, MAPLE-deposited P3HT films exhibited comparable in-plane mobilities but significantly lower out-of-plane mobilities than those of spin-cast analogs, due to the unequal influences of disorder on in- and out-of-plane transport.[18] However, in order to further understand the structure-function relationship in MAPLE-deposited conjugated polymer films, a detailed study on molecular structure has yet to be done.

Using grazing-incidence wide angle X-ray scattering (GIWAXS), we investigate the structure of MAPLE-deposited P3HT films on various types substrates and compare the results to films produced using conventional spin-casting. Three common substrates for organic electronic devices were used: SiO_2/Si, octyltrichlorosilane (OTS)-treated SiO_2/Si, and poly(3,4-ethylenedioxythiophene) polystyrene sulfonate (PEDOT)/indium tin oxide (ITO)/glass. The GIWAXS studies, complemented by variable angle spectroscopic ellipsometry (VASE) measurements, reveal that MAPLE-deposited samples possess a higher degree of disorder, with more random orientations of polymer crystallites along side-chain stacking, π-π stacking and conjugated backbone directions. Unlike solvent-cast films, the morphologies of the MAPLE-deposited films are independent of the substrate onto which they are deposited. These studies provide important new insights into the mechanism of film formation of MAPLE-deposited semicrystalline conjugated polymer films in connection to in-plane charge carrier transport properties.

4.2. EXPERIMENTAL

4.2.1. Sample Preparation

All substrates used in this study were cleaned by ultrasonication in an Alconox® detergent solution, DI water, acetone, hot Hellmanex® solution and 2-propanol for 5 min each, followed by UV-ozone treatment for 20 min. Thin film transistor (TFT) measurements were performed on polymer films deposited on highly doped Si with 300 nm of thermally-grown SiO_2. GIWAXS measurements were performed on polymer films deposited on 3 different substrates: Si with 300 nm of thermally grown SiO_2 (SiO_2/Si), octyltrichlorosilane (OTS)-treated SiO_2/Si and indium tin oxide (ITO)/glass coated with a layer of poly(3,4-ethylenedioxythiophene) polystyrene sulfonate (PEDOT). The self-assembled monolayer of OTS (Sigma-Aldrich) was

grown on top of the Si/SiO_2 substrate by immersing the substrate in a mixture of OTS and hexadecane (1:250 by volume) for 14 hours while stirring. A smooth OTS layer was formed on top of the Si/SiO_2 substrate as confirmed by Atomic Force Microscopy (data not shown). PEDOT/ITO/glass substrates were fabricated by spin-casting filtered PEDOT solution (Clevios PH 500) onto the cleaned ITO/glass substrates and annealed at 130 °C for 20 min before polymer deposition. The ellipsometric measurements were performed on films supported by Si substrates possessing different thermal oxide layer thicknesses.

Solutions of P3HT (Rieke Metal, ~95% regioregularity, M_w = 50 000 $g \cdot mol^{-1}$) were prepared by dissolving the polymer in 1,2-dichlorobenzene with concentration 10 mg/ml and shaken overnight before filtering with a 0.45 μm filter. The filtered solutions were then spun onto the prepared substrates at 600 rpm for 2 min to make spin-cast films. For OTS-treated substrates, the P3HT solutions were left to stand on the substrates for several minutes before spin-casting due to the poor wettability of OTS.

Our MAPLE deposition system was purchased from PVD Products, equipped with an Er:YAG laser (Quantel) that produces a wavelength of 2.94 μm. We exploited an emulsion-based approach pioneered by the Stiff-Roberts's group.[21] In this strategy, the polymer is first dissolved in 1,2-dichlorobenzene (5 mg/ml), then mixed with benzyl alcohol and deionized (DI) water (containing 0.005 wt.% sodium dodecyl sulfate surfactant) at a 1:0.3:3 ratio, and then shaken and ultrasonicated to generate a homogeneous emulsion. The emulsion was injected into a pre-cooled target cup (ca.−170 °C); once it was fully frozen, the chamber was pumped in a high vacuum to a pressure < 2×10^{-5} Torr. To maintain relatively uniform/consistent ablation over the course of deposition, the target was subjected to a constant rotation, while the laser (fluence ~1.3 J/cm^2 at a repetition rate of 5 Hz) was rastered across the surface. The substrates

were suspended in face-down at a height of 5.5 cm above the target, and were also kept at a constant rotation to achieve uniform deposition. The deposition time was approximately 5 hours. Film thicknesses of all spin-cast and MAPLE samples in this study were kept at ca. 80 nm, as confirmed by both AFM and spectroscopic ellipsometry.

4.2.2. In-plane mobility measurements

Top-contact, bottom-gate transistor configurations were used to fabricate transistors for in-plane mobility measurements. Thin film transistors were made by depositing polymer on top of OTS-treated substrates. After deposition of polymer films, source and drain gold electrodes (Kurt J. Lesker, 99.99%) were vacuum-deposited on top of the polymer film at a rate of 0.5 A/s to fabricate transistors having channel length and width of 50 μm and 500 μm, respectively. In-plane hole mobility (μ) was measured using the Agilent 4156C Parameter Analyzer. The hole mobility was extracted from the drain current I_{DS} by fitting the transfer curve in the saturation regime (V_D = -80 V) using the following equation:

$$I_{DS} = \frac{WC_i}{2L}\mu(V_g - V_t)^2$$

In this equation, W and L are the channel width and length, C_i = 10 nF/cm^2 is the capacitance per unit area of the insulating SiO_2 layer, V_g and V_t are the gate and threshold voltage, respectively. The experiments were conducted in a vacuum cryostat (Janis Inc.) at specific temperatures controlled by a Temperature Monitor (LakeShore Cryotronics).

4.2.3. Grazing incidence wide angle X-ray scattering (GIWAXS)

All samples were measured at beamline 8-ID-E of the Advanced Photon Source (Argonne National Laboratory) with 7.35 keV (λ = 0.16868 nm) synchrotron radiation at an incidence angle of 0.21°, in ambient air.[27] The off-specular scattering was recorded with a Pilatus

1MF pixel array detector (pixel size = 172 μm) positioned 204 mm from the sample. The measurement time was 10 sec per frame, which is short enough to avoid damage to the structure,[28] and data were acquired from 6 positions. Each data set was stored as a 981x1043 32-bit tiff image with 20-bit dynamic range. The Pilatus detector has gaps along the horizontal axis that result in bands of missing data. To fill these gaps, the sample was moved to a fresh spot after each exposure, and measured again with the detector at a new vertical position. The gaps were filled by splicing the data from the two detector positions. This procedure is implemented using the GIXSGUI package for MATLAB.[29] Signal-to-noise was improved by taking the sum of six data sets, which were output as intensity maps in (q_y, q_z)-space also by using the GIXSGUI package. The GIXSGUI package was used to correct the spectra for detection efficiency, the polarization effect and solid-angle variation.

In order to construct partial pole figures, wedge cuts with an angular breadth of 2° were extracted from each GIWAXS data set for detector angles in the range of 90° (vertical cut) up to 180° (horizontal cut). Each wedge cut was fit to an empirical baseline function to subtract the background intensity.[30] The integrated intensity of each peak is reported as a function of the polar angle (χ) between the scattering vector and pole vector.[31] More details of partial pole figure construction can be found in the results and discussion section.

4.2.4. Variable Angle Spectroscopic Ellipsometry (VASE)

VASE measurements were performed using the M-2000 Ellipsometer (J. A. Woollam Co.) on identical polymer films prepared on 4 different Si substrates. One substrate possessed a native layer of SiO_2 and the other 3 possessed a layer of thermally grown SiO_2; the thicknesses of each layer were 300, 500 and 750 nm (Encompass Inc.). VASE measurements were performed in the reflection mode at 5 angles: 55°, 60°, 65°, 70° and 75°. The complex

reflectance ratio of the reflected and incident light polarization states are presented in terms of the ellipsometric angles Ψ and Δ. The thickness and optical constants of P3HT were determined by iteratively fitting Ψ and Δ using the CompleteEASE software, also provided by J. A. Woollam Co. The optical constants of Si, native oxide and thermally grown SiO_2 were taken from CompleteEASE software's library database. The multi-sample analysis and interference enhancement methods were necessary to increase the uniqueness of the fits due to the strong correlations between the fitting parameters. [32] More details of the fitting procedure can be found in the result and discussion section.

4.2.5. Atomic Force Microscopy (AFM)

Topographical images of the top and buried interfaces of P3HT films were probed using an Asylum Research MFP-3D stand-alone AFM in tapping mode with a CT300-25 Aspire probe (spring constant 40 N/m and radius of curvature of 8 nm). The buried interfaces were revealed by delaminating P3HT films from the SAM-treated SiO_2 substrates using a featureless poly(dimethyl siloxane) (PDMS) (Dow Corning Sylgard 184) stamp.

4.3. RESULS AND DISCUSSIONS

This section is divided into two main parts. We begin by describing the structures of MAPLE and spin-cast films, determined by GIWAXS, VASE and AFM. We then discuss the role of structure on electronic transport, and the implications for film forming mechanism.

4.3.1. GIWAXS

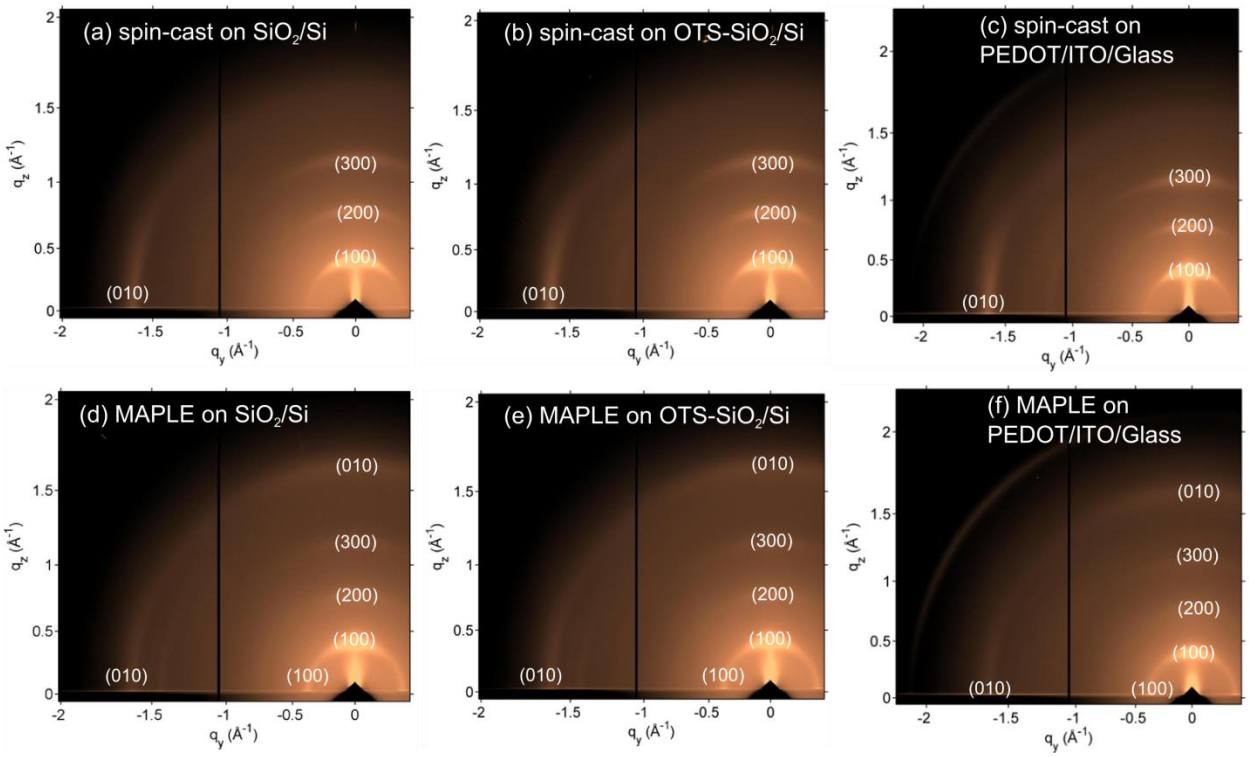

Figure 4.1. Diffraction patterns of (a),(b),(c) spin-cast and (d), (e), (f) MAPLE films deposited on SiO_2/Si, OTS-treated SiO_2/Si and PEDOT/ITO/glass substrates.

GIWAXS experiments provide information about the molecular packing symmetry, lattice parameters, crystallite orientation distributions, and relative degree of crystallinity of MAPLE and spin-cast samples. Shown in Figure 4.1 are GIWAXS patterns of MAPLE and spin-casted films supported by SiO_2/Si, OTS-treated SiO_2/Si and PEDOT/ITO/glass substrates; hereafter the substrates will be denoted as SiO_2, OTS and PEDOT, respectively. The diffraction patterns of films fabricated on different substrates using the same technique are qualitatively similar. As seen in Figure 4.1, for all spin-cast samples the (100) diffraction peak across the side-chain stacking direction is strongest along the out-of-plane (q_z) direction, and the (010) diffraction peak across the π-stacking direction is observed along the in-plane (q_{xy}) direction, indicating a strong bias towards the edge-on crystallite orientation.[33] In contrast, films prepared

by MAPLE exhibit (100) and (010) diffraction peaks along both in-plane and out-of-plane directions, suggesting a more random distribution of polymer crystallite orientations.

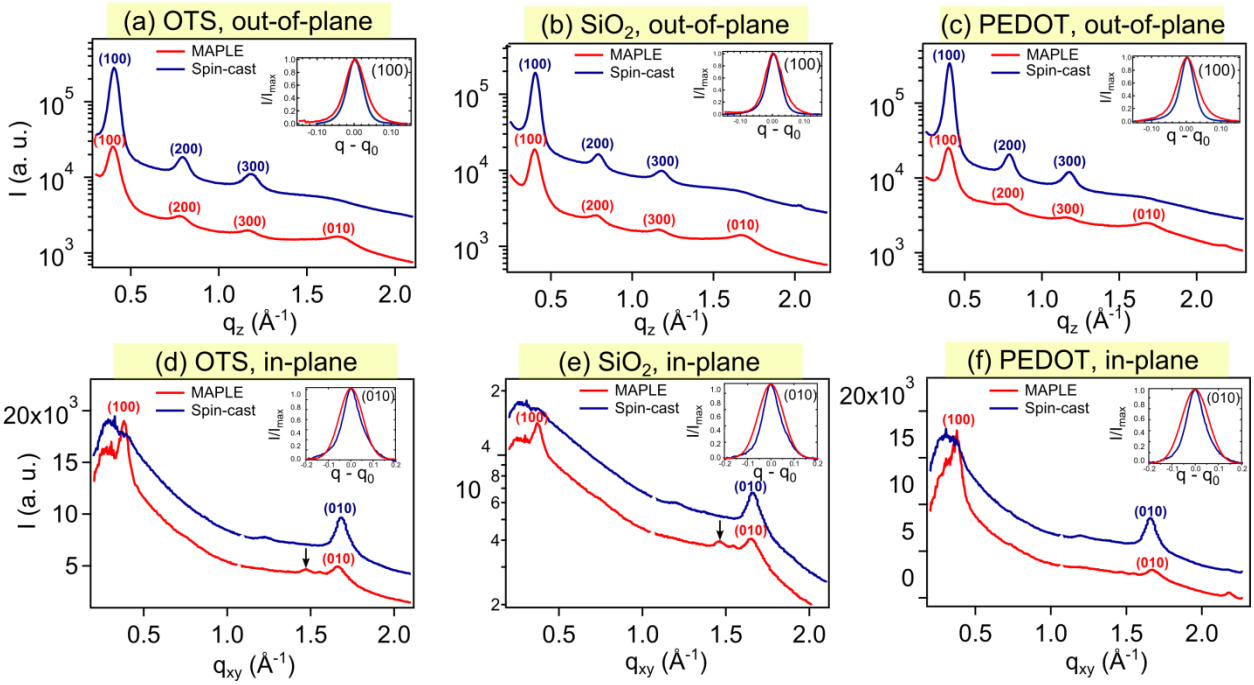

Figure 4.2: (a)(b)(c) Out-of-plane (vertical) and (d)(e)(f) in-plane (horizontal) diffraction signals of MAPLE and spin-cast samples on 3 different substrates. The diffraction intensity of MAPLE and spin-cast samples in each plot are offset vertically for clarity. Insets of (a)(b)(c) and (d)(e)(f) show superimposed line shapes of (100) and (010) diffraction peaks of MAPLE and spin-cast films on the corresponding substrates. Line shapes of (100) peaks were taken from the vertical line cuts, line shapes of (010) peaks were taken from the horizontal line cuts. The (010) diffraction peaks of MAPLE samples were calculated via multi-peak fitting to subtract the diffraction intensities of the adjacent peaks.

Figure 4.2 reports the intensity profiles along the out-of-plane (q_z) and in-plane (q_{xy}) directions. The out-of-plane intensity profiles were extracted from a detector angle of ω = 0º (vertical). The in-plane intensity traces were measured at a detector angle of ω = 83º (nearly horizontal) instead of 90º (horizontal), because at 90º the data are noisier and partially obscured due to standing waves. Similar to visual inspection of the raw data, the intensity traces reveal clear differences in crystallite orientations between MAPLE and spin-cast films. For the spin-cast films, the (100) and (010) peaks are detected along the out-of-plane and in-plane axes,

respectively, which indicates the edge-on crystallite orientations. On the other hand, for the MAPLE-deposited films, the (100) and (010) reflections appear along both directions indicating a more random orientation of crystallites. Furthermore, as shown in the insets of Figure 4.2, the (100) and (010) line shapes appear to be broader for the MAPLE-deposited samples than for the spin-cast samples; this is indicative of a shorter crystal coherence length both in the side-chain and π-stacking directions. We note that the crystal coherence length here is not exactly equal to the crystallite dimension because factors such as paracrystallinity could also contribute to the broadening of the diffraction peaks.[34,35] Identifying the exact origins of the peak broadening requires more sophisticated line-shape analysis[34,36] which is beyond the scope of our study. Nevertheless, we suspect that the broadening of diffraction peaks in MAPLE-deposited samples compared to spin-cast samples at least partially originates from the greater disordered morphology as suggested by AFM and UV-vis absorption spectroscopy measurements, reported earlier from our previous study.[18]

The peak positions (q_{exp}) observed in both MAPLE and spin-cast samples are summarized in Table 4-1. Within experimental error, the peak positions are identical for all MAPLE and spin-cast samples deposited on all substrates. Interestingly, together with the commonly observed (*h*00) and (0*k*0) diffraction peaks, we also observe a weak peak at *ca.* 1.5 $Å^{-1}$ in the q_{xy} direction of MAPLE samples, indicated by the arrows in Figure 4.2(d) and (e). This feature may be a mixed-index peak, which is consistent with a model based on a monoclinic unit cell as described by others.[37,38] The monoclinic unit cell has lattice parameters of a = 16.1 Å, b = 7.6 Å, c = 7.6 Å, corresponding to the lamellar stacking axis, π-stacking axis and backbone direction, respectively. The typical angles for this monoclinic model of P3HT are $\alpha = \beta = 90°$ and $\gamma = 93.5°$. (The angle γ is between a and b axes).[37] Table 1 provides a comparison of the

observed and predicted peak positions. We index the peak at *ca.* 1.5 $Å^{-1}$ in MAPLE samples as a (310) reflection based on this monoclinic cell. It should nevertheless be emphasized that this assignment is very tentative, and more mixed index peaks are needed to verify the model. However, it is important to note that the mixed index peaks are observed exclusively in MAPLE samples in this work and only reported in a few literature studies on P3HT.[37–40] Although there were some examples of mixed index peaks observed in spin-cast P3HT samples,[39,40] they were all fabricated using chloroform, a solvent known to produce highly disordered morphology due to its high volatility.[41] The appearance of mixed index peaks solely in MAPLE-deposited samples thus might suggest higher degree of chain folding and twisting in P3HT films deposited by MAPLE technique compared to those deposited by the spin-cast analog.[42]

Table 4-1: Summarized peaks position observed on MAPLE and spin-cast samples together with predicted peak positions based on the monoclinic unit cell with a = 16.1 Å, b = 7.6 Å, c = 7.6 Å, $\alpha = \beta = 90°$ and $\gamma = 93.5°$.

(hkl)	q_{exp} ($Å^{-1}$), spin-cast	q_{exp} ($Å^{-1}$), MAPLE	q_{pred} ($Å^{-1}$)
(100)	0.39	0.39	0.39
(200)	0.78	0.78	0.78
(300)	1.18	1.18	1.17
(010)	1.67	1.67	1.67
(002)	1.67	1.67	1.66
(310)	Not observed	1.48	1.48

To quantify the molecular orientation distribution and relative degree of crystallinity (DoC) of all samples, partial pole figures of (100) reflections were constructed as a function of the polar angle χ between the scattering vector q_{100} and the substrate normal (Figure 4.3(a)). In GIWAXS measurement, the detector angle ω is not exactly equal to the polar angle χ because the Ewald sphere is curved, as pointed out previously.[31,43,44] The polar angle for the (100) reflection was calculated from each detector angle using the GIXSGUI package.[29] The integrated intensity

at each polar angle was scaled by sin(χ) to correctly quantify the population of crystallites with a particular orientation.[31,44] Shown in Figure 4.3(b) and (c) are the geometrically corrected partial pole figures of (100) reflection of spin-cast and MAPLE-deposited samples on 3 different substrates. The range of polar angles χ accessible with our experimental configuration is 3.2° up to approximately 85° for the (100) reflection. Data at higher angles are impacted by standing waves and thus excluded from the analysis, while data are lower angles cannot be resolved since the reciprocal lattice vector does not intersect with the Ewald sphere in this regime.[31]

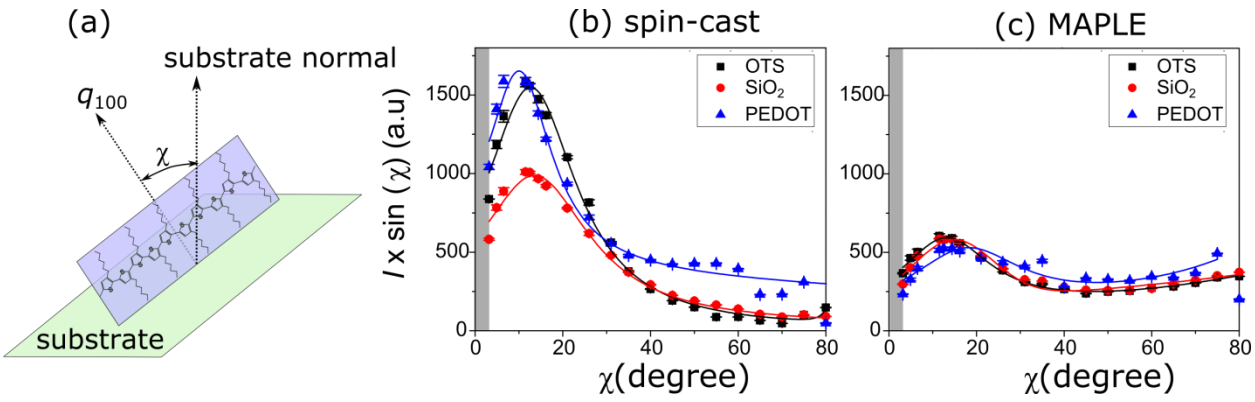

Figure 4.3. (a): Illustration of the polar angle χ, defined as the angle between the substrate normal and the scattering vector along the side-chain direction q_{100}. (b), (c): geometrically corrected pole figures for (100) reflection of spin-cast and MAPLE samples deposited on three different substrates. The gray-shaded areas in figure (b) and (c) denote the non-measurable regime of the experiments. The error bars are calculated from a propagation of errors approach that includes uncertainty in baseline correction and peak integration. The solid lines represent the best fits of the data to an empirical function. The axis scale of (b) and (c) plots are set to the same range for ease of comparison.

For P3HT films deposited by both techniques, pole figures of samples deposited on PEDOT/ITO/glass substrates appear to be noisier than those on SiO_2 and OTS-treated SiO_2 substrates, likely due to the comparative roughness of the PEDOT/ITO surfaces. All spin-cast samples exhibit a large population of crystallites with average orientation near χ = 0º, which is consistent with an edge-on orientation where alkyl side-chains are nearly perpendicular to the

substrate. In stark contrast, MAPLE samples exhibit a broad population of crystallite orientations with a very weak bias towards $\chi = 0^{\circ}$ (edge-on) and $\chi = 90^{\circ}$ (face-on). This outcome agrees with visual inspection of raw detector images in Figure 4.1 and horizontal and vertical line cuts shown in Figure 4.2. Furthermore, while samples spun on OTS and PEDOT exhibit larger edge-on populations than samples spun on SiO_2, as evidenced by higher intensity toward $\chi = 0^{\circ}$, there are no significant differences in the orientation distributions of the (100) reflections across the MAPLE-deposited counterparts. These results suggest that the average structure in spin-cast films is highly sensitive to the substrate chemistry, whereas the average structure in MAPLE deposited films is relatively independent of substrate chemistry.

In order to permit a comparison of the degrees of crystallinity (DoC) of the samples, a series of samples having the same thicknesses $h \sim 80$ nm, confirmed by both ellipsometry and AFM, were prepared. X-ray exposure time and beam footprint size were made the same for all samples in order to further facilitate accurate DoC comparison.[31] The pole figures were fitted using two Lorentzian functions centered near $\chi = 15^{\circ}$ and $\chi = 90^{\circ}$, corresponding to diffraction from edge-on and face-on populations, respectively. Assuming that the data may be smoothly extrapolated to $\chi = 0^{\circ}$ and 90°, integrating the intensity for the whole range of χ demonstrates that relative DoC of spin-cast samples is 1.6:1.3:1 for PEDOT, OTS, and SiO_2, respectively. However, the DoC is identical within experimental uncertainty for MAPLE films deposited on the three substrates. Similar to the distributions of crystallite/aggregate orientations, the DoC also exhibits distinct substrate dependent behaviors, based on the fabrication techniques. This result is consistent with our previously reported findings that the in-plane mobility in MAPLE-deposited transistor devices is not as sensitive to the substrate chemistry as their spin-cast counterparts.[18]

Some limitations of our analysis should be noted. First, GIWAXS measures the average structure throughout the thickness of the film, so it is possible that crystallite orientations and DoC at the buried interface of MAPLE-deposited films may differ from the bulk. Second, because data for $\chi < 3.2^{\circ}$ could not be resolved, crystallites with smaller polar angles are undetectable within our experiment set-up, as indicated by the gray-shaded areas in Figure 4.3(b) and (c). Therefore, some of the very highly edge-on oriented crystallites in spin-cast film on OTS substrate might have not been captured,[45] so it is possible that the DoC of this sample was underestimated. However, such highly oriented crystallites in MAPLE samples are unlikely because of the highly disordered structure in MAPLE samples, evidenced by (i) heterogeneous globular morphology,[18] (ii) broad distribution of conjugation length[18] and (iii) random orientation of polymer chains determined by both GIWAXS and VASE measurement, as will be discussed in the following.

4.3.2. Variable angle spectroscopic ellipsometry measurements

Spectroscopic ellipsometric measurements were performed to determine the average orientation of the conjugated polymer backbones with regard to the underlying substrates. For all MAPLE and spin-cast samples, the best fits were achieved by employing the uniaxial anisotropic model, which assumes different dielectric functions for the in- and out-of-plane direction, but no preferred orientation within the *xy* plane, i.e. $\varepsilon''_{xx} = \varepsilon''_{yy}$ (in-plane)$\neq \varepsilon''_{zz}$ (out-of-plane). No significant differences were observed between the complex permittivities of P3HT films fabricated by the same technique on the three substrates. The representative imaginary parts of complex permittivity ε'' of MAPLE and spin-cast samples on SiO_2 substrate are plotted in Figure 4.4.

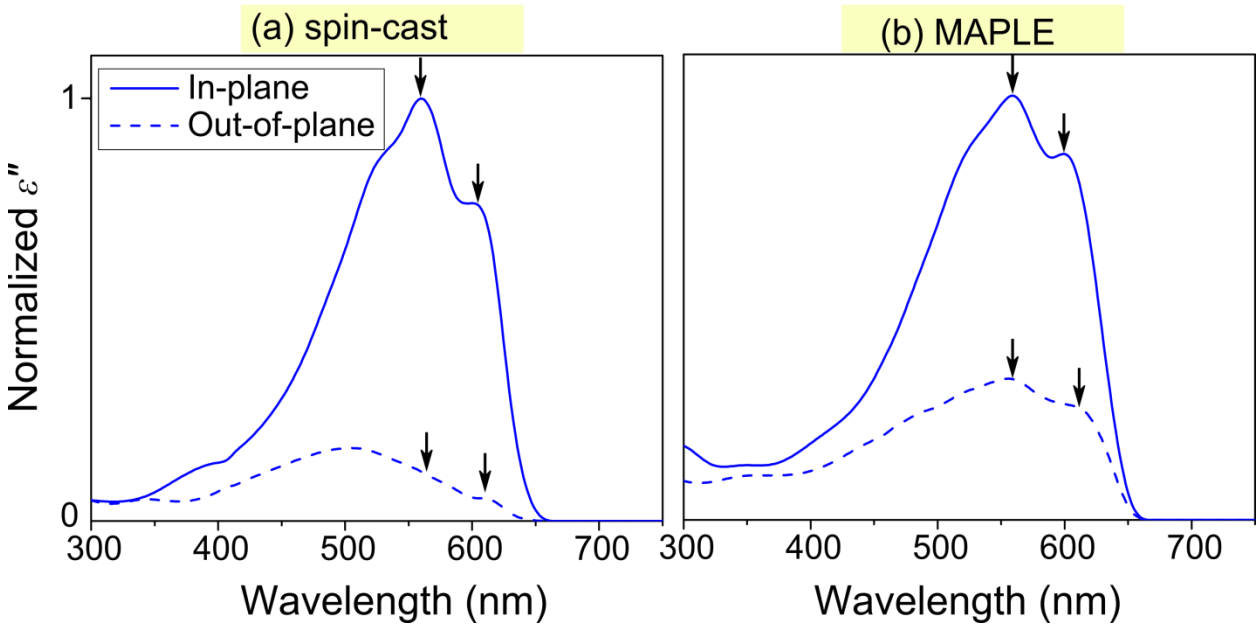

Figure 4.4: In-plane and out-of-plane imaginary permittivities *ε"* of (a) spin-cast and (b) MAPLE films. The arrows indicate the aggregate shoulders in P3HT film.

It is evident that the shape of the in-plane component in MAPLE-deposited film is less defined than that for spin-cast film, indicating a wider distribution of conjugation lengths in MAPLE-deposited sample. This is consistent with our previously reported finding using UV-vis absorption spectroscopy.[18] Both samples exhibit pronounced anisotropic behavior with stronger in-plane than out-of-plane imaginary permittivities. This is indicative of the tendency of the polymer chains to lie parallel to the substrates, which has been widely observed in spin-cast conjugated polymers.[35,46,47] The MAPLE-deposited sample, however, exhibits a relatively stronger out-of-plane component as compared to the spin-cast counterpart, suggesting that the polymer chains in MAPLE samples are oriented more randomly. To quantify the orientation of the polymer chains, we compute the dichroic ratio *R*, defined as the ratio of the out-of-plane to the in-plane imaginary permittivity at *ca.* 610 nm ($R = \varepsilon''_{out\text{-}of\text{-}plane} / \varepsilon''_{in\text{-}plane}$); this position corresponds to the π–π* transition dipole moment in P3HT.[47] The dichroic ratio *R* provides a measure of the average orientation of the polymer backbone, where $R = 1$ corresponds to a

completely isotropic sample and $R = 0$ corresponds to a film in which all the polymer chains lie parallel to the substrate. The observed dichroic ratio of spin-cast P3HT film is 0.12, suggesting a predominantly in-plane orientation of polymer chains in spin-cast films. The dichroic ratio of the MAPLE-deposited film is 0.41, which is significantly higher than that of spin-cast films and comparable to the value reported for spin-cast amorphous films.[47] Interestingly, while the shape of $\varepsilon''_{in\text{-}plane}$ and $\varepsilon''_{out\text{-}of\text{-}plane}$ spectra appears similar for MAPLE sample, those of spin-cast samples differ significantly. In spin-cast samples, the vibronic shoulders that corresponding to aggregate absorption of P3HT[48] (indicated by the dashed arrows in Figure 4.4(a)) are considerably suppressed in the out-of-plane direction, suggesting that the microstructure corresponding to the out-of-plane direction is much more disordered than the one corresponding to the in-plane direction. The resemblance of in- and out-of-plane spectra of MAPLE samples on the other hand indicates that the structure in the in- and out-of-plane directions are similar.[49]

4.3.3. AFM

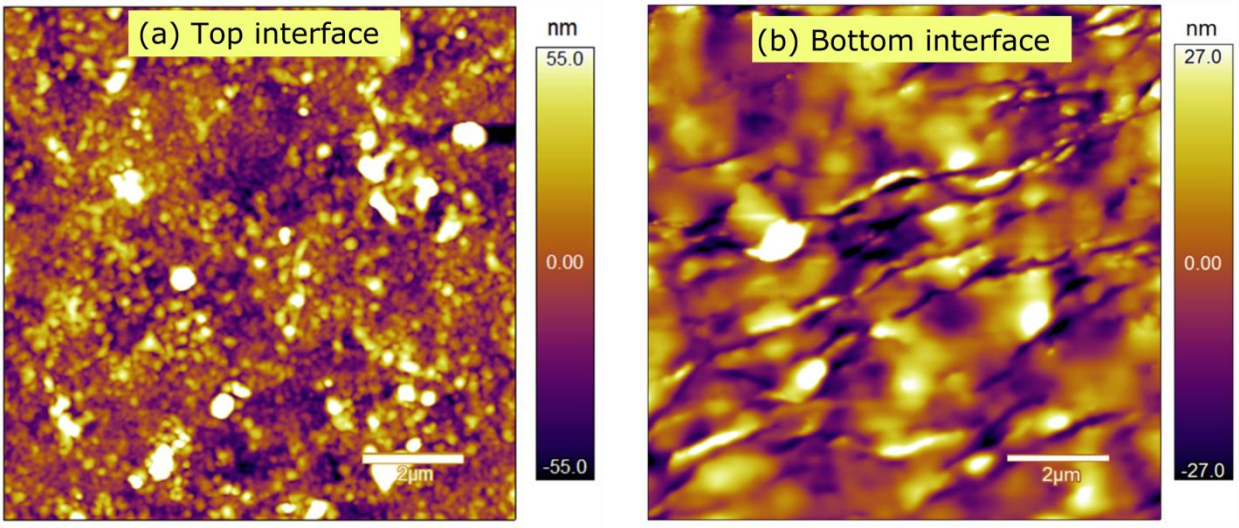

Figure 4.5: 10 x 10 μm AFM images of MAPLE-deposited P3HT's (a) top and (b) bottom (buried) interfaces. The samples were deposited on top of an OTS-treated substrate. The scale bar is 2 μm. The roughness for top and bottom interface is 24 nm and 13 nm, respectively.

Because GIWAXS and VASE measure only the average morphologies across the entire film thickness, AFM measurements were performed to learn about the morphologies at the top and bottom interfaces of MAPLE-deposited samples. Shown in Figure 4.5(a) is the top surface of a MAPLE-deposited P3HT films on an OTS-treated SiO_2 substrate. The surface of the film exhibits a roughness of *ca.* 24 nm, consisting of globular features with diameters ranging from 10 to 200 nm. This type of rough and inhomogeneous globular morphology is consistent with previous reports of MAPLE films, originating from the mechanisms of target ablation causing the polymer and solvent clusters to be ejected towards the substrate.[50] Surprisingly, the AFM scan of the flipped film (substrate interface), shown in Figure 4.5(b), exhibits a very different morphology - no globular structures were observed and the surface is smoother, with a roughness of *ca.* 13 nm. Similar observations were made of MAPLE-deposited films on SiO_2 (data not shown). This is not surprising since the polymer clusters that come in contact with the hard substrate are highly compliant. They may "crash" onto the hard substrates upon arrival and the force of impact resulting in flattened features observed in the AFM images of the flipped films.

4.3.4. Implication of morphology on transport characteristics

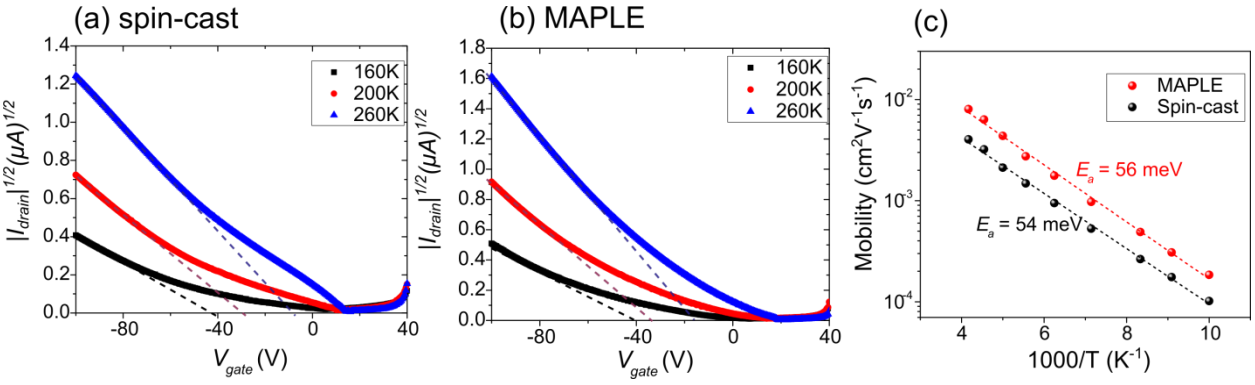

Figure 4.6: (a)(b) Exemplary transistor transfer characteristics of spin-cast and MAPLE samples measured in saturation regime (Vdrain = -80V) at three different temperatures. The dashed lines represent the fit of the linear regime from which the in-plane mobilities are calculated. (c) Arrhenius plot of in-plane mobility of both MAPLE and spin-cast samples. The transport activation energies Ea are shown in the plot.

In order to understand the role of the morphology of the film on carrier transport, we measured the temperature dependence of in-plane carrier mobility by fabricating bottom-gate top-contact thin film transistors (TFTs) on OTS-treated substrates. Figure 4.6(a) and (b) depicts the transistor transfer characteristics in the saturation regime (V_{drain} = -80V) at three different temperatures of spin-cast and MAPLE samples, respectively. It can be immediately seen that for both samples, the drain current rises with increasing temperature, suggesting higher carrier mobilities at higher temperature. This is indicative of thermally activated charge transport characteristics typically observed in organic semiconductors. Despite the seemingly unfavorable molecular orientation (less in-plane orientation of the backbone and π-π stacking) and the highly disordered morphology, the MAPLE-deposited sample exhibits very similar field-effect transport properties to the spin-cast sample with comparable or even superior in-plane carrier mobilities at all temperatures within the range tested. The activation energies E_a calculated from the Arrhenius equation are 56 and 54 meV for MAPLE and spin-cast samples, respectively. These numbers are close to the transport activation energies of many high performing polymers used in TFT in literature such as pBTTT, high molecular weight P3HT, as well as many other high mobility donor-acceptor copolymers.[35,51,52] This implies that TFT transport in both MAPLE-deposited sample and spin-cast sample, despite their morphological dissimilarity, might be limited by the same process that governs the activation energies.

The reasons for the comparable mobilities may be better understood from the following. First, GIWAXS and VASE measurements are only sensitive to the morphology of the bulk and therefore do not reflect the morphology near the buried interface where carrier transport in TFT transistors is known to occur.[53] It could be that in MAPLE samples, the molecular order near the substrate is more favorable for in-plane transport than the bulk. We showed evidence that the

topography of the polymer layer within the close vicinity of the dielectric interface is significantly different from the top. This layer may consist of aggregates with the conjugated backbone oriented parallel to the substrate or aggregates with strong edge-on orientations. An alternative explanation is that the absence of significant long-range order or highly oriented aggregates might not necessarily be detrimental for carrier transport, which has been increasingly observed in many recently engineered high mobility polymers[35,54,55] In other words, the transport may be somewhat resilient to the structure. Due to the lack of long-range order, macroscopic charge migration in conjugated polymer films relies on the combination of fast transport of carriers along polymer backbone (intrachain transport) and relatively slower hopping transport across π-stacking direction (interchain transport). It was recently proposed that efficient long-range charge transport across conjugated polymer films only requires short-range intermolecular aggregation of a few polymer chains.[56,57] As discussed in our previous publication, despite the very different morphologies, the UV-vis absorption spectrum and the extracted conjugation lengths of MAPLE-deposited film are very similar to those of spin-cast films.[18] This suggests that at a very local scale, the chain aggregation behavior in MAPLE samples is similar to spin-cast samples. Here, such local aggregation is demonstrably sufficient for facile carrier transport in highly disordered MAPLE samples.

4.3.5. Implication of morphology on film forming mechanism

Unlike spin-cast samples, the average molecular orientation and DoC of MAPLE-deposited P3HT samples appear independent of the substrate chemistry, suggesting that different mechanisms drive the film formation compared to solvent-casting techniques. Both experiments and simulations suggest that film growth in MAPLE involves 3 different steps: (i) ejection of plumes of solvent-polymer droplets due to explosive decomposition of the solvent molecules

after absorbing the energy from the laser pulses, (ii) rapid removal of solvent molecules from the solvent-polymer droplets during transport from target to substrate and (iii) deposition of the remaining polymer globules onto the substrate.[50,58,59] Therefore, the formation of P3HT aggregates may occur during two distinct stages in the deposition process. In one case, they may form prior to arrival at the substrate, either in the frozen target or during the transfer from target to substrate. In another case, the aggregates may form subsequent to deposition of P3HT globules atop the substrate. To date, the exact origin and mechanism of aggregates formation in MAPLE-deposited conjugated polymer films remains elusive.

Based on our results, we hypothesize that most of the aggregates form prior to deposition at the substrate. This hypothesis is supported by several key observations. First, the DoC and orientation of the MAPLE films are independent of the substrate chemistry, suggesting that there is little or no nucleation, aggregation, or crystallization after the globules arrive at the substrate. Second, the random orientation of polymer aggregates in the films suggests there is little interaction with the substrate during aggregate formation. This assumption is further corroborated by the line shape of $\varepsilon''_{in\text{-}plane}$ and $\varepsilon''_{out\text{-}of\text{-}plane}$ obtained from VASE measurement (Figure 4.4). For spin-cast samples, the aggregate shoulders in $\varepsilon''_{out\text{-}of\text{-}plane}$ are considerably weaker than those in $\varepsilon''_{in\text{-}plane}$, revealing significant chain disorder in the out-of-plane directions. This reflects the preferred growth in the in-plane direction of the conjugated backbone in the aggregates. On the other hand, the similar line shape of $\varepsilon''_{in\text{-}plane}$ and $\varepsilon''_{out\text{-}of\text{-}plane}$ in MAPLE-deposited samples indicates no preference in the growth direction of the aggregates, providing further evidence that aggregate formation is not impacted by interactions with the substrate.

Finally, we would like to point out that since MAPLE films are formed from merging of discrete globular units overlapping one another, it is possible that only the near-substrate layer

would exhibit substrate-sensitive morphological differences. Thus, we expect to see a stronger substrate dependence behavior upon decreasing the film thickness towards the globule size, because self-assembled monolayers (SAMs) such as OTS are known to have localized effect on polymer structure.[45] A thorough examination on film forming mechanism therefore should motivate a thickness dependence study of polymer structure on different substrates and will be the subject of our investigations in the near future.

4.4. CONCLUSION

In this work, we compared molecular structure of MAPLE-deposited P3HT films and spin-casted P3HT films on 3 different substrates: OTS, SiO_2 and PEDOT. GIWAXS data showed higher degrees of disorder and a more random orientation of polymer crystallites in all MAPLE-deposited samples compared to spin-cast counterparts. Additionally, VASE measurements revealed little overall preferential orientation of the conjugated polymer backbone in MAPLE films, further highlighting the highly disordered structure in films deposited by the MAPLE technique. Partial pole figures from GIWAXS measurements indicated a negligible dependence of average polymer morphology on substrate chemistry of MAPLE-deposited films compared to the spin-cast analogs. MAPLE-deposited samples exhibited identical average structures on all substrates, whereas spin-cast samples prepared on PEDOT and OTS showed higher degrees of crystallization and more edge-on orientations of polymer crystallites than the sample prepared on SiO_2. The implications of the morphology on charge transport were illustrated with temperature dependent studies of field-effect mobilities, yielding results suggesting that structural disorder or unfavorable molecular orientations revealed by GIWAXS and VASE may not be the limiting factors for in-plane carrier transport. These results also supported our proposed mechanism of the film formation in MAPLE films, specifically, that the

aggregates nucleate and form prior to reaching the substrate. Future efforts involving manipulation of molecular order in MAPLE films will focus on factors such as controlling the degree of π-stacked aggregates in the emulsion rather than changing the chemistry of the underlying substrates.

4.5. REFERENCES

(1) Sirringhaus, H. 25Th Anniversary Article: Organic Field-Effect Transistors: The Path Beyond Amorphous Silicon. *Adv. Mater.* **2014**, *26* (9), 1319–1335.

(2) Geffroy, B.; le Roy, P.; Prat, C. Organic Light-Emitting Diode (OLED) Technology: Materials, Devices and Display Technologies. *Polym. Int.* **2006**, *55* (6), 572–582.

(3) Müllen, K.; Scherf, U. *Organic Light Emitting Devices: Synthesis, Properties and Applications*; Wiley: New York, 2006.

(4) Günes, S.; Neugebauer, H.; Sariciftci, N. S. Conjugated Polymer-Based Organic Solar Cells. *Chem. Rev.* **2007**, *107* (4), 1324–1338.

(5) Kroon, R.; Lenes, M.; Hummelen, J. C.; Blom, P. W. M.; de Boer, B. Small Bandgap Polymers for Organic Solar Cells (Polymer Material Development in the Last 5 Years). *Polym. Rev.* **2008**, *48* (3), 531–582.

(6) Giebink, N. C.; Forrest, S. R. Quantum Efficiency Roll-off at High Brightness in Fluorescent and Phosphorescent Organic Light Emitting Diodes. *Phys. Rev. B* **2008**, *77* (23), 1–9.

(7) Newman, C. R.; Frisbie, C. D.; Demetrio, A.; Filho, S.; Bre, J. Introduction to Organic Thin Film Transistors and Design of N-Channel Organic Semiconductors. **2004**, 4436–4451.

(8) Pivrikas, A.; Sariciftci, N. S.; Juška, G.; Österbacka, R. A Review of Charge Transport and Recombination in Polymer/Fullerene Organic Solar Cells. *Prog. PHOTOVOLTAICS Res. Appl.* **2007**, *15*, 677–696.

(9) Mcgi, R. A.; Chriseya, D. B.; Piqué, A.; Misnac, T. E.; Washington, D. C. Matrix Assisted Pulsed Laser Evaporation (MAPLE) of Functionalized Polymers : Applications with Chemical Sensors. *Laser Appl. Microelectron. Optoelectron. Manuf. III* **1998**, *3274*, 255–266.

(10) Piqué, a.; McGill, R. a.; Chrisey, D. B.; Leonhardt, D.; Mslna, T. E.; Spargo, B. J.; Callahan, J. H.; Vachet, R. W.; Chung, R.; Bucaro, M. a. Growth of Organic Thin Films by the Matrix Assisted Pulsed Laser Evaporation (MAPLE) Technique. *Thin Solid Films* **1999**, *355*, 536–541.

(11) Chrisey, D. B.; Piqué, A.; McGill, R. A.; Horwitz, J. S.; Ringeisen, B. R.; Bubb, D. M.; Wu, P. K. Laser Deposition of Polymer and Biomaterial Films. *Chem. Rev.* **2003**, *103* (2), 553–576.

(12) Shepard, K. B.; Priestley, R. D. MAPLE Deposition of Macromolecules. *Macromol. Chem. Phys.* **2013**, *214* (8), 862–872.

(13) Guo, Y.; Morozov, A.; Schneider, D.; Chung, J. W.; Zhang, C.; Waldmann, M.; Yao, N.; Fytas, G.; Arnold, C. B.; Priestley, R. D. Ultrastable Nanostructured Polymer Glasses. *Nat. Mater.* **2012**, *11* (4), 337–343.

(14) Shepard, K. B.; Guo, Y.; Arnold, C. B.; Priestley, R. D. Nanostructured Morphology of Polymer Films Prepared by Matrix Assisted Pulsed Laser Evaporation. *Appl. Phys. A Mater. Sci. Process.* **2013**, *110* (4), 771–777.

(15) Sima, F.; Axente, E.; Ristoscu, C.; Mihailescu, I. N.; Kononenko, T. V.; Nagovitsin, I. A.; Chudinova, G.; Konov, V. I.; Socol, M.; Enculescu, I.; Sima, L. E.; Petrescu, S. M. Tailoring Immobilization of Immunoglobulin by Excimer Laser for Biosensor Applications. *J. Biomed. Mater. Res. - Part A* **2011**, *96 A* (2), 384–394.

(16) Casey, C. N.; Campbell, S. E.; Gibson, U. J. Phenylalanine Detection Using Matrix Assisted Pulsed Laser Evaporation of Molecularly Imprinted Amphiphilic Block Copolymer Films. *Biosens. Bioelectron.* **2010**, *26* (2), 703–709.

(17) Cristescu, R.; Popescu, C.; Socol, G.; Visan, A.; Mihailescu, I. N.; Gittard, S. D.; Miller, P. R.; Martin, T. N.; Narayan, R. J.; Andronie, A.; Stamatin, I.; Chrisey, D. B. Deposition of Antibacterial of poly(1,3-Bis-(P-Carboxyphenoxy Propane)-Co-(Sebacic Anhydride)) 20:80/gentamicin Sulfate Composite Coatings by MAPLE. *Appl. Surf. Sci.* **2011**, *257* (12), 5287–5292.

(18) Li, A.; Dong, B. X.; Green, P. Influence of Morphological Disorder on In- and Out-of-Plane Charge Transport in Conjugated Polymer Films. *MRS Commun.* **2015**, *5* (4), 593–598.

(19) Gutiérrez-Llorente, a.; Horowitz, G.; Pérez-Casero, R.; Perrière, J.; Fave, J. L.; Yassar, a.; Sant, C. Growth of Polyalkylthiophene Films by Matrix Assisted Pulsed Laser Evaporation. *Org. Electron. physics, Mater. Appl.* **2004**, *5* (1–3), 29–34.

(20) McCormick, R. D.; Lenhardt, J.; Stiff-Roberts, A. D. Effects of Emulsion-Based Resonant Infrared Matrix Assisted Pulsed Laser Evaporation (RIR-MAPLE) on the Molecular Weight of Polymers. *Polymers (Basel).* **2012**, *4* (4), 341–354.

(21) Pate, R.; Lantz, K. R.; Stiff-Roberts, A. D. Tabletop Resonant Infrared Matrix-Assisted Pulsed Laser Evaporation of Light-Emitting Organic Thin Films. *IEEE J. Sel. Top. Quantum Electron.* **2008**, *14* (4), 1022–1030.

(22) Ge, W.; Li, N. K.; McCormick, R. D.; Lichtenberg, E.; Yingling, Y. G.; Stiff-Roberts, A. D. Emulsion-Based RIR-MAPLE Deposition of Conjugated Polymers: Primary Solvent Effect and Its Implications on Organic Solar Cell Performance. *ACS Appl. Mater.*

Interfaces **2016**, *8* (30), 19494–19506.

(23) Mariano, F.; Caricato, A. P.; Accorsi, G.; Leo, C.; Cesaria, M.; Carallo, S.; Genco, A.; Simeone, D.; Tunno, T.; Martino, M.; Gigli, G.; Mazzeo, M. White Multi-Layered Polymer Light Emitting Diode by Matrix Assisted Pulsed Laser Evaporation. *J. Mater. Chem. C* **2016**.

(24) Ge, W.; McCormick, R. D.; Nyikayaramba, G.; Stiff-Robertsa, A. D. Bulk Heterojunction PCPDTBT:PC71BM Organic Solar Cells Deposited by Emulsion-Based, Resonant Infrared Matrix-Assisted Pulsed Laser Evaporation. *Appl. Phys. Lett.* **2014**, *104* (22).

(25) Caricato, a. P.; Cesaria, M.; Gigli, G.; Loiudice, a.; Luches, a.; Martino, M.; Resta, V.; Rizzo, a.; Taurino, a. Poly-(3-hexylthiophene)/[6,6]-Phenyl-C61-Butyric-Acid-Methyl-Ester Bilayer Deposition by Matrix-Assisted Pulsed Laser Evaporation for Organic Photovoltaic Applications. *Appl. Phys. Lett.* **2012**, *100* (7), 73306.

(26) Ge, W.; Atewologun, A.; Stiff-Roberts, A. D. Hybrid Nanocomposite Thin Films Deposited by Emulsion-Based Resonant Infrared Matrix-Assisted Pulsed Laser Evaporation for Photovoltaic Applications. *Org. Electron. physics, Mater. Appl.* **2015**, *22*, 98–107.

(27) Jiang, Z.; Li, X.; Strzalka, J.; Sprung, M.; Sun, T.; Sandy, A. R.; Narayanan, S.; Lee, D. R.; Wang, J. The Dedicated High-Resolution Grazing-Incidence X-Ray Scattering Beamline 8-ID-E at the Advanced Photon Source. *J. Synchrotron Radiat.* **2012**, *19* (4), 627–636.

(28) Vaselabadi, S. A.; Shakarisaz, D.; Ruchhoeft, P.; Strzalka, J.; Stein, G. E. Radiation Damage in Polymer Films from Grazing-Incidence X-Ray Scattering Measurements. *J. Polym. Sci. Part B Polym. Phys.* **2016**, 1–13.

(29) Jiang, Z. GIXSGUI : A MATLAB Toolbox for Grazing-Incidence X-Ray Scattering Data Visualization and Reduction, and Indexing of Buried Three-Dimensional Periodic Nanostructured Films. *J. Appl. Crystallogr.* **2015**, *48* (3), 917–926.

(30) Rivnay, J.; Noriega, R.; Kline, R. J.; Salleo, A.; Toney, M. F. Quantitative Analysis of Lattice Disorder and Crystallite Size in Organic Semiconductor Thin Films. *Phys. Rev. B - Condens. Matter Mater. Phys.* **2011**, *84* (4), 1–20.

(31) Baker, J. L.; Jimison, L. H.; Mannsfeld, S.; Volkman, S.; Yin, S.; Subramanian, V.; Salleo, A.; Alivisatos, A. P.; Toney, M. F. Quantification of Thin Film Crystallographic Orientation Using X-Ray Diffraction with an Area Detector. *Langmuir* **2010**, *26* (11), 9146–9151.

(32) Campoy-Quiles, M.; Alonso, M. I.; Bradley, D. D. C.; Richter, L. J. Advanced Ellipsometric Characterization of Conjugated Polymer Films. *Adv. Funct. Mater.* **2013**, *24*, 2116–2134.

(33) Brinkmann, M.; Wittmann, J.-C. Orientation of Regioregular Poly(3-Hexylthiophene) by Directional Solidification: A Simple Method to Reveal the Semicrystalline Structure of a

Conjugated Polymer. *Adv. Mater.* **2006**, *18* (7), 860–863.

(34) Rivnay, J.; Noriega, R.; Northrup, J. E.; Kline, R. J.; Toney, M. F.; Salleo, A. Structural Origin of Gap States in Semicrystalline Polymers and the Implications for Charge Transport. *Phys. Rev. B - Condens. Matter Mater. Phys.* **2011**, *83* (12), 1–4.

(35) Zhang, X.; Bronstein, H.; Kronemeijer, A. J.; Smith, J.; Kim, Y.; Kline, R. J.; Richter, L. J.; Anthopoulos, T. D.; Sirringhaus, H.; Song, K.; Heeney, M.; Zhang, W.; McCulloch, I.; Delongchamp, D. M. Molecular Origin of High Field-Effect Mobility in an Indacenodithiophene-Benzothiadiazole Copolymer. *Nat. Commun.* **2013**, *4*, 2238.

(36) Prosa, T. J.; Moulton, J.; Heeger, a. J.; Winokur, M. J. Diffraction Line-Shape Analysis of poly(3-Dodecylthiophene): A Study of Layer Disorder through the Liquid Crystalline Polymer Transition. *Macromolecules* **1999**, *32* (12), 4000–4009.

(37) Brinkmann, M.; Rannou, P. Effect of Molecular Weight on the Structure and Morphology of Oriented Thin Films of Regioregular poly(3-Hexylthiophene) Grown by Directional Epitaxial Solidification. *Adv. Funct. Mater.* **2007**, *17* (1), 101–108.

(38) Wu, Z.; Petzold, A.; Henze, T.; Thurn-Albrecht, T.; Lohwasser, R. H.; Sommer, M.; Thelakkat, M. Temperature and Molecular Weight Dependent Hierarchical Equilibrium Structures in Semiconducting poly(3-Hexylthiophene). *Macromolecules* **2010**, *43* (10), 4646–4653.

(39) Joshi, S.; Pingel, P.; Grigorian, S.; Panzner, T.; Pietsch, U.; Neher, D.; Forster, M.; Schere, U. Bimodal Temperature Behavior of Structure and Mobility in High Molecular Weight P3HT Thin Films. *Macromolecules* **2009**, *42* (13), 4651–4660.

(40) Joshi, S.; Joshi, S.; Grigorian, S.; Grigorian, S.; Pietsch, U.; Pietsch, U.; Pingel, P.; Pingel, P.; Zen, A.; Zen, A.; Neher, D.; Neher, D.; Scherf, U.; Scherf, U. Thickness Dependence of the Crystalline Structure and Hole Mobility in Thin Films of Low Molecular Weight Poly(3-Hexylthiophene). *Macromolecules* **2008**, *41* (18), 6800–6808.

(41) Chang, J.-F.; Sun, B.; Breiby, D. W.; Nielsen, M. M.; Sölling, T. I.; Giles, M.; McCulloch, I.; Sirringhaus, H. Enhanced Mobility of Poly(3-Hexylthiophene) Transistors by Spin-Coating from High-Boiling-Point Solvents. *Chem. Mater.* **2004**, *16* (23), 4772–4776.

(42) Brinkmann, M.; Rannou, P. Molecular Weight Dependence of Chain Packing and Semicrystalline Structure in Oriented Films of Regioregular poly(3-Hexylthiophene)revealed by High-Resolution Transmission Electron Microscopy. *Macromolecules* **2009**, *42*, 1125–1130.

(43) Mannsfeld, S. C. B.; Virkar, A.; Reese, C.; Toney, M. F.; Bao, Z. Precise Structure of Pentacene Monolayers on Amorphous Silicon Oxide and Relation to Charge Transport. *Adv. Mater.* **2009**, *21* (22), 2294–2298.

(44) Hammond, M. R.; Kline, R. J.; Herzing, A. a; Richter, L. J.; Germack, D. S.; Ro, H.-W.; Soles, C. L.; Fischer, D. a; Xu, T.; Yu, L.; Toney, M. F.; Delongchamp, D. M. Molecular Order in High-Efficiency Polymer/fullerene Bulk Heterojunction Solar Cells. *ACS Nano*

2011, *5* (10), 8248–8257.

(45) Jimison, L. H.; Himmelberger, S.; Duong, D. T.; Rivnay, J.; Toney, M. F.; Salleo, A. Vertical Confinement and Interface Effects on the Microstructure and Charge Transport of P3HT Thin Films. *J. Polym. Sci. Part B Polym. Phys.* **2013**, *51* (7), 611–620.

(46) Dong, B. X.; Huang, B.; Tan, A.; Green, P. F. Nanoscale Orientation Effects on Carrier Transport in a Low-Band- Gap Polymer. *J. Phys. Chem. C* **2014**, *118* (31), 17490–17498.

(47) Gurau, M. C.; Delongchamp, D. M.; Vogel, B. M.; Lin, E. K.; Fischer, D. a; Sambasivan, S.; Richter, L. J. Measuring Molecular Order in poly(3-Alkylthiophene) Thin Films with Polarizing Spectroscopies. *Langmuir* **2007**, *23* (2), 834–842.

(48) Clark, J.; Silva, C.; Friend, R.; Spano, F. Role of Intermolecular Coupling in the Photophysics of Disordered Organic Semiconductors: Aggregate Emission in Regioregular Polythiophene. *Phys. Rev. Lett.* **2007**, *98* (20), 206406.

(49) DeLongchamp, D. M.; Kline, R. J.; Fischer, D. a; Richter, L. J.; Toney, M. F. Molecular Characterization of Organic Electronic Films. *Adv. Mater.* **2011**, *23* (3), 319–337.

(50) Leveugle, E.; Zhigilei, L. V. Molecular Dynamics Simulation Study of the Ejection and Transport of Polymer Molecules in Matrix-Assisted Pulsed Laser Evaporation. *J. Appl. Phys.* **2007**, *102* (7), 1–19.

(51) Zhang, X.; Hudson, S. D.; Delongchamp, D. M.; Gundlach, D. J.; Heeney, M.; McCulloch, I. In-Plane Liquid Crystalline Texture of High-Performance Thienothiophene Copolymer Thin Films. *Adv. Funct. Mater.* **2010**, *20* (23), 4098–4106.

(52) Kline, R. J.; Mcgehee, M. D.; Kadnikova, E. N.; Liu, J.; Fre, J. M. J.; Toney, M. F. Dependence of Regioregular Poly (3-Hexylthiophene) Film Morphology and Field-Effect Mobility on Molecular Weight. *Macromolecules* **2005**, 3312–3319.

(53) Dinelli, F.; Murgia, M.; Levy, P.; Cavallini, M.; Biscarini, F.; De Leeuw, D. M. Spatially Correlated Charge Transport in Organic Thin Film Transistors. *Phys. Rev. Lett.* **2004**, *92* (11), 116802–1.

(54) Nielsen, C. B.; Turbiez, M.; McCulloch, I. Recent Advances in the Development of Semiconducting DPP-Containing Polymers for Transistor Applications. *Adv. Mater.* **2013**, *25* (13), 1859–1880.

(55) Zhang, W.; Smith, J.; Watkins, S. E.; Gysel, R.; McGehee, M.; Salleo, A.; Kirkpatrick, J.; Ashraf, S.; Anthopoulos, T.; Heeney, M.; McCulloch, I. Indacenodithiophene Semiconducting Polymers for High-Performance, Air-Stable Transistors. *J. Am. Chem. Soc.* **2010**, *132* (33), 11437–11439.

(56) Noriega, R.; Rivnay, J.; Vandewal, K.; Koch, F. P. V; Stingelin, N.; Smith, P.; Toney, M. F.; Salleo, A. A General Relationship between Disorder, Aggregation and Charge Transport in Conjugated Polymers. *Nat. Mater.* **2013**, *12* (11), 1038–1044.

(57) Himmelberger, S.; Salleo, A. Engineering Semiconducting Polymers for Efficient Charge

Transport. *MRS Commun.* **2015**, *5* (3), 383–395.

(58) Shepard, K. B.; Arnold, C. B.; Priestley, R. D. Origins of Nanostructure in Amorphous Polymer Coatings via Matrix Assisted Pulsed Laser Evaporation. *Appl. Phys. Lett.* **2013**, *103* (12), 123105.

(59) Shepard, K. B.; Arnold, C. B.; Priestley, R. D. Transport and Stability of Laser-Deposited Amorphous Polymer Nanoglobules. *ACS Macro Lett.* **2014**, *3* (10), 1046–1050.

Chapter 5 : CRYSTALLIZATION MECHANISM AND CHARGE CARRIER TRANSPORT IN MAPLE-DEPOSITED CONJUGATED POLYMER THIN FILMS

Adapted from:

Dong, B. X.; Strzalka, J.; Li, H.; Stein, G. E.; Green, P. F. Crystallization Mechanism and Charge Carrier Transport in MAPLE-Deposited Conjugated Polymer Thin Films. *Manuscript under review*

5.1. INTRODUCTION

In chapter 4 we have showed that the structure of MAPLE-deposited conjugated polymer film is highly disordered, yet the devices made from MAPLE-deposited films still exhibit superior in-plane transport characteristics. Moreover, for films with thickness of approximately 80 nm, the degree of crystallinity and molecular orientation in MAPLE-deposited samples are insensitive to the substrate chemistry, which is in stark contrast to the conventional spin-cast technique.[1,2] Our preliminary findings suggest different crystallization mechanism driving film formation in MAPLE compared to solvent-based methods. However, since MAPLE films are formed from merging of discrete globular units overlapping one another, it is possible that only the near substrate layer would exhibit substrate-sensitive morphological differences.

To this end, in this work we investigate the structural evolution of poly(3-hexylthiophene) (P3HT) films during the course of MAPLE-deposition on two different types of substrates: SiO_2/Si and octadecyltrichlorosilane (OTS)-treated SiO_2/Si substrates to further elucidate the crystallization process in MAPLE. Construction of complete X-ray diffraction pole

figures allows one to discern that in MAPLE-deposited samples, there exist two crystallite populations: one of highly-oriented crystals growing directly from the polymer/dielectric interface and one of misoriented crystals growing on top of existing polymer layers. Interestingly, the substrate chemistry exerts distinct effects on the two types of crystallites. We show that compared to misoriented crystals, the growth of highly-oriented crystals depends more significantly on the substrate chemistry. Treating the dielectric substrate with OTS shows to enhance the population as well as the crystallite coherence length of highly-oriented crystal; the effect of OTS treatment on misoriented crystal is weaker. Complementary in-plane mobility measurement highlights the importance of the highly-oriented crystals at the buried interface in dictating transport in organic thin-film transistor.

5.2. EXPERIMENTS

5.2.1. Sample Preparation

All substrates used in this study were cleaned by ultrasonication in an Alconox® detergent solution, DI water, acetone, hot Hellmanex® solution and 2-propanol for 5 min each, followed by UV-ozone treatment for 20 min. Wide angle X-ray scattering (WAXS), thin-film transistor (TFT) and atomic force microscopy (AFM) measurements were performed on polymer films deposited on highly doped Si with 300 nm of thermally-grown SiO_2. UV-vis absorption measurement was performed on polymer films deposited on top of glass substrates. For all measurements, the substrates were used either as non-treated (bare) or treated with a self-assembled monolayer (SAM) of octadecyltrichlorosilane (OTS). OTS was grown on top of the Si/SiO_2 and glass substrates by immersing the substrates in a mixture of OTS and hexadecane (1:250 by volume) for 14 hours while stirring. A smooth OTS layer was formed on top of the Si/SiO_2 substrate as confirmed by AFM and contact angle measurements (data not shown).

Our MAPLE deposition system was purchased from PVD Products, equipped with an Er:YAG laser (Quantel) that produces a wavelength of 2.94 μm. To fabricate polymer films, we exploited the emulsion-based approach.[3] The solution of P3HT (Rieke Metal, ~95% regioregularity, Mw = 50 000 g.mol^{-1}) were first prepared by dissolving the polymer in 1,2-dichlorobenzene (concentration 5 mg/ml) and shaken overnight before filtering with a 0.45 μm filter. In the next step, the P3HT solution was mixed with benzyl alcohol and deionized (DI) water (containing 0.005 wt.% sodium dodecyl sulfate surfactant) at a 1:0.3:3 ratio, and then shaken while ultrasonicated to generate a homogeneous emulsion. The emulsion was injected into a target cup pre-cooled by liquid nitrogen (ca.−170 °C). Once it was fully frozen, the chamber was pumped in a high vacuum to a pressure < 2 × 10^{-5} Torr. To maintain relatively uniform/consistent ablation over the course of deposition, the target was subjected to a constant rotation, while the laser (fluence ~1.3 J/cm^2 at a repetition rate of 5 Hz) was rastered across the frozen surface of the target polymer emulsion. The substrates were suspended in face-down at a height of 5.5 cm above the target, and were also kept at a constant rotation to further achieve uniform deposition. The deposition times were kept from 3 min to 180 min to fabricate films with different thicknesses.

5.2.2. Wide angle X-ray scattering (WAXS)

WAXS measurements were performed at beamline 8-ID-E of the Advanced Photon Source (Argonne National Laboratory) with 10.86 keV (λ = 0.11416 nm) synchrotron radiation.[4] The measurement time was 4 sec per frame, which is short enough to avoid damage to the structure but sufficiently long to ensure high signal-to-noise ratio.[5] Samples were enclosed and measured inside a low vacuum chamber (10^{-3} mbar) to further minimize concerns about radiation damages as well as prevent extraneous scattering from ambient air. For each sample, 4 data sets

were taken from 4 different spots on the sample and then averaged in order to further enhance signal-to-noise ratio. The off-specular scattering was recorded with a Pilatus 1MF pixel array detector (pixel size = 172 μm) positioned 228 mm from the sample. Each data set was stored as a 981x1043 32-bit tiff image with 20-bit dynamic range. The Pilatus detector has rows of inactive pixels at the border between detector modules.. To fill these gaps, after each measurement the detector was moved to a new vertical direction and the measurement on each spot was repeated. The gaps were filled by combining the data from two detector positions. This procedure was implemented using the GIXSGUI package for MATLAB.[6] The signals were output as intensity maps in (q_y, q_z)-space also by using the GIXSGUI package. The GIXSGUI package was used to correct the images for detector nonuniformity, detection efficiency, the polarization effect and solid-angle variation.

In our work, two separate WAXS measurements were performed: one in grazing incidence condition (GIWAXS) and one in local specular condition. In GIWAXS measurement, the samples were tilted at an incidence angle of 0.14° with respect to the beam. This angle is chosen such as it is above the critical angle of the polymer films but below the critical angle of the Si substrates (0.166°) in order to probe the entire thickness of the polymer films. In local specular measurement, the samples were tilted at an incidence angle θ_B = 2.036°, which is the Bragg angle of the scattering vector q_{100} of the (100) reflection in P3HT ($d \approx 1.6$ nm) as determined from the GIWAXS measurement. To construct the pole figure of each sample, wedge cuts with an angular breadth of 0.5° were extracted from both grazing incidence and local specular measurements using GIXSGUI. Each wedge cut was first fit to an empirical baseline function to subtract the background intensity and amorphous scattering. The background-subtracted wedge cut was then fit to a Voigt function in order to extract the integrated intensity

as well as the full width at half maximum (FWHM) of the reflection of interest (100). The integrated intensity of each peak was reported as a function of the polar angle χ between the scattering vector and pole vector. The complete pole figures with the available range of χ from 0° to 90° were constructed by merging data from GIWAXS and local specular measurements.[7,8] More details of the complete pole figure construction can be found in the results and discussion section.

5.2.3. Atomic force microscopy (AFM)

Topographical images of the top interface of P3HT films at different deposition times were probed using an Asylum Research MFP-3D stand-alone AFM in tapping mode with a CT300-25 Aspire probe (spring constant 40 N/m and radius of curvature of 8 nm).

5.2.4. Ultraviolet-visible (UV-vis) absorption spectroscopy

The ultraviolet−visible (UV−vis) absorption spectroscopy measurements were performed using a Lambda 750 UV/vis/ NIR Spectrophotometer (PerkinElmer Inc.). Obtained absorption spectra were then fit to the following Spano equation in order to extract the exciton bandwidth *W* and the disorder parameter σ:[9,10]

$$A_{aggregate} \propto \sum_{m=0} \left(\frac{S^m}{m!}\right) \times \left(1 - \frac{We^{-S}}{2E_p} \sum_{n \neq m} \frac{S^n}{n!(n-m)}\right)^2 \times e^{\frac{(E - E_0 - mE_p - \frac{1}{2}WS^m e^{-S})^2}{2\sigma^2}} \qquad (5\text{-}1)$$

In this equation, *A* is the absorption of the aggregates as a function of photon energy, *E*; *S* is the Huang-Rhys factor, representing the overlap between vibrational states and assumed to be 1; *m* corresponds to different energy levels and E_p = 0.179 eV is the energy of C=C symmetric stretch mode.[9]

5.2.5. In-plane mobility measurements

Bottom-contact, bottom-gate transistor configurations were used to fabricate transistors for in-plane mobility measurements. Thin film transistors were made by first vacuum-depositing source and drain gold electrodes (Kurt J. Lesker, 99.99%) on top of the Si/SiO_2 substrate at a rate of 0.5 A/s. P3HT was then deposited onto the gold-patterned substrates and the transfer curves were collected inside a N_2-filled glovebox in the saturation regime (V_D = −80 V) using the Agilent 4156C Parameter Analyzer. The in-plane hole mobility μ was extracted from the drain current I_{DS} by fitting the transfer curve in the saturation regime using the following equation:

$$I_{DS} = \frac{WC_i}{2L}\mu(V_g - V_t)^2 \quad (5\text{-}2)$$

In this equation, W and L are the channel width and length, C_i = 10 nF/cm^2 is the capacitance per unit area of the insulating SiO_2 layer, V_g and V_t are the gate and threshold voltage, respectively.

5.3. RESULTS AND DISCUSSION

5.3.1. Atomic force microscopy (AFM)

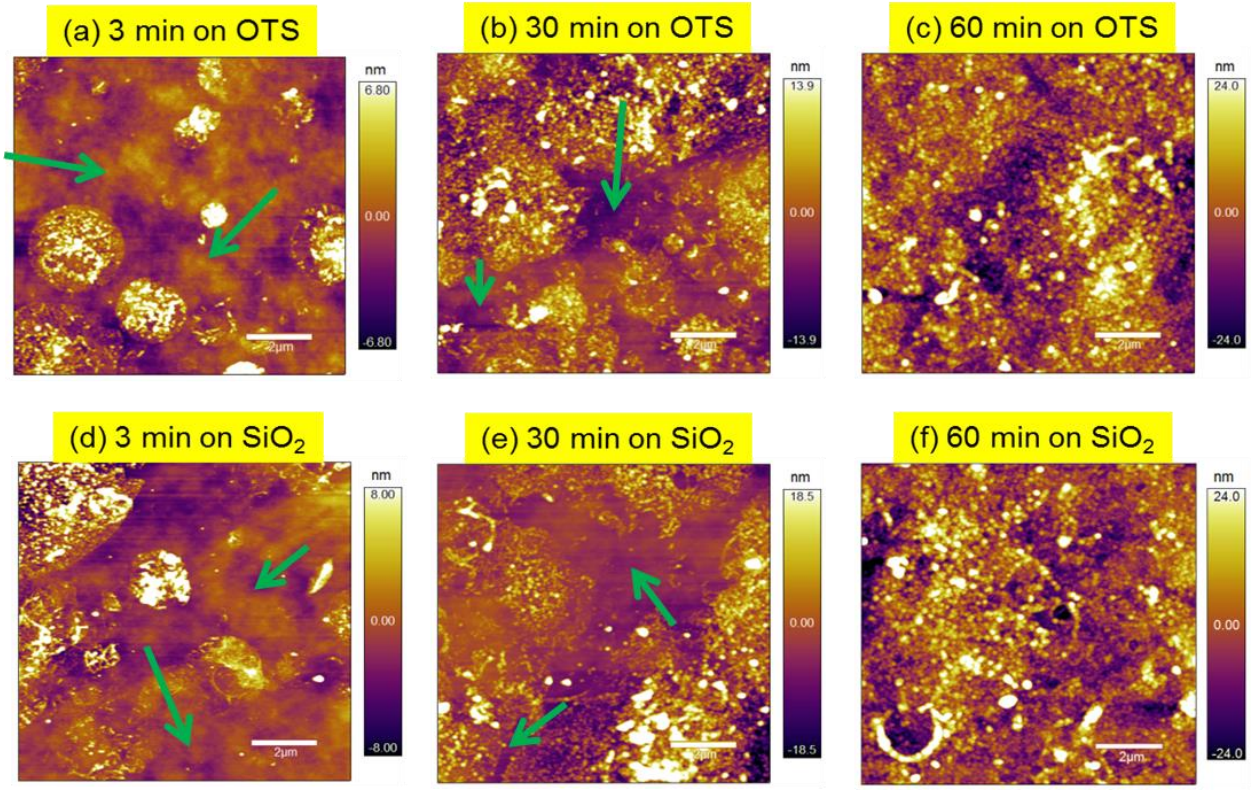

Figure 5.1: 10 x 10 μm AFM images of MAPLE-deposited P3HT on (a), (b), (c) OTS and (d), (e), (f) SiO_2 substrates at different deposition times. The exposed substrate areas of the films are indicated by the green arrows. The scale bar is 2 μm.

AFM measurements were performed to study the surface morphologies of MAPLE-deposited samples as a function of deposition time. Figure 5.1 shows representative topography data for MAPLE-deposited P3HT films at 3 different deposition times on SiO_2/Si and OTS-treated SiO_2/Si substrates; hereafter the substrates will be denoted as SiO_2 and OTS, respectively. At the same deposition time, there are no clear differences in topography for OTS and SiO_2 substrates. The surface of all films consists of globular features with diameters and height ranging from 10 to 200 nm and 5 to 40 nm, respectively. This type of inhomogeneous globular morphology is consistent with previous reports of MAPLE films, originating from the

mechanisms of target ablation causing the polymer and solvent clusters to be ejected towards the substrate.[11] The earliest deposition time of 3 min yields films with small and isolated polymer islands distributed atop the substrates. Interestingly, in contrast to previous report of films deposited using UV-MAPLE,[12] the polymer clusters here are not deposited on the substrate as isolated individual nanoglobules but rather as "patches" of globule islands. With increasing deposition time, the size of the globular islands grows, coalesces and consequently the uncovered area of the substrate reduces. The exposed substrate areas are clearly visible at deposition times of 3 and 30 min, as indicated by the arrows in Figure 5.1(a), (b) and (d), (e). At deposition times beyond 60 min, a continuous polymer film is formed and completely covers the substrates. We note that in MAPLE deposition, the average film thickness h almost linearly scales with deposition time t as $h = 0.37 \pm 0.02$ (nm/min) × t (min) (measured by ellipsometry). At 60 min, the average film thickness is ca. 25 nm (roughness ~15 nm) and at the longest deposition of 180 min, the average film thickness is ca. 70 nm (roughness ~25 nm).

5.3.2. UV-vis absorption spectroscopy

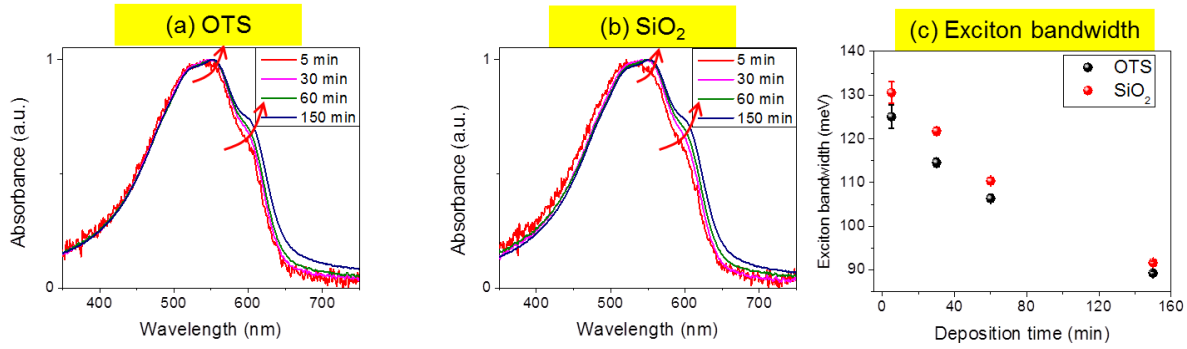

Figure 5.2: UV-vis absorption spectra of MAPLE-deposited P3HT films on (a) OTS-treated glass substrate (OTS) and (b) bare glass substrate (SiO_2). (c) The exciton bandwidth W as a function of deposition times.

UV-vis absorption spectroscopy was performed to investigate the structural evolution of P3HT during the deposition process. The absorption spectra of P3HT on both OTS-treated glass

substrate and bare glass substrates (SiO_2) are plotted in Figure 5.2(a) and (b). It is evident that during the course of MAPLE deposition, the intensity of the vibronic shoulders at ca. 550 nm and 600 nm that correspond to aggregate absorption of P3HT[13] increases for samples on both substrates, indicated by the arrows in Figure 5.2(a) and (b). This is suggestive of the growing fraction of the aggregates within the polymer films upon increasing deposition time. The total absorption can be further deconvoluted into individual peaks by applying the Spano model (equation (1)), from which the exciton bandwidth *W* can be calculated.[9,14] As seen in Figure 5.2(c), upon increasing deposition time *W* shows a steady decrease, with slightly larger values for SiO_2 samples compared to OTS samples. In the limit of weak excitonic coupling between cofacially-packed P3HT chains, the interchain coupling leads to the formation of vibronic bands characterized by the exciton bandwidth *W*. An increase in the conjugation length leads to greater exciton delocalization across polymer chains and hence reduces *W*.[10,15] The reduction of *W* here thus indicates an increase of the average conjugation length upon increasing deposition time, with slightly longer conjugation length in OTS samples compared to SiO_2 samples. This result suggests that P3HT aggregates grow along the backbone direction (001) during the course of deposition.

5.3.3. Wide angle X-ray scattering (WAXS)

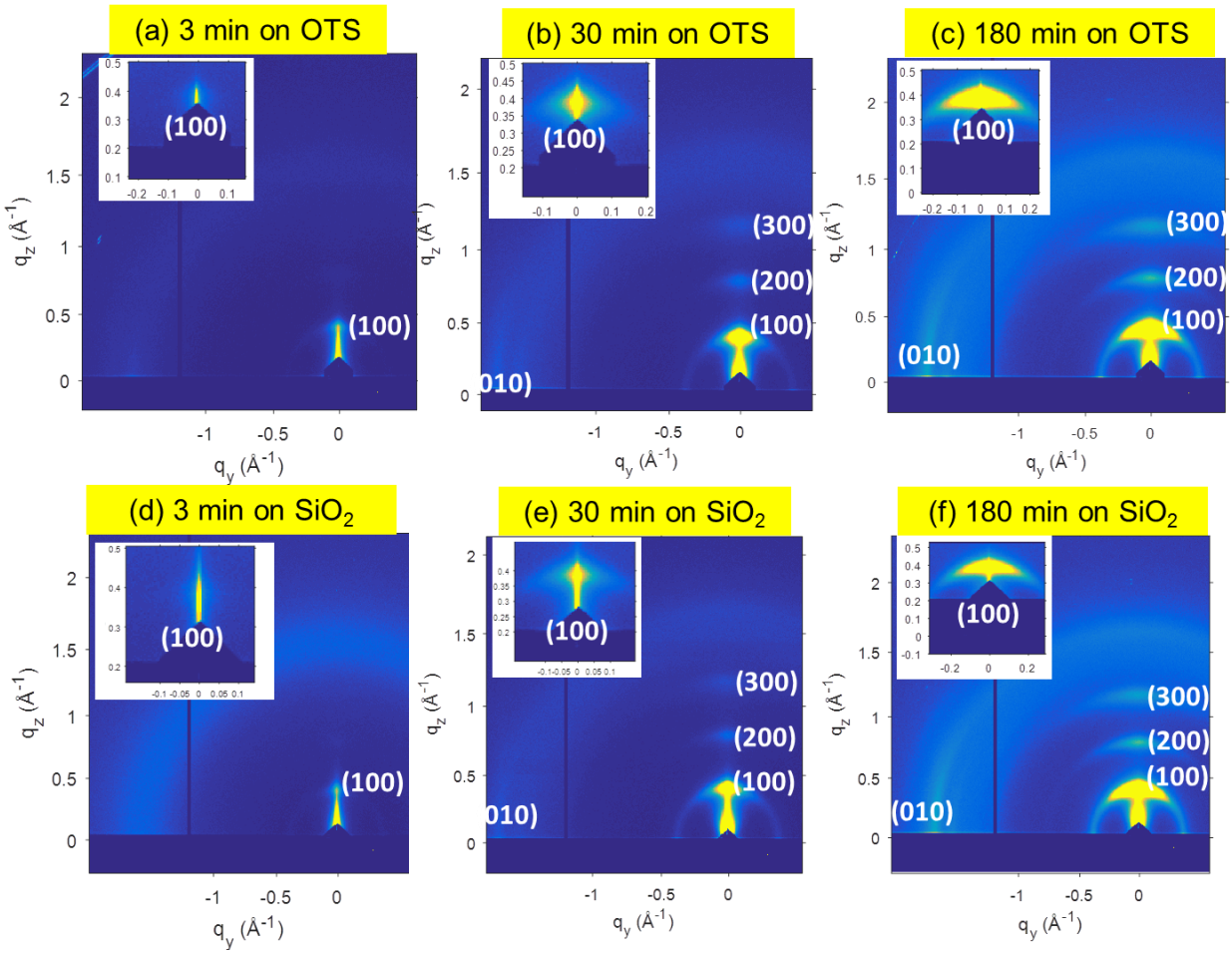

Figure 5.3: Representative GIWAXS detector images of MAPLE samples fabricated at 3 different deposition times on (a)(b)(c) OTS and on (d)(e)(f) SiO_2 substrates. The inset of each figure is local specular detector image of the same sample.

WAXS experiments provide information about the evolution of crystallite orientation distributions, relative degree of crystallinity and crystallite coherence length of MAPLE-deposited samples as a function of deposition time. Shown in Figure 5.3 are representative GIWAXS patterns of MAPLE films fabricated at 3 different deposition times on OTS and SiO_2. The diffraction patterns of films fabricated on two types of substrates at the same deposition time appear qualitatively similar. For each substrate, the diffraction intensity increases with deposition times due to the increase in the amount of diffracting crystallites within the samples. At the shortest deposition time of 3 min, only the first order of the alkyl-stacking peak (100) at ca. 0.39

$Å^{-1}$ is visible along the vertical q_z direction. The second order peak (200) and the third order peak (300) only appear along the vertical direction in samples deposited after 30 min and 180 min. Also visible after 30 min of deposition is the (010) π-stacking peak along q_{xy} axis at ca. 1.67 $Å^{-1}$, indicative of bias toward edge-on orientation of polymer crystallites in which the polymer side-chain orients in the out-of-plane direction and the π-stacking orients in the in-plane direction.[16] For films deposited on both substrates, the azimuthal breadth of the (h00) peaks increases with deposition time (film thickness), providing qualitative evidence of more random orientation of crystallites as the films become thicker. While this behavior has been widely observed in spin-cast P3HT films,[8,17,18] this is the first time such behavior is reported in MAPLE-deposited samples.

Although information extracted from GIWAXS measurement is generally useful for qualitative analysis of the film structure, the raw data collected with a 2D detector is geometrically distorted and thus does not reflect the true reciprocal space. More importantly, any crystallites that have the scattering vector q close to the perpendicular direction with the substrate will not be detected in GIWAXS geometry because the scattering vector q does not intersect with Ewald sphere in this regime.[7,8] With respect to the (100) reflection in P3HT, the accessible range of the polar angle χ between the q_{100} vector and the pole vector in GIWAXS measurement is from θ_B = 2.036° to 90°, as calculated from our experiment configuration. In order to resolve data for $\chi < \theta_B$, we followed the previously reported procedures introduced by Baker et al.[7] and performed a local specular measurement. In the local specular condition, the samples are tilted at the incident angle $\alpha = \theta_B$ so that the pole of the orientation sphere of the (100) peak intersects with the Ewald sphere. The complete accessible range of χ in the local specular measurement is from 0° to 60°.[7,8] Representative 2D detector images of the local specular measurements are

shown in the insets of Figure 5.3. Similar to the GIWAXS data, the local specular data of samples on both SiO_2 and OTS substrates exhibits broadening of the azimuthal breadth of the (100) diffraction peaks with increasing deposition times, suggesting more random crystallite orientations as the films become thicker. The complete pole figures of the (100) reflection are then compiled by merging the partial pole figures extracted from GIWAXS ($\theta_B < \chi < 90°$) and local specular ($0° < \chi < 20°$) diffraction data. The stitching range of χ is chosen such as the two partial pole figures overlay and their local derivatives are identical. An example of complete pole figure construction is shown in Appendix. Complete pole figures of the (100) diffraction peaks of P3HT samples fabricated at different deposition times on OTS and SiO_2 are shown in Figure 5.4, both in semi-log scale in (a), (b) and double log scale in (c), (d).

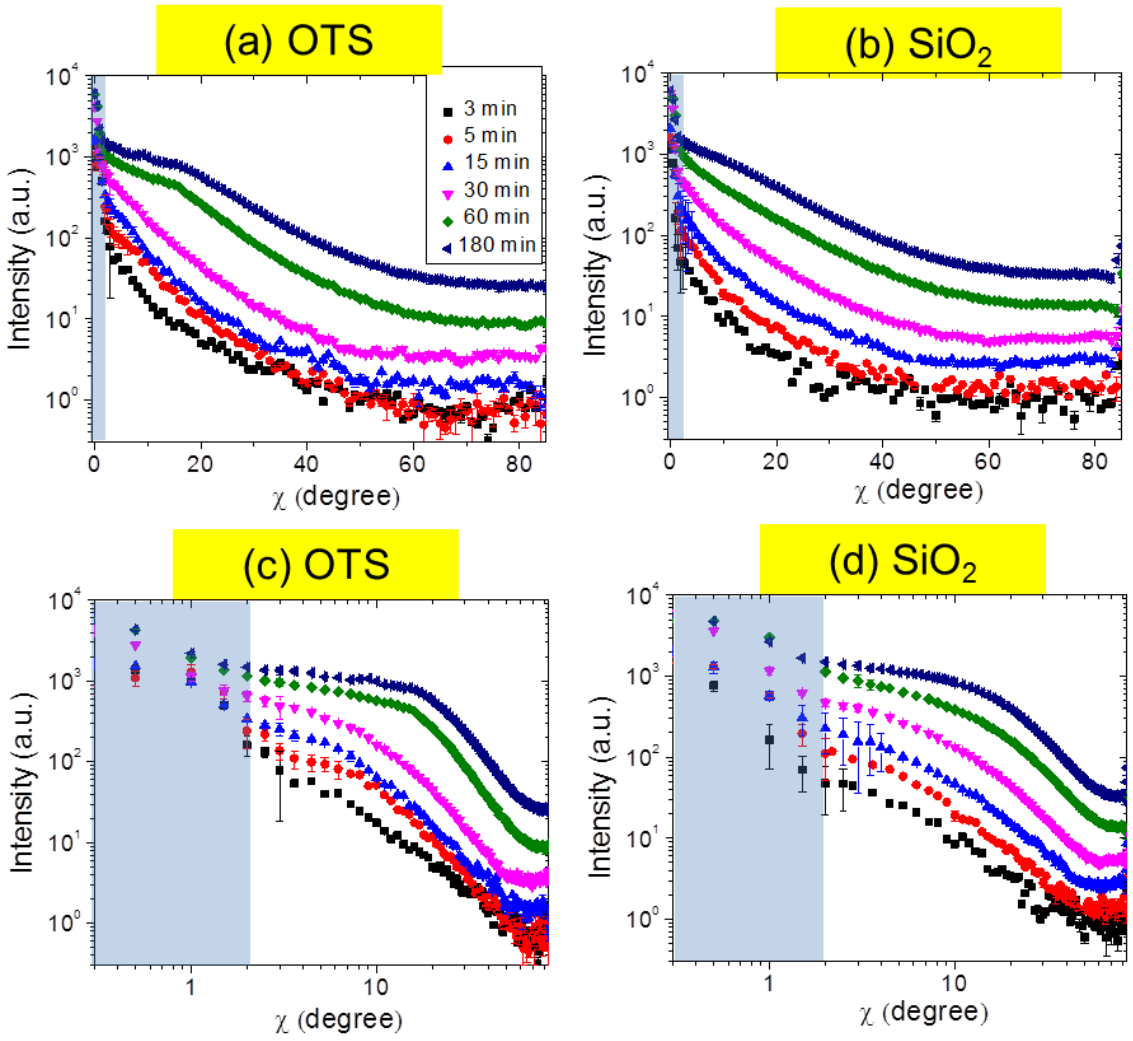

Figure 5.4: Complete pole figures of the (100) diffraction peak for films deposited on top of (a) OTS and (b) SiO_2 at different deposition times. The same data are plotted on a log-log scale in (c) and (d) to emphasize different crystallite populations. The shaded areas in each figure represent the data from highly-oriented crystals extracted from local specular measurement. The error bars were calculated from the uncertainty of the peak fitting.

For all samples fabricated at different deposition times on both types of substrates, we observed relatively strong intensity near $\chi = 0°$, indicated by the shaded areas in Figure 5.4(a)-(d), which decreases as χ increases. This shows that in MAPLE-deposited samples, despite the highly disordered morphologies reported in our earlier studies,[1,2] there exists a large population of highly-oriented crystallites having the (100) stacking direction almost perfectly perpendicular to

the substrates. Highly-oriented crystallites have also been observed for spin-cast films of P3HT[8,19] and other semicrystalline polythiophenes.[20,21] With increasing deposition time, the distribution of the pole figures becomes broader for samples on both substrates, indicating that the average orientation of crystallites becomes more random as the films become thicker. This observation is in good agreement with visual inspection of the raw detector images in Figure 5.3 but in a more quantitative manner.

Here, it is instructive to divide the pole figures into two components based on different crystallite orientations and monitor their growth separately. We define the crystallites with $\chi < \theta_B = 2.036°$ as "highly-oriented" crystals and the remaining crystallites with $\chi > \theta_B$ as "misoriented" crystals. In order to emphasize these two different crystallite populations, the pole figures were plotted in double log scale in Figure 5.4(c) and (d). We note that direct comparison between crystallite populations, and thus degree of crystallinity (DoC), at different deposition times could be challenging because at a fixed angle of incidence, the diffraction intensity strongly depends on film thickness: Since the angle of incidence used in GIWAXS measurement is below the critical angle of the substrate, the incident beam is largely reflected at the polymer/substrate interface. Interference between the incident and reflected beams will produce standing waves, amplifying the signal at certain depths in the films. These effects are strongly dependent on film thickness, making direct comparison between films with different thicknesses difficult.[5,22] However, from the evolution of complete pole figures in Figure 5.4 we are able to extracted some valuable information regarding the crystallization process in MAPLE.

First, we observe that during MAPLE deposition process, the growth of the highly-oriented crystals seems to be decoupled from that of the misoriented crystals. Compared to the growth of misoriented crystals which continues during the whole course of deposition, the

growth of highly-oriented crystals is considerably suppressed beyond 60 min, as demonstrated in Figure 5.4(c) and (d). We hypothesize that the highly-oriented crystals can only nucleate and grow on very flat dielectric interfaces. As we showed earlier in AFM measurement, at the early stage of MAPLE deposition, the substrates are not fully covered. Thus the polymer droplets can be deposited atop the uncovered portions of the flat substrates, promoting the growth of highly-oriented crystals. At deposition times longer than 60 min, the substrates are fully covered and the new polymer crystals can only grow on top of existing polymer layers. Therefore at this stage, the growth of highly-oriented crystals is hindered and only misoriented crystals continue to grow. Later on we will show that this hypothesis is further supported by several other key observations. Second, by calculating the ratio between DoC of samples fabricated on OTS and SiO_2 at each deposition time, we are able to discern the effect of substrate chemistry on overall DoC of the samples. To facilitate DoC comparison, the same X-ray exposure time and angle of incidence were used for all measurements. The diffraction intensity at each polar angle is multiplied by a factor of $\sin(\chi)$ for geometrical correction.[23] The DoC of highly-oriented crystal and misoriented crystals is then calculated by integrating the geometrically corrected intensity from 0° to θ_B and θ_B to 85°, respectively. Data at $\chi > 85°$ is impacted by standing waves and thus excluded from the analysis. Shown in Figure 5.5 is the DoC ratio of samples deposited on OTS and SiO_2 as a function of deposition time.

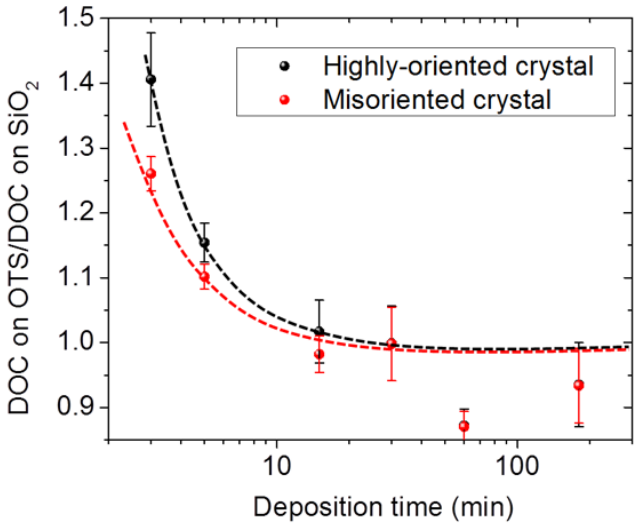

Figure 5.5: DoC ratio of samples deposited on OTS and SiO_2 as a function of deposition time. The errors for DoC calculation were first computed by measuring standard deviation from 4 different spots on the same sample. The error bars of DoC ratio were then calculated from the uncertainty of DoC estimation following an error propagation approach.

As seen in Figure 5.5, at the early stages of deposition the substrate chemistry shows a strong influence on DoC of the samples, with a more pronounced effect on highly-oriented crystals than misoriented crystals. At the earliest deposition time of 3 min, the highly-oriented crystals on OTS are ca. 40% more crystalline than those on SiO_2 and the misoriented crystals on OTS are ca. 25% more crystalline than those on SiO_2. As the films continue to grow, the differences between samples on OTS and SiO_2 quickly vanish (note the log scale of *x* axis) and the DoC becomes comparable at longer deposition times for both highly-oriented crystals and misoriented crystals, consistent with our previous finding.[2] The stronger impact of substrate chemistry on highly-oriented crystals is another indication of their preferential growth on the dielectric substrates as hypothesized above. We note that although the effect of substrate chemistry on the DoC of misoriented crystals is not as strong as on the highly-oriented crystals,

it still exerts some certain influences, especially in thinner films. It could be that similar to spin-cast samples,[8,24] the dielectric interface in MAPLE-deposited samples hosts not only highly-oriented crystals but also some misoriented crystals/amorphous polymer chains as well.

The full width at half-maximum (FWHM) of the (100) peak reflects the coherence length along the alkyl-stacking direction. Because we collected WAXS data both in grazing incidence and local specular conditions, we were able to extracted two separate sets of FWHM data. Some discrepancies between the two sets of data were observed: for the same sample at the same polar angle, we always observed a smaller FWHM and lower peak position q of the (100) peak in local specular data compared to GIWAXS data (see Appendix). The discrepancies could originate from a couple of reasons. First, in GIWAXS measurements, where the angle of incidence is below the critical angle of the substrate, two Bragg peaks are produced for each diffraction plane that are associated with transmitted and reflected beams. The two peaks are clearly resolved in grazing incidence small angle X-ray scattering measurements,[22] but appear as one broad peak at higher q in GIWAXS due to the resolution limits of this experiment. In local specular measurements, where the angle of incidence is well above the critical angle, there is little reflection at the polymer-substrate interface and only one Bragg peak is detected. Second, there are other possible contributions to the broadening of a Bragg peak from instrumental resolutions that include contributions from beam divergences, energy bandwidth and geometric smearing.[25] The combined resolution broadening is quite significant in GIWAXS measurement but is negligibly small in local specular measurement (see the resolution analysis in Appendix). FWHM data collected from the local specular condition is thus more accurate and reflects the truer FWHM of the Bragg peak.

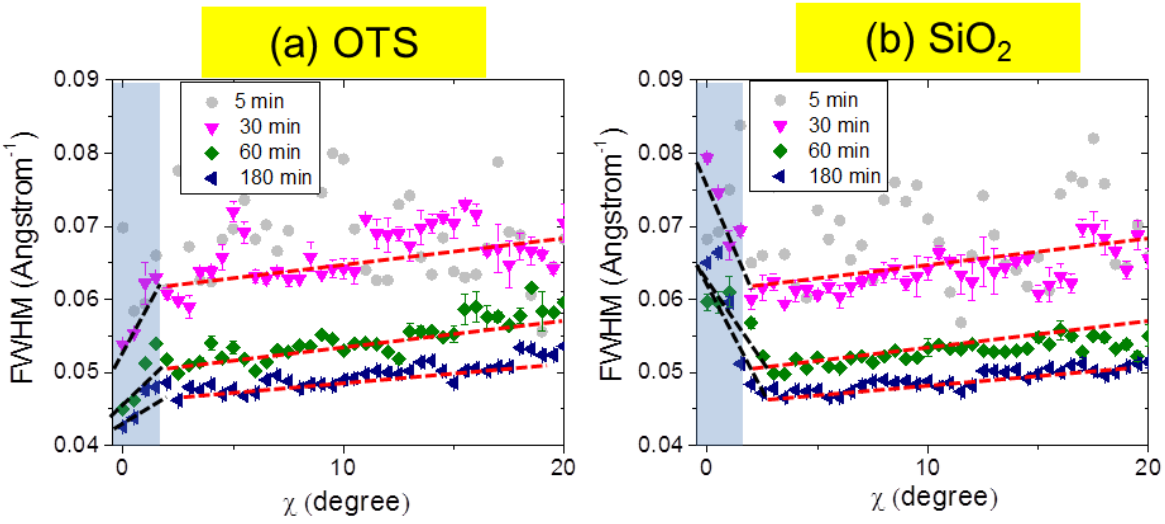

Figure 5.6: FWHM of the (100) peak extracted from local specular measurement of samples deposited on (a) OTS and (b) SiO_2 substrates at different deposition times. The shaded area represents the data extracted from "highly-oriented" crystals ($\chi<\theta_B$). The error bars were calculated from the uncertainty of the peak fitting. The dashed lines are guides to the eyes. The red dashed lines represent the trends for misoriented crystals and the black dashed lines represent the trends for highly-oriented crystals. The red dashed lines are in the same position in both (a) and (b).

Figure 5.6 depicts the FWHM extracted from local specular measurement of the (100) peak as a function of the polar angle χ for samples on (a) OTS and (b) SiO_2. We note that at deposition times shorter than 30 min, the diffraction signal of the samples is weak and the FWHM values extracted from our fit tend to be noisy such as the data of 5 min samples shown in Figure 5.6(a) and (b). For samples deposited at or longer than 30 min, we observe a general trend that the FWHM decreases with increasing deposition times for samples on both OTS and SiO_2 substrates. This suggests that during MAPLE-deposition, the average crystallite coherence length L_{100} along the alkyl-stacking direction increases according to Scherrer equation.[25] Here, it is important to note that the coherence length L_{100} calculated from Scherrer equation is the distance over which unit cells are spatially correlated, which includes contribution not only from crystallite size but also from paracrystallinity.[26] However, we believe that the narrowing of the

peak with increasing deposition time at least partially originates from increases in crystallite size, which is corroborated by UV-vis measurements reported in Figure 5.2. Interestingly, L_{100} appears to continuously increase even after the longest deposition time of 180 min. This is in contrast to spin-cast P3HT films where the crystallite coherence length increased with film thickness but saturated after reaching a certain threshold value.[8] We postulate that the crystallization process of MAPLE involves the addition of polymer chains within new globules to the polymer crystallites inside the existing globules. The merging of discrete globules unit during MAPLE deposition contributes to the film formation and assists crystal growth. The growth of crystals during the course of deposition is rather surprising, given the fact that the fabrication process in this work was performed at temperature close to 0ºC which is likely below the glass transition temperature of P3HT.[27] We suspect that although most vaporized solvent molecules were pumped away under the high vacuum environment, a small amount of them still remains within the polymer clusters right before reaching the substrates. The remaining solvent molecules could reduce the effective T_g of P3HT, providing chain mobility that assists additive crystal growth during the deposition process.[28] The similar additive growth behavior in MAPLE-deposited poly(ethylene oxide) films has also been reported in a recent work by Jeong and co-workers.[29]

Also worthy of discussion is the dependence of FWHM on the polar angle χ. For $\chi > \theta_B$ (misoriented crystals), the FWHM increases as χ increases, suggesting that crystallites oriented away from the substrate normal tends to have smaller L_{100}. Moreover, the FWHM of misoriented crystals in samples deposited at the same deposition time is insensitive to substrate chemistry (Note that the red dashed lines in Figure 5.6(a) and (b) are set at the same location for ease of comparison). However, for $\chi < \theta_B$ the FWHM distribution drastically changes and is characteristically different for samples on OTS and SiO_2. While the FWHM reduces quite

significantly as χ approaching 0° for sample deposited atop OTS, the FWHM shows an opposite trend and greatly enhances toward χ = 0° for samples deposited atop SiO_2. This suggests that whereas L_{100} of misoriented crystals are comparable for samples on both substrates, L_{100} of highly-oriented crystals is substantially smaller for samples on SiO_2 compared to samples on OTS. Inputting the FWHM values in Figure 5.6 into Scherrer equation[25] demonstrates that for the thickest films (at 180 min of deposition), the coherence length of the misoriented crystals at χ = 20° is ca. 10 nm (≈ 6 *d*-spacings across side-chain direction) for both substrates. However, the coherence length of the highly-oriented crystals at χ = 0° is ca. 13 nm (≈ 8 *d*-spacings) on OTS substrate but only 8 nm (≈ 5 *d*-spacings) on SiO_2 substrate. This shows that the coherence length of highly-oriented crystals strongly depends on the chemistry of the substrate and further suggests that the highly-oriented crystals only nucleate and grow from the dielectric interfaces. A schematic representation of structural development during the course of MAPLE deposition is summarized in Figure 5.7.

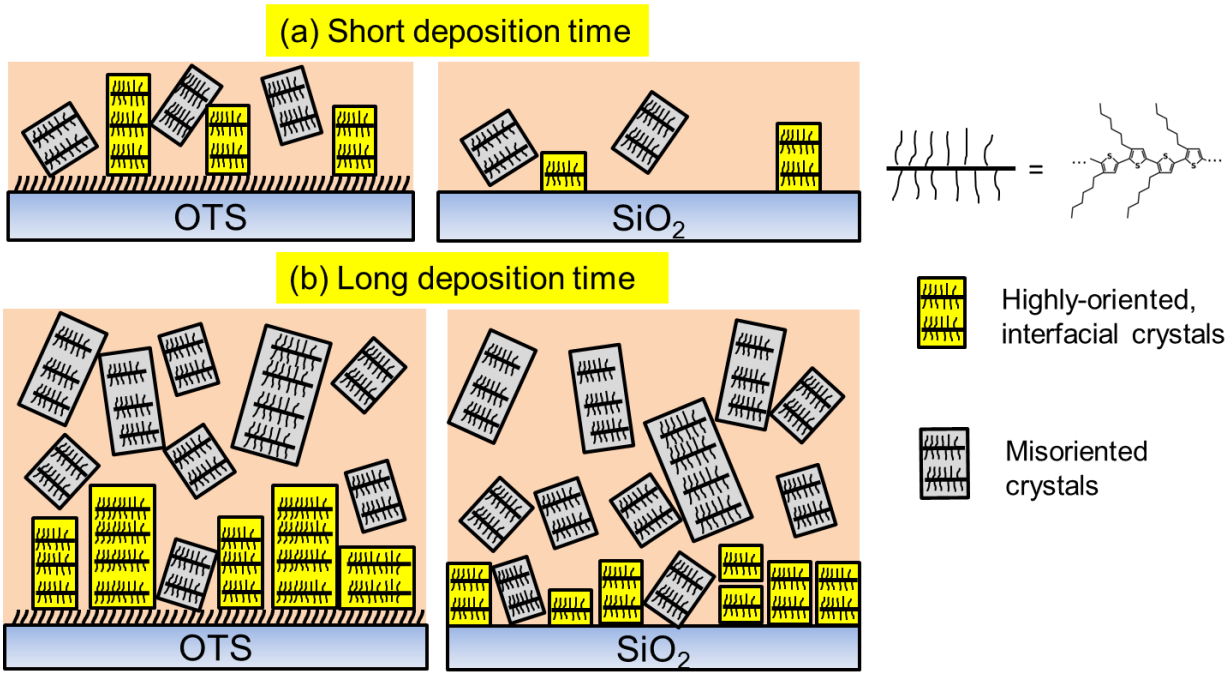

Figure 5.7: Schematic representation of the structure of MAPLE-deposited samples at (a) short and (b) long deposition times. The highly-oriented crystals (highlighted in yellow) grow from the dielectric interface; the misoriented crystals (highlighted in grey) grow from the bulk and partially from the dielectric interface. At the early stage of deposition, the substrate chemistry exerts strong influence on the growth of both types of crystals which higher DoC on OTS than on SiO_2. As the films develop, the effect of substrate chemistry on DoC diminishes and the films consists of misoriented crystal from the bulk with comparable sizes on both substrates and highly oriented crystals at the buried interfaces which larger size on OTS compared to SiO_2 substrate.

5.3.4. Correlation between morphology and in-plane transport characteristics

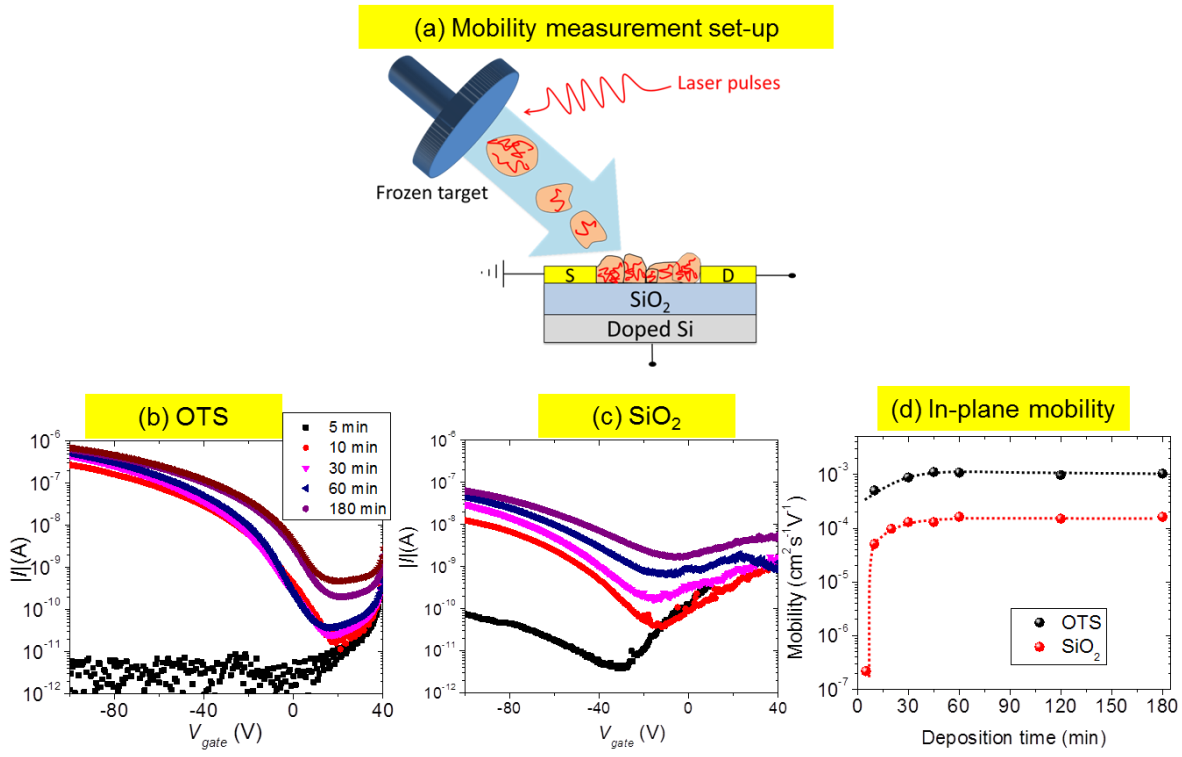

Figure 5.8: (a) Bottom-gate bottom-contact transistor configuration used in the mobility measurement. (b)(c) Evolution of transistor transfer characteristics of MAPLE samples deposited on top of OTS and SiO_2 substrates measured in saturation regime (V_D = -80V). (d) Calculated in-plane hole mobility as a function of deposition time

In an attempt to understand the role of thin film microstructure on carrier transport, we fabricate bottom-gate, bottom-contact thin-film transistor (TFT) to study the in-plane transport characteristics of the samples as depicted in Figure 5.8(a). We chose to use the bottom-contact instead of top-contact configuration in order to monitor the transport characteristics of the exact same devices during the course of deposition. Shown in Figure 5.8(b) and (c) is the evolution of transistor transfer curves of devices fabricate atop OTS and SiO_2 substrates as a function of deposition time. For both types of devices, we observe quite abrupt increase of current as going from 5 to 10 min of deposition. This sudden rise of current likely originates from the coalescence of the globular islands as suggested by our AFM measurements. The coalescence of polymer

islands helps to create interconnected pathways for charge carriers to transport from source to drain electrode. Beyond 10 min, the current slowly increases with deposition time, with weaker current for device fabricated on top of SiO_2, indicative of lower carrier mobility compared to OTS device. Also worth mentioning is the continuous increase in magnitude of the leakage current (or off current) I_{off} with deposition time, scaling with the amount of material deposited on top of the substrates. The leakage current is higher in SiO_2 device compared to OTS device, indicative of higher level of unwanted doping in SiO_2 device which likely due to the presence of moisture-sensitive hydroxyl groups on SiO_2 substrate.

The extracted in-plane mobilities of OTS and SiO_2 devices versus deposition time are shown in Figure 5.8(d). For OTS device, the mobility first increases and then reaches a plateau value of ca. 1.0×10^{-3} $cm^2V^{-1}s^{-1}$ after approximately 60 min. Similar trend is observed for SiO_2 device but the mobility is always lower than OTS device and saturates at ca. 1.7×10^{-4} $cm^2V^{-1}s^{-1}$. We note that at deposition time of 5 min the mobility of SiO_2 device is considerably suppressed and the mobility of OTS device is unmeasurable, probably due to the lack of connection between polymer islands as mentioned above. Beyond 60 min the hole mobility does not improve despite the increase in overall aggregate size and crystallite coherence length. The increase and plateau out of mobilities coincide with the structure development of the highly-oriented crystals, suggesting that the highly-oriented crystals at the buried interface control transport in TFT.

The higher mobility of OTS device compared to SiO_2 device is also consistent with the larger crystallite coherence length existing at the OTS-treated dielectric interface. It is well-established that passivating the dielectric substrate with self-assembled monolayers such as OTS improves TFT performance of spin-cast conjugated polymers, and the origin of the enhanced mobility is at least partially structural.[8,30,31] An OTS monolayer also helped improve TFT

mobility in MAPLE-deposited films, although the effect is not as strong as in the case of spin-cast conjugated polymers.[1,2] Here, by using the complementary local specular measurement, for the first time we have shown that the effect of OTS on mobility of device fabricated using MAPLE originates from the improved polymer order near the dielectric interfaces, which has been elusive to date. Our data suggests that similar to spin-cast samples, in MAPLE samples the OTS monolayer can also act as a nucleation layer and promote the growth of large-sized, highly-oriented crystallites near the dielectric interfaces. Furthermore, the presence of a large population of highly-oriented crystals at the buried interface of MAPLE-deposited samples could be used to explain the superior TFT mobilities of MAPLE-deposited devices compared to the spin-cast analogs reported in our previous studies, despite their highly disordered morphologies.[1,2] Our results highlight the importance of characterizing the polymer structure near the buried interfaces in evaluating TFT performance.[32]

5.4. CONCLUSION

In this work, we studied the molecular structure in relation to in-plane transport properties of MAPLE-deposited P3HT films as a function of deposition time on two different substrates: OTS and SiO_2. Through quantitative characterizations using X-ray diffraction and optical techniques, we observed the increase in the overall aggregate size and crystallite coherence length, indicative of additive growth mechanism during MAPLE deposition process. Complete pole figures showed that in MAPLE-deposited samples, there exists a large population of highly-oriented crystallites at the dielectric interface having the side-chain oriented almost perfectly perpendicular to the substrates. The growth of these highly-oriented crystals decoupled from the remaining misoriented crystals and strongly depended on the substrate chemistries. At early deposition stages, the population of highly-oriented crystals is higher on OTS substrate

compared to SiO_2 substrates and the difference diminished as the film become thicker. Additionally, the OTS monolayer promotes the growth of large-sized highly-oriented crystals at the buried interface; the effect of OTS treatment on the size of misoriented crystals is negligible. The implications of the morphology on charge transport were illustrated by studying the evolution of field-effect mobility, yielding results suggesting that transport in thin-film transistor is controlled by the highly-oriented crystals growing at the buried interfaces. Our study offers fundamental understanding of crystallization mechanism in MAPLE in tight connection to carrier transport properties, providing an important step toward exploiting MAPLE to engineer structures in various conjugated polymer-based electronic devices.

5.5. APPENDIX

5.5.1. Complete Pole Figure Constructions

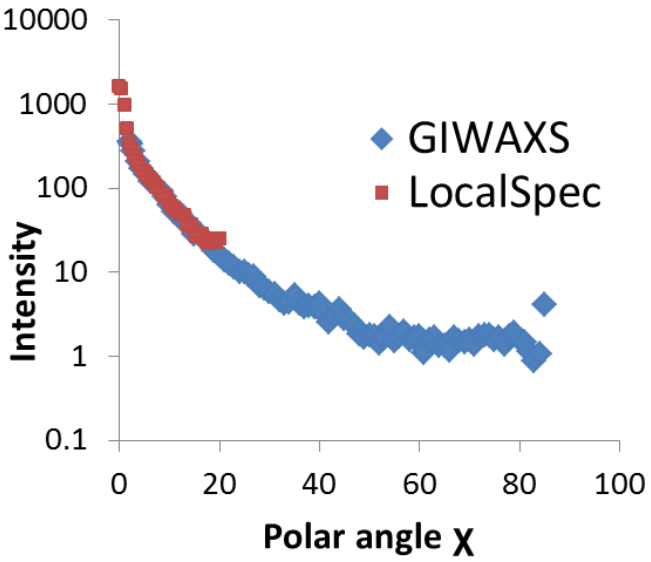

Figure 5.9: Representative construction of complete pole figures by combining partial pole figures extracted from GIWAXS and local specular measurements

The intensity versus χ plots extracted from the grazing incidence ($\theta_B < \chi < 90°$) and local-specular ($0° < \chi < 20°$) diffraction patterns are not on an absolute scale. Thus to create the complete pole figure, the intensity of GIWAXS pole figure is kept constant and the intensity of the local-specular pole figure is scaled with an appropriate pre-factor so that the two partial pole figures overlay (Figure 5.9).

5.5.2. FWHM Discrepancies between Local Specular and GIWAXS Measurements

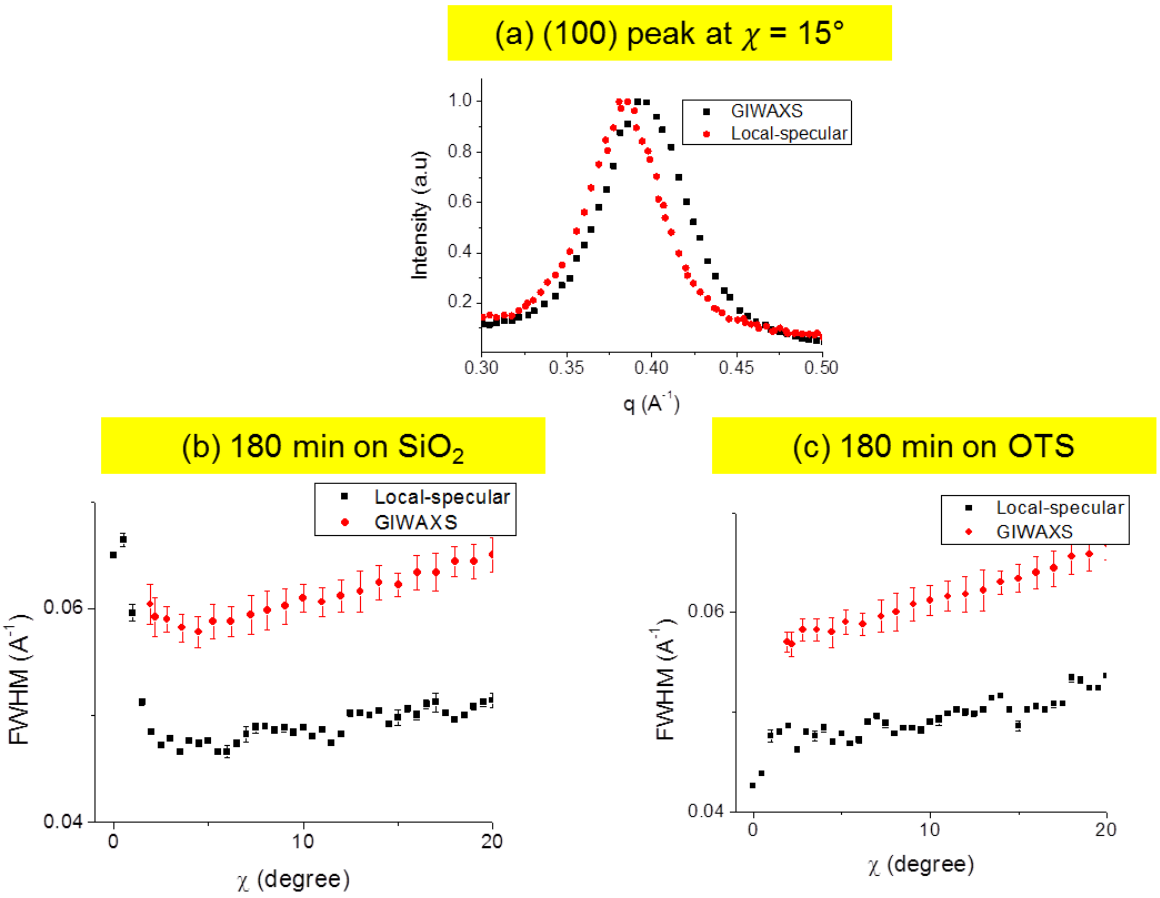

Figure 5.10: (a) An example of (100) peak at χ = 15° of the same sample (180 min on SiO_2). The peak measured by GIWAXS is broader and shifts to higher *q*. (b)(c) Comparison of the FWHM of the (100) peak extracted from GIWAXS and local specular measurements. The FWHM values

extracted from GIWAXS always higher than the ones extracted from local-specular measurement. Note that data below $\theta_B \approx 2°$ is not measurable in GIWAXS geometry. Origins of the discrepancies are explained in the text of the manuscript.

5.5.3. WAXS Resolution Analysis

The measured peak breadth ΔB_{exp} of a particular reflection *hkl* in WAXS experiments contains contributions from both the samples ΔB_{hkl} and resolution of experimental apparatus ΔB_{res}. Thus the experimental width must be corrected in order to resolve the true breadth of the peak

$$\Delta B_{hkl} = ((\Delta B_{\exp})^2 - (\Delta B_{res})^2)^{1/2} \quad (1)$$

For WAXS measurements, ΔB_{res} includes vertical and horizontal beam divergence contribution ΔB_{div}, bandwidth contribution ΔB_{bw} and geometrical contribution ΔB_{geo}.[25]

1. *Beam divergence contribution* ΔB_{div}

Assuming an elliptical beam profile having intrinsic beam divergences in the vertical and horizontal direction σ_V and σ_H, the beam diversion ΔB_{div} for a given detector azimuth angle ϕ is as follow:

$$\Delta B_{div} = \frac{1}{\sqrt{\frac{\cos^2(\phi)}{\sigma_H^2} + \frac{\sin^2(\phi)}{\sigma_V^2}}} \quad (2)$$

Inputting σ_V = 3.7μrad and σ_H = 12 μrad[4] into equation (2) the beam divergence contribution can be calculated.

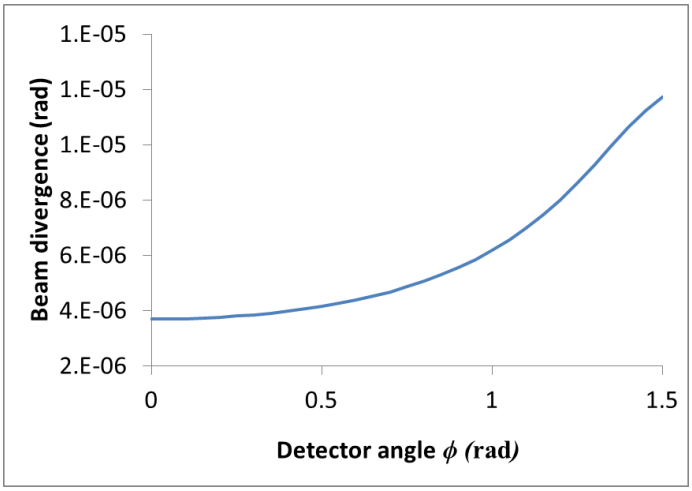

Figure 5.11. Beam divergence as a function of detector angle ϕ

The ΔB_{hkl} of P3HT's (100) reflection in our experiment ranges from 0.01 to 0.02 rad. As seen in Figure 5.11, the beam divergence contribution ΔB_{div} is in the microradian range and thus negligibly small.

2. *Bandwidth contribution* ΔB_{bw}

The peak broadening due to bandwidth ΔB_{bw} is

$$\Delta B_{bw} = 2\eta \tan\frac{2\theta}{2} \qquad (3)$$

Here, the energy bandwidth $\eta = 10^{-4}$ for Si(111) optics used in our beamline. The bandwidth contribution is computed as follow:

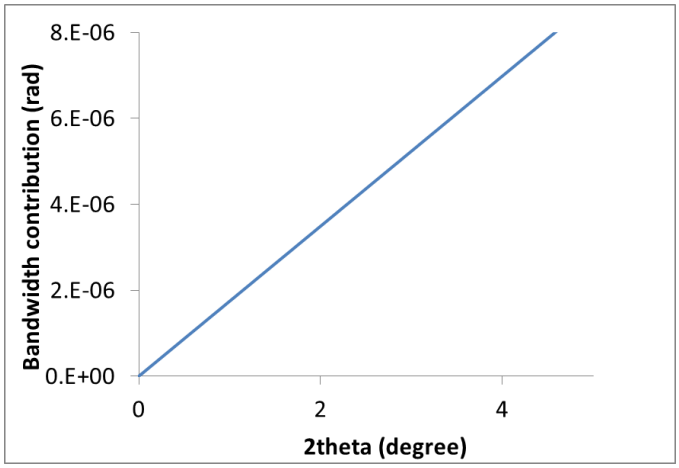

Figure 5.12. Bandwidth resolution as a function of 2θ

Note that $2\theta_B \approx 4°$ for (100) reflection in P3HT, thus the bandwidth contribution for the broadening of (100) peak is in the microradian range and also negligibly small.

3. *Geometrical contribution* ΔB_{geo}

The peak broadening due to geometry is projection of footprint divided by sample to detector distance. It can be calculated as:

$$\Delta B_{geo} = \frac{w\tan(2\theta)}{L}$$

Here, $w = 8.1 \times 10^{-3}$ m is the beam footprint in GIWAXS measurement and $w = 5.6 \times 10^{-4}$ m is the beam footprint in local specular measurement. L = 0.228 m is the sample-to-detector distance.

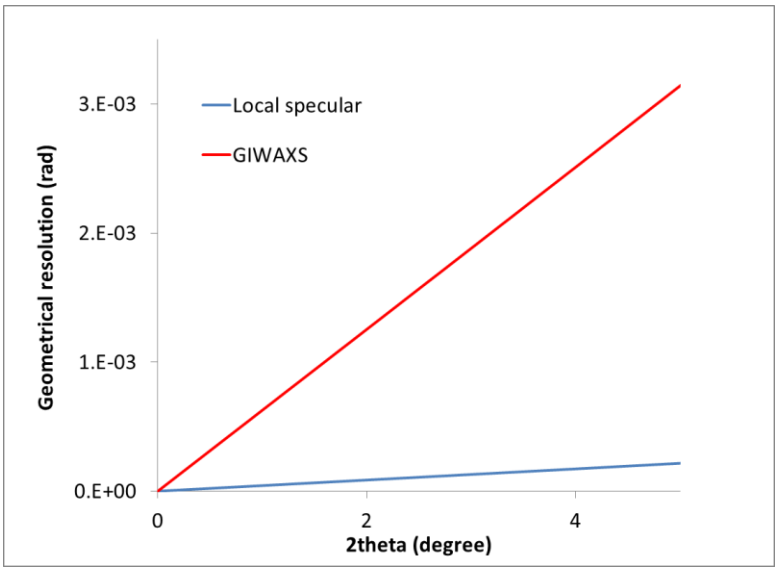

Figure 5.13 Geometrical resolutions in GIWAXS and local specular measurements as a function of 2θ

As seen in Figure 5.13, the geometrical effect from the size of the footprint is in the miliradian range for P3HT's (100) reflection and thus is the largest of the three contributions. The geometrical resolution in GIWAXS measurement is worse than in local specular measurement because of the larger beam footprint.

4. *Calculation of experimental resolution from divergence, bandwidth and geometry contributions*

The combined resolution to the peak broadening from the beam divergence, beam bandwidth and geometric smearing can be expressed as:

$$\Delta B_{res}(2\theta,\phi) = [\Delta B_{div}(\phi)^2 + \Delta B_{bw}(2\theta)^2 + \Delta B_{geo}(2\theta)^2]^{1/2}$$

However, since ΔB_{geo} >> ΔB_{div} and ΔB_{bw}, the resolution is dominated by the geometric term. Thus the resolution can be expressed in term of scattering vector resolution as follow:

$$\Delta q_{res} = \frac{4\pi}{\lambda}\cos(\frac{2\theta}{2})\Delta B_{res} \approx \frac{4\pi}{\lambda}\cos(\frac{2\theta}{2})\Delta B_{geo}$$

Here, λ = 1.14162 Å is the X-ray wavelength.

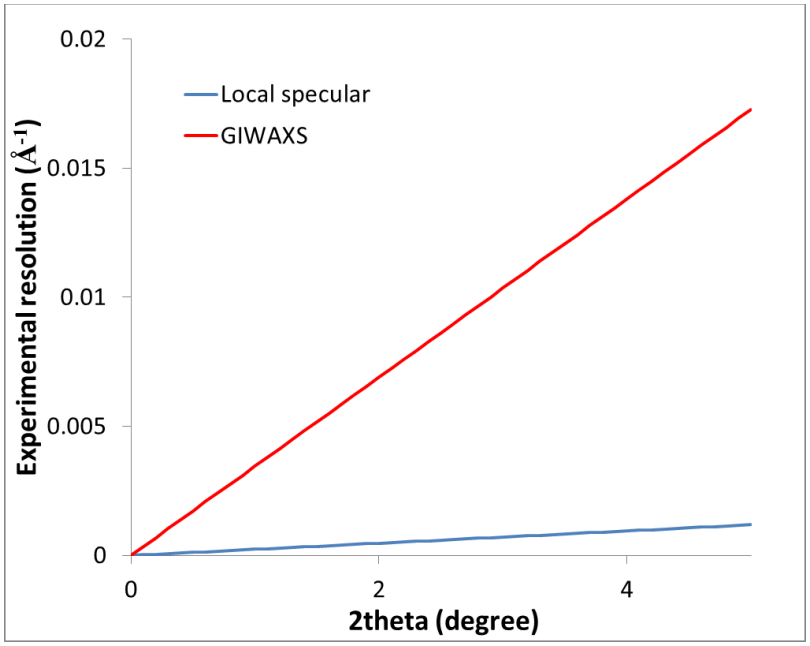

Figure 5.14. Combined experimental broadening as a function of 2θ

Figure 5.14 demonstrates the combined experimental broadening as a function of 2θ in terms of scattering vector resolution ($Å^{-1}$). The experimental broadening from GIWAXS measurement is more prominent than from local specular measurement. With regard to the (100) diffraction peak in P3HT ($2\theta_B \approx 4°$), the experimental broadening is ca. 0.014 $Å^{-1}$ in GIWAXS measurement and ca. 0.001 $Å^{-1}$ in local specular measurement. The combined resolution broadening is thus negligibly small in local specular measurement.

5.6. REFERENCES

(1) Li, A.; Dong, B. X.; Green, P. Influence of Morphological Disorder on In- and Out-of-Plane Charge Transport in Conjugated Polymer Films. *MRS Commun.* **2015**, *5* (4), 593–598.

(2) Dong, B. X.; Li, A.; Strzalka, J.; Stein, G. E.; Green, P. F. Molecular Organization in MAPLE-Deposited Conjugated Polymer Thin Films and the Implications for Carrier Transport Characteristics. *J. Polym. Sci. Part B Polym. Phys.* **2017**, *55* (1), 39–48.

(3) Pate, R.; Lantz, K. R.; Stiff-Roberts, A. D. Tabletop Resonant Infrared Matrix-Assisted Pulsed Laser Evaporation of Light-Emitting Organic Thin Films. *IEEE J. Sel. Top. Quantum Electron.* **2008**, *14* (4), 1022–1030.

(4) Jiang, Z.; Li, X.; Strzalka, J.; Sprung, M.; Sun, T.; Sandy, A. R.; Narayanan, S.; Lee, D. R.; Wang, J. The Dedicated High-Resolution Grazing-Incidence X-Ray Scattering Beamline 8-ID-E at the Advanced Photon Source. *J. Synchrotron Radiat.* **2012**, *19* (4), 627–636.

(5) Vaselabadi, S. A.; Shakarisaz, D.; Ruchhoeft, P.; Strzalka, J.; Stein, G. E. Radiation Damage in Polymer Films from Grazing-Incidence X-Ray Scattering Measurements. *J. Polym. Sci. Part B Polym. Phys.* **2016**, 1–13.

(6) Jiang, Z. GIXSGUI : A MATLAB Toolbox for Grazing-Incidence X-Ray Scattering Data Visualization and Reduction, and Indexing of Buried Three-Dimensional Periodic Nanostructured Films. *J. Appl. Crystallogr.* **2015**, *48* (3), 917–926.

(7) Baker, J. L.; Jimison, L. H.; Mannsfeld, S.; Volkman, S.; Yin, S.; Subramanian, V.; Salleo, A.; Alivisatos, A. P.; Toney, M. F. Quantification of Thin Film Crystallographic Orientation Using X-Ray Diffraction with an Area Detector. *Langmuir* **2010**, *26* (11), 9146–9151.

(8) Jimison, L. H.; Himmelberger, S.; Duong, D. T.; Rivnay, J.; Toney, M. F.; Salleo, A. Vertical Confinement and Interface Effects on the Microstructure and Charge Transport of P3HT Thin Films. *J. Polym. Sci. Part B Polym. Phys.* **2013**, *51* (7), 611–620.

(9) Spano, F. C. Modeling Disorder in Polymer Aggregates: The Optical Spectroscopy of Regioregular poly(3-Hexylthiophene) Thin Films. *J. Chem. Phys.* **2005**, *122* (23), 234701.

(10) Spano, F. C.; Silva, C. H- and J-Aggregate Behavior in Polymeric Semiconductors. *Annu. Rev. Phys. Chem.* **2014**, *65*, 477–500.

(11) Leveugle, E.; Zhigilei, L. V. Molecular Dynamics Simulation Study of the Ejection and Transport of Polymer Molecules in Matrix-Assisted Pulsed Laser Evaporation. *J. Appl. Phys.* **2007**, *102* (7), 1–19.

(12) Shepard, K. B.; Arnold, C. B.; Priestley, R. D. Origins of Nanostructure in Amorphous Polymer Coatings via Matrix Assisted Pulsed Laser Evaporation. *Appl. Phys. Lett.* **2013**, *103* (12), 123105.

(13) Clark, J.; Silva, C.; Friend, R.; Spano, F. Role of Intermolecular Coupling in the Photophysics of Disordered Organic Semiconductors: Aggregate Emission in Regioregular Polythiophene. *Phys. Rev. Lett.* **2007**, *98* (20), 206406.

(14) Spano, F. C. Absorption in Regio-Regular poly(3-Hexyl)thiophene Thin Films: Fermi Resonances, Interband Coupling and Disorder. *Chem. Phys.* **2006**, *325* (1), 22–35.

(15) Gierschner, J.; Huang, Y.-S.; Van Averbeke, B.; Cornil, J.; Friend, R. H.; Beljonne, D. Excitonic versus Electronic Couplings in Molecular Assemblies: The Importance of Non-Nearest Neighbor Interactions. *J. Chem. Phys.* **2009**, *130* (4), 44105.

(16) Sirringhaus, H.; Brown, P. J.; Friend, R. H.; Nielsen, M. M.; Bechgaard, K.; Langeveld-Voss, B. M. W.; Spiering, A. J. H.; Janssen, R. A. J.; Meijer, E. W.; Herwig, P.; et al. Two-Dimensional Charge Transport in Self-Organized, High-Mobility Conjugated Polymers. *Nature* **1999**, *401* (6754), 685–688.

(17) Porzio, W.; Scavia, G.; Barba, L.; Arrighetti, G.; Milita, S. Depth-Resolved Molecular Structure and Orientation of Polymer Thin Films by Synchrotron X-Ray Diffraction. *Eur. Polym. J.* **2011**, *47* (3), 273–283.

(18) Joshi, S.; Joshi, S.; Grigorian, S.; Grigorian, S.; Pietsch, U.; Pietsch, U.; Pingel, P.; Pingel, P.; Zen, A.; Zen, A.; et al. Thickness Dependence of the Crystalline Structure and Hole Mobility in Thin Films of Low Molecular Weight Poly(3-Hexylthiophene). *Macromolecules* **2008**, *41* (18), 6800–6808.

(19) Joseph Kline, R.; McGehee, M. D.; Toney, M. F. Highly Oriented Crystals at the Buried Interface in Polythiophene Thin-Film Transistors. *Nat. Mater.* **2006**, *5* (3), 222–228.

(20) Chabinyc, M. L.; Toney, M. F.; Kline, R. J.; McCulloch, I.; Heeney, M. X-Ray Scattering Study of Thin Films of Poly(2,5-bis(3-Alkylthiophen-2-yl)thieno[3,2- B]thiophene). *J. Am. Chem. Soc.* **2007**, *129* (11), 3226–3237.

(21) Jimison, L.; Salleo, A.; Chabinyc, M.; Bernstein, D.; Toney, M. Correlating the Microstructure of Thin Films of poly[5,5-bis(3-Dodecyl-2-Thienyl)-2,2-Bithiophene] with Charge Transport: Effect of Dielectric Surface Energy and Thermal Annealing. *Phys. Rev. B* **2008**, *78* (12), 125319.

(22) Stein, G. E.; Kramer, E. J.; Li, X.; Wang, J. Layering Transitions in Thin Films of Spherical-Domain Block Copolymers. *Macromolecules* **2007**, *40* (7), 2453–2460.

(23) Hammond, M. R.; Kline, R. J.; Herzing, A. a; Richter, L. J.; Germack, D. S.; Ro, H.-W.; Soles, C. L.; Fischer, D. a; Xu, T.; Yu, L.; et al. Molecular Order in High-Efficiency Polymer/fullerene Bulk Heterojunction Solar Cells. *ACS Nano* **2011**, *5* (10), 8248–8257.

(24) Ho, P. K.-H.; Chua, L.-L.; Dipankar, M.; Gao, X. Y.; Qi, D. C.; Wee, a. T.-S.; Chang, J.-F.; Friend, R. H. Solvent Effects on Chain Orientation and Interchain π-Interaction in Conjugated Polymer Thin Films: Direct Measurements of the Air and Substrate Interfaces by Near-Edge X-Ray Absorption Spectroscopy. *Adv. Mater.* **2007**, *19* (2), 215–221.

(25) Smilgies, D. M. Scherrer Grain-Size Analysis Adapted to Grazing-Incidence Scattering

with Area Detectors. *J. Appl. Crystallogr.* **2009**, *42* (6), 1030–1034.

(26) Rivnay, J.; Noriega, R.; Kline, R. J.; Salleo, A.; Toney, M. F. Quantitative Analysis of Lattice Disorder and Crystallite Size in Organic Semiconductor Thin Films. *Phys. Rev. B - Condens. Matter Mater. Phys.* **2011**, *84* (4), 1–20.

(27) Zhao, J.; Swinnen, A.; Van Assche, G.; Manca, J.; Vanderzande, D.; Van Mele, B. Phase Diagram of P3HT/PCBM Blends and Its Implication for the Stability of Morphology. *J. Phys. Chem. B* **2009**, *113* (6), 1587–1591.

(28) Ge, W.; Li, N. K.; McCormick, R. D.; Lichtenberg, E.; Yingling, Y. G.; Stiff-Roberts, A. D. Emulsion-Based RIR-MAPLE Deposition of Conjugated Polymers: Primary Solvent Effect and Its Implications on Organic Solar Cell Performance. *ACS Appl. Mater. Interfaces* **2016**, *8* (30), 19494–19506.

(29) Jeong, H.; Shepard, K. B.; Purdum, G. E.; Guo, Y.; Loo, Y. L.; Arnold, C. B.; Priestley, R. D. Additive Growth and Crystallization of Polymer Films. *Macromolecules* **2016**, *49* (7), 2860–2867.

(30) Salleo, a.; Chabinyc, M. L.; Yang, M. S.; Street, R. a. Polymer Thin-Film Transistors with Chemically Modified Dielectric Interfaces. *Appl. Phys. Lett.* **2002**, *81* (23), 4383.

(31) Chabinyc, M. L.; Salleo, A.; Wu, Y.; Liu, P.; Ong, B. S.; Heeney, M.; McCulloch, I. Lamination Method for the Study of Interfaces in Polymeric Thin Film Transistors. *J. Am. Chem. Soc.* **2004**, *126* (43), 13928–13929.

(32) Dong, B. X.; Amonoo, J. A.; Purdum, G. E.; Loo, Y. L.; Green, P. F. Enhancing Carrier Mobilities in Organic Thin-Film Transistors Through Morphological Changes at the Semiconductor/Dielectric Interface Using Supercritical Carbon Dioxide Processing. *ACS Appl. Mater. Interfaces* **2016**, *8* (45), 31144–31153.

Chapter 6 : CONCLUSION AND OUTLOOK

6.1. CONCLUSION

The research in this dissertation were designed and performed with the goal of using creative strategies to fabricate conjugated polymer thin-films and studying how polymer chemistry, fabricating and processing conditions affect microstructure and how details of the microstructure affect different charge transport mechanisms. The findings in this thesis provide fresh perspectives on the extent to which the detailed microstructure impact mechanisms of charge transport in conjugated polymers, providing important guidelines for designing conjugated polymer-based electronic devices with efficient transport.

In chapter two, we showed that due to a substrate-induced orientation of the local morphology of PBDTTT-C, the out-of-plane hole mobility μ increased with increasing film thickness h and becoming independent of h for $h > 110$ nm. The temperature and electric field dependencies of μ are in agreement with predictions of the well-known Gaussian Disorder Model (GDM), developed to describe charge transport in materials possessing positional and energetic disorder. Room temperature studies reveal a negative dependence of μ on the electric field E, with a strength quantified by the parameter β. The largest magnitude of β was measured in the thinnest films, indicative of the strongest dependence of μ on the electric field E; β decreased monotonically with increasing film thickness. The thickness dependencies of μ and β manifest an increase of the average anisotropy of the films with decreasing film thickness, corroborated by UV−vis spectroscopy and spectroscopic ellipsometry measurements. Our findings suggested that

transport is not an intrinsic property of conjugated polymer but rather dictated by local morphology.

In chapter three, we invested the effect of $scCO_2$ processing on structure and in-plane charge transport in P3HT films supported by two SAMs: OTS and FTS. We discovered that for P3HT fabricated on FTS, a SAM known to have high affinity toward $scCO_2$ annealing, $scCO_2$ preferably altered the structure of P3HT films at P3HT/FTS interface and consequently the in-plane carrier mobility increased by 5-fold. The effect of $scCO_2$ annealing on structure and transport of P3HT/OTS films was negligible. Our findings revealed an effective way to control the morphology of conjugated polymers at the semiconductor/substrate interface and suggested a strong dependence of polymer processing on the nature of polymer/substrate interface.

In chapter four, we used a novel vacuum deposition technique termed MAPLE to fabricate conjugated polymer thin films, and discovered that the structure of MAPLE-deposited samples were fundamentally different from the conventional spin-cast counterparts. Using a combination of optical and X-Ray diffraction characterization methods, we showed that MAPLE samples possessed high degree of disorder with more random orientations across side-chain, pi-stacking and backbone direction. Significantly, the structure of MAPLE-deposited samples is much less sensitive to substrate chemistry compared to the spin-cast analogs, suggesting different crystallization mechanism in MAPLE. In spite of the high degree of structural disorder in MAPLE- deposited films, the in-plane carrier mobilities were very comparable or even more superior to conventionally-cast devices.

Motivated by our findings in chapter four, in chapter five we investigated in detail the crystallization process in MAPLE and studied the structure at the buried interface in MAPLE-

deposited samples. Complete pole figures constructed from X-Ray diffraction measurements reveals that in MAPLE, there exist two distinct crystallite populations: one of highly-oriented crystals that grows from the flat dielectric substrate and one of misoriented crystals that preferably grows on top of existing polymer layers. Moreover, the growth of the highly-oriented crystals is highly sensitive to the chemistry of the substrate, whereas the effect of substrate chemistry on misoriented crystal growth is weaker. The use of a self-assembled monolayer greatly enhances the population and crystallite coherence length at the buried interfaces, especially at early deposition times. The evolution of in-plane mobility during the course of deposition correlates with the development of highly-oriented crystals at the buried interface, suggesting the importance of this interface in determining transport of organic thin-film transistor. This study offers fundamental understanding of crystallization mechanism in MAPLE in connection to carrier transport properties, providing an important step toward exploiting the technologically relevant strategy MAPLE to fabricate various conjugated polymer-based electronic devices.

6.2. OUTLOOK

6.2.1. Molecular Weight Dependence of Structure and Transport in MAPLE-deposited Conjugated Polymer Film

In the field of conjugated polymers, perhaps one of the most intriguing questions is related to the structural transition from small molecule to high molecular weight macromolecule and how the transition in the morphological structure affects physical properties. This transition has led to a plethora of investigations on the dependence of structure and many physical properties such as in-plane, out-of-plane charge transports, thermal analysis, mechanical properties or OPV performance on the molecular weight (MW) of conjugated polymer films.[1–5] Thus in order to

further realize MAPLE for technological and scientific applications, a thorough study on the MW dependence of structure and transport of MAPLE deposited conjugated polymer films is needed. To this end, in collaboration with McNeil Group in Chemistry Department, we are currently investigating the structure and transport properties of MAPLE-deposited P3HT films having molecular weight ranging from 2.8 kDa to 21.5 kDa. Figure 6.1 depicts the preliminary results of the GIWAXS diffraction patterns of the highest and lowest MW.

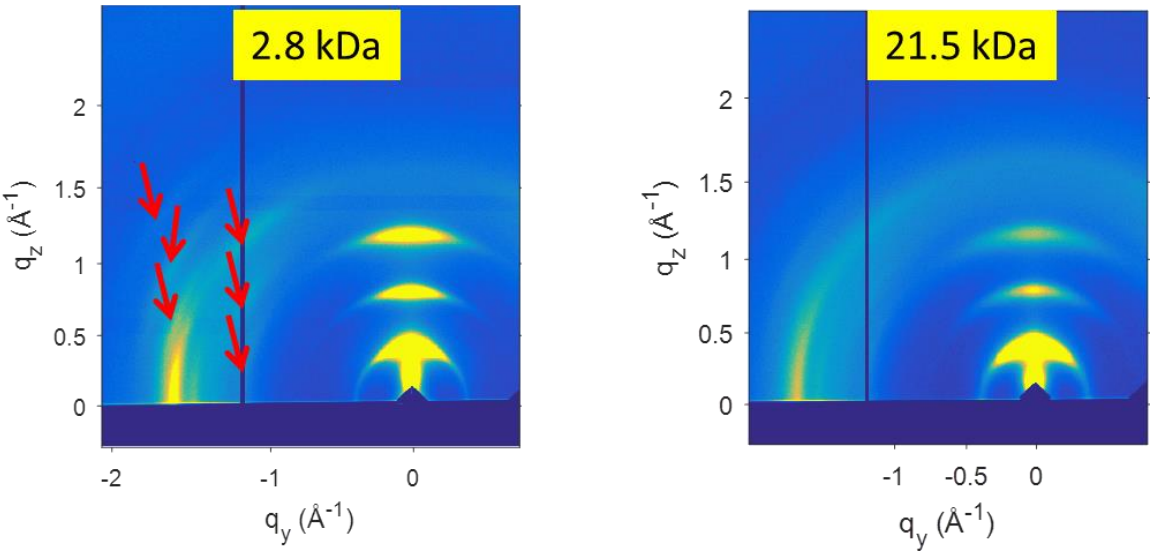

Figure 6.1. GIWAXS diffraction patterns of MAPLE-deposited P3HT films with 2 different MW: 2.8 kDa and 21.5 kDa. The arrows indicate additional diffraction peaks in low MW sample.

Interestingly, beside the typically observed (h00) and (010) diffraction peaks of the side-chain stacking and pi-stacking in P3HT, we also observed a numerous of additional diffraction peak in low MW sample as indicated by the red arrows. The appearance of additional diffraction peaks is indicative of more ordered structure. The origins of those diffraction peaks, the details of unit cells, degree of crystallinity and molecular orientation in connection to in- and out-of-plane charge transport of MAPLE-deposited samples at different MWs will be investigated.

6.2.2. Band Bending Effect in Conjugated Polymer Films: Role of Morphology

In any devices using conjugated polymers, an understanding of interfacial energy level alignment between conjugated polymers and the conducting electrodes is of particularly importance because this energy alignment determines many processes relevant to device performance. In this on-going project, we employ Kelvin Probe Force Microscopy (KPFM) technique that we built in our lab to investigate band bending of P3HT films fabricated using both conventional spin-casting and MAPLE technique on ITO:PEDOT substrates. The purpose of this project is to unravel the interplay between molecular structure, electronic states and bulk transport in conjugated polymer films. The basic of the KPFM measurement set-up and preliminary results of the surface potential measurement on a MAPLE-deposited P3HT films are shown in Figure 6.2.

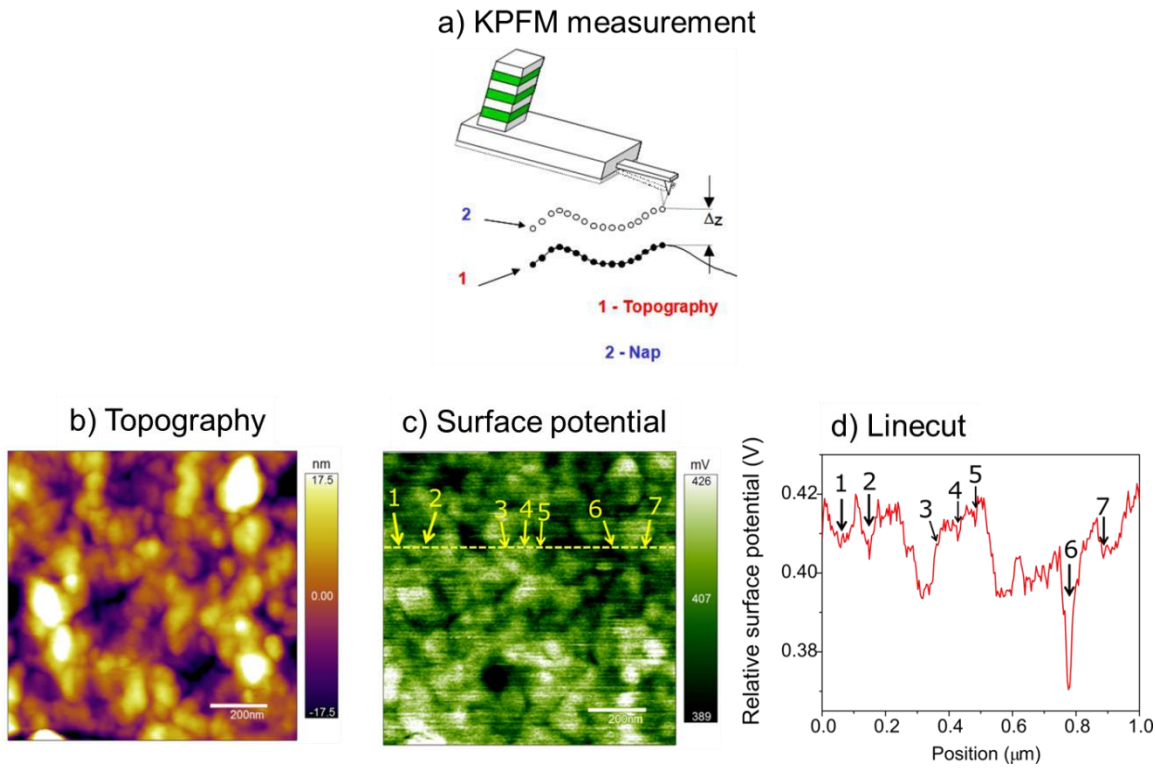

Figure 6.2. (a) Simplified illustration of the double pass technique used in KPFM measurements. (b),(c) Exemplary topographical images and the corresponding surface potential images of a MAPLE-deposited P3HT films (d) Surface potential linecut corresponding to the yellow dashed line in (c).

In our KPFM set-up, we use the double pass technique in which two scans are performed for each line in an image (Figure 6.2(a)). On the first pass the tip maps the topography where the amplitude of the mechanical oscillation, driven at the first resonance frequency of the cantilever, is used as the feedback signal to obtain surface topography. On the second pass the mechanical oscillations of the tip is set to zero while it is lifted along the z direction a known distance above the sample surface. This distance, known as the lift height (Δz), is typically 10 - 20 nm, outside the range of Van der Waal forces. The surface potential is measured at the second pass.[6] Preliminary result on MAPLE deposited samples showed that the surface potential of MAPLE films are highly heterogeneous, which lower surface potential at the globular boundaries

compared to its interior. This result indicated that the globular boundaries might serve as boundary for carrier transport in MAPLE-deposited film.

Future works will focus on studying band bending effect, i.e. measuring the surface potential at different film thickness. Throughout modeling,[7] we will calculate the broadening of the density of state (DOS) both in MAPLE and spin-cast samples. Temperature dependence of the out-of-plane carrier mobility will also be carried out to investigate the connection between bulk transport and the electronic structure extracted from the band bending data.

6.3. REFERENCES

(1) Koch, F. P. V.; Rivnay, J.; Foster, S.; Müller, C.; Downing, J. M.; Buchaca-Domingo, E.; Westacott, P.; Yu, L.; Yuan, M.; Baklar, M.; et al. The Impact of Molecular Weight on Microstructure and Charge Transport in Semicrystalline Polymer Semiconductors-poly(3-Hexylthiophene), a Model Study. *Progress in Polymer Science*. 2013, pp 1978–1989.

(2) Kline, R. J.; Mcgehee, M. D.; Kadnikova, E. N.; Liu, J.; Fre, J. M. J.; Toney, M. F. Dependence of Regioregular Poly (3-Hexylthiophene) Film Morphology and Field-Effect Mobility on Molecular Weight. *Macromolecules* **2005**, 3312–3319.

(3) Zen, a.; Pflaum, J.; Hirschmann, S.; Zhuang, W.; Jaiser, F.; Asawapirom, U.; Rabe, J. P.; Scherf, U.; Neher, D. Effect of Molecular Weight and Annealing of Poly(3-Hexylthiophene)s on the Performance of Organic Field-Effect Transistors. *Adv. Funct. Mater.* **2004**, *14* (8), 757–764.

(4) Ballantyne, A. M.; Chen, L.; Dane, J.; Hammant, T.; Braun, F. M.; Heeney, M.; Duffy, W.; McCulloch, I.; Bradley, D. D. C.; Nelson, J. The Effect of Poly(3-Hexylthiophene) Molecular Weight on Charge Transport and the Performance of Polymer:Fullerene Solar Cells. *Adv. Funct. Mater.* **2008**, *18* (16), 2373–2380.

(5) Brinkmann, M.; Rannou, P. Molecular Weight Dependence of Chain Packing and Semicrystalline Structure in Oriented Films of Regioregular poly(3-Hexylthiophene)revealed by High-Resolution Transmission Electron Microscopy. *Macromolecules* **2009**, *42*, 1125–1130.

(6) Hoppe, H.; Glatzel, T.; Niggemann, M.; Hinsch, A.; Lux-Steiner, M. C.; Sariciftci, N. S. Kelvin Probe Force Microscopy Study on Conjugated Polymer/fullerene Bulk Heterojunction Organic Solar Cells. *Nano Lett.* **2005**, *5* (2), 269–274.

(7) Lange, I.; Blakesley, J. C.; Frisch, J.; Vollmer, A.; Koch, N.; Neher, D. Band Bending in Conjugated Polymer Layers. *Phys. Rev. Lett.* **2011**, *106* (21), 216402.